



Max-Planck-Institut für Kolloid- und Grenzflächenforschung

Abteilung Theorie und Bio-Systeme

Theoretische biologische Physik

**Morphological transitions of vesicles exposed to nonuniform  
spatio-temporal conditions**

DISSERTATION

zur Erlangung des akademischen Grades

„doctor rerum naturalium“ (Dr. rer. nat.)

im Doktoratsstudium der

Physik

**Simon Christ**

eingereicht an der:

Mathematisch Naturwissenschaftlichen Fakultät

Institut für Physik und Astronomie

der Universität Potsdam

This work is licensed under a Creative Commons License:  
Attribution – Share Alike 4.0 International.  
This does not apply to quoted content from other authors.  
To view a copy of this license visit  
<https://creativecommons.org/licenses/by-sa/4.0>

Dekan: Prof. Helmut Elsenbeer

Betreuer:  
Prof. Reinhard Lipowsky  
Prof. Ralf Metzler

Gutachter:  
Prof. Reinhard Lipowsky  
Prof. Ralf Metzler  
Prof. Udo Seifert

Published online on the  
Publication Server of the University of Potsdam:  
<https://doi.org/10.25932/publishup-48078>  
<https://nbn-resolving.org/urn:nbn:de:kobv:517-opus4-480788>

# Morphological transitions of vesicles exposed to nonuniform spatio-temporal conditions

Simon Christ

It's not „publish or perish“ any  
more,  
it's „share and thrive“.

---


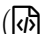

*The Carpentries lesson*

# Contents

<i>Acknowledgments</i>	vii	
1	<i>Introduction</i>	1
2	<i>Theoretical preliminaries</i>	5
2.1	<i>Calculus of variation</i>	5
2.2	<i>Free energy of a canonical ensemble</i>	8
3	<i>Flexible and rigid membrane compartments</i>	11
3.1	<i>Spontaneous curvature model</i>	12
3.2	<i>Cones with constant area and volume</i>	16
4	<i>Morphologies of uniform vesicles in equilibrium</i>	27
4.1	<i>Zero spontaneous curvature</i>	27
4.2	<i>Positive spontaneous curvature</i>	29
4.3	<i>Bridging the gap - parameterization for narrow necks</i>	34
5	<i>Non-equilibrium shape transformations</i>	39
5.1	<i>Shape oscillations in GUVs filled with min-proteins</i>	39
6	<i>Concentration gradients in rigid compartments</i>	55
6.1	<i>Ideal gas in cones</i>	55

6.2	<i>Cytoskeletal molecular motors</i>	57
6.3	<i>Molecular motors in tubes</i>	59
6.4	<i>Density of molecular motors in conic compartments</i>	62
7	<i>Discussion</i>	71
8	<i>Summary</i>	73
A	<i>Concentration gradients in flexible compartments</i>	75
A.1	<i>Shape equations for an ideal gas in a vesicle</i>	75
B	<i>VesicleForms.jl</i>	77
B.1	<i>Solving the shape equations</i>	77
C	<i>Molemoto</i>	81
	<i>References</i>	85
	<i>Glossary</i>	91
	<i>Numerical Constants</i>	101
	<i>Abbreviations</i>	103
	<i>List of source links</i>	105

# *Preface*


This thesis contains marks for reproducible content. Namely links to notebooks, e.g. for derivations of formulas () , links to source code of scripts for figures or numerical calculations () as well as links to animations () . These can be clicked in the online version and are also listed in the List of source links at the end of the thesis sorted by page number. These are mainly to facilitate the reproduction of the content for future studies and are not needed to be reviewed.

## *Notation*

Throughout this document dotted variables like  $\dot{f}$  refer to the derivative with respect to the arc-length  $s$ , e.g.  $\dot{f} = \frac{\partial}{\partial s}f$ .

# *Acknowledgments*

This work was done under the supervision of Prof. Lipowsky and funded by the Max-Planck society. Thanks for technical support to the IT-department of the Max-Planck institute of colloids and interfaces as well as the library staff. Additional support both technical and morally was given by the julia<sup>[1]</sup>-community. Furthermore Jörg Bachmann helped developing C++ code and took part in many discussions. Jaime Agudo and Melanie Müller helped a lot by providing

the source code of their research. The template and pipeline for this document is thankfully adopted from the Stanford Intelligent Systems Lab . All of this would not have been possible without the loving support of my family.



# 1 *Introduction*

The formation of the first cell was a breaking point in the evolution of complex organisms like animals, bacteria and plants. A cell is an entity that is separated from its environment by a lipid membrane. Over time, the interior of the cell evolved by subdivision and change of its composition, by fission into separate cells and fusion with other cells. With rising complexity different functional complexes differentiated and formed what is today known as prokaryotic and eukaryotic cells.

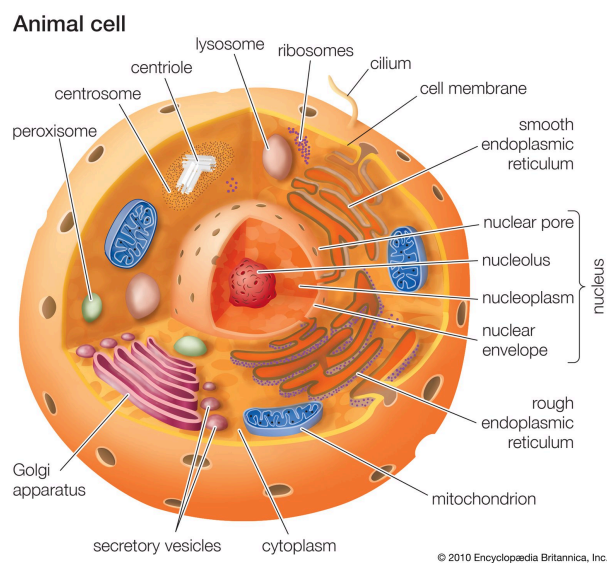
While natural evolution is increasing the complexity over time, scientists use reductionism as a tool to understand complex systems. This means, that they strive to identify elementary components with respect to a specific function or an observed effect.

Taking the human cells as an example, a variety of specialised cells exists: Oblate shaped red blood cells can transport oxygen from the lungs to the tissue and carbon-dioxide back; polyhedral shaped brown fat cells (plurivacuolar adipocytes) have a large amount of mitochondria to produce heat; and the long tube-like axons of nerve cells transport electrical signals and create concentration gradients via ion-pumps.

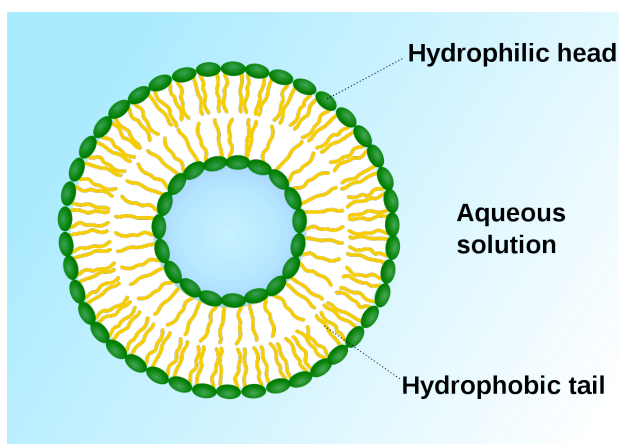
This thesis focuses on the shape of cells. Cells come in different shapes from discocyte human red blood cells<sup>[2]</sup> to prolate *E. coli* bacteria. Furthermore they can change their shape to fit through narrow capillaries or replicate via cell division. On the other hand malformed cells can lead to diseases like sphero- or ellipsocytosis<sup>[2]</sup>.

Natural cells are very complicated organisms whose membranes can contain many different components as well as channels or other pro-

teins as shown in figure 1.1a. Very simple membranes with only a few components are produced in laboratories. These simple membranes are called biomimetic membranes. A schematic drawing is shown in figure 1.1b. They can be used to create „empty“ cells, which are called vesicles, and they can be produced in a wide range of sizes and, as visible in chapter 4, come in a number of different shapes. This is very useful for controlled experiments, since it is easier to isolate functional behaviour. One such experiment will be analyzed in more detail in chapter 5.



(a) Schematic representation of an animal cell<sup>[3]</sup>



(b) Schematic representation of a vesicle<sup>[4]</sup>

Figure 1.1. Comparison of animal cells and vesicles. (a) The animal cell consist of three main layers: The nucleolus at its core, the nuclear envelope and the cell membrane. The nuclear envelope separates the nucleoplasm from the cytoplasm, whereas the cell membrane separates the cytoplasm from the outer solution. In the cytoplasm many smaller compartments, such as lysosomes, ribosomes or mitochondria can be encapsulated. In addition larger structures that have shapes akin to folded sheets, like the golgi apparatus and the rough endoplasmic reticulum are present. (b) In contrast to the complex structure of an animal the cell, a vesicle has only two components: The inner solution and the lipid bilayer, which may consist of different types of lipids, that separates the inner solution from the outer solution.

Giant unilamellar vesicles (GUVs) are being studied intensively since they are large enough to be observed by light microscopy and they show the remarkable property of being able to change between vari-

ous shapes. The transition from one shape to another can be induced by increasing or decreasing the asymmetry between the two leaflets of the lipid bilayer<sup>[5]</sup> or by adsorption of proteins to the membrane<sup>[6,7]</sup> as well as deflation or inflation of the vesicle. By adsorbing photo-switchable proteins to the membrane photoresponsive membranes can be obtained<sup>[8]</sup>, which means that a change of the shape of the vesicle can be induced by light in a reversible manner, e.g. the formation of a bud by exposition to UV-light and backtransformation to a spherical vesicle with blue light. In particular, the coexistence of highly curved tubes and necks with regions of relatively low curvature in the same vesicle is a central property to being able to undergo fission<sup>[7]</sup>.

In addition, GUVs can be used to encapsulate chemical compounds or build multilamellar structures<sup>[9,10]</sup>. Depending on the composition of the bilayer it is possible to observe phase-separation of liquid-ordered and liquid-disorderd phases<sup>[11,12]</sup>, which are also called rafts, as well as phase-separation of different gel-phases<sup>[13]</sup>. GUVs are thought to become a basic building block in the engineering of basic living organisms<sup>[14,15]</sup>.

With respect to theoretical modeling of membrane shapes mostly homogeneously filled vesicles have been considered so far and chapter 4 will recapitulate the findings relevant for this thesis. Beyond that, new results on multi-spherical vesicles will be reported.

In this thesis also vesicles in non-uniform environments are considered. This includes shape transformations due to the active process of membrane adhesion of Min-proteins in chapter 5, which causes periodic transitions in time between a homogeneous protein distribution and a distribution that is mainly localized on the membrane.

Furthermore, spatial concentration gradients are considered in chapter 6. These gradients can arise by external forces like electromagnetic or gravitational fields, by particle sinks or reservoirs like absorption sites or production sites as well as by active processes like the movement of processive molecular motors, which are introduced in sec-

tion 6.2. Molecular motors are naturally abundant in biological cells and as such are a promising candidate to be useful in practice. Their directed motion along the cytoskeleton may well be used to create a concentration gradient of the cargos that they are able to transport.

To decouple the complex behaviour of lipid membranes from the effects of concentration gradients rigid conic compartments as further explained in section 3.2 are used as a surrogate. The theoretical description of axisymmetric vesicles and conic compartments will be illustrated in chapter 3.

Another abundant force is the gravitational field of the earth, which causes sedimentation, but its strength is rather weak compared to other intracellular dynamics such as diffusion. An ideal gas in gravity will also be used as a surrogate system for the more complex system of the molecular motors in section 6.1. Both, the ideal gas and the gravitational force, are often used in theoretical physics to get a fundamental understanding of a more complex system. In this thesis they are used to get a qualitative picture of the expected effects of gradients, since many properties are analytically calculable.

In the following chapter 2 the fundamental theoretical preliminaries are introduced. Finally, the thesis will be concluded with a discussion in chapter 7 and a summary in chapter 8.

## 2 Theoretical preliminaries

### 2.1 Calculus of variation

The calculus of variation investigates conditions to find critical points  $\xi_0$  of a function  $f : X \rightarrow \mathbb{R}$  where  $X$  is an open subset of a  $k$ -dimensional Banach space (like the set of all functions<sup>1</sup>). A critical point is a point for which the first variation  $\delta f$  of  $f$  vanishes, which is either a local maximum, a local minimum or a saddle-point. In order to distinguish between these cases higher order variations have to be considered. Here, a variation of  $f(\xi)$  means that instead of the functions  $\xi$  a univariate family of functions  $\xi + \varepsilon\eta$  is considered and the variation  $\delta$  can be defined as

$$\delta = \varepsilon \lim_{\varepsilon \rightarrow 0} \frac{\partial}{\partial \varepsilon} \quad (2.1)$$

and interpreted as the amount the value of  $f$  would change at each point  $\xi$  along the curve that  $f$  defines in  $X$  if it would be slightly perturbed. A typical mathematical formulation for a variational problem reads

$$\delta \int_{s_0}^{s_1} f(\xi, \xi', s) \, ds = \int_{s_0}^{s_1} \delta f(\xi, \xi', s) \, ds = 0. \quad (2.2)$$

These formulations are very useful in the field of theoretical physics since it allows to formulate laws of nature independent of any coordinate system (like Fermat's principle or Hamilton's principle). Finally, the solutions to equation (2.2) can be found by solving the Euler-Lagrange equations<sup>[16]</sup>

$$\frac{d}{ds} \left( \frac{\partial}{\partial \dot{\xi}_i} f \right) - \frac{\partial}{\partial \xi_i} f = 0, \quad i \in [1, k], \quad (2.3)$$

<sup>1</sup> In that case  $f$  is called a *functional* and for the rest of this document  $X$  is treated as the set of all functions.

which are  $k$  second order differential equations, which corresponds to  $2k$  first order differential equations.

### 2.1.1 Constrained variation

Often not all possible points  $\xi$  are physically possible. Then the set  $X$  is said to be constrained. Constraints can be expressed in differential or integral form. These are demonstrated in example 2.1. In general, constraints can be written as  $g_i(f) = 0$ , where  $i \in [1, m]$  if  $m$  is the number of constraints. Constraints can be incorporated by introduc-

Dido was the founder and first queen of Carthage. According to a tradition of the Greek historian Timaeus she got the land from the Numidian King Hierbas by asking for as much land as can be encompassed by a bull's hide in 814BC. After he agreed, she cut the hide into thread-like strips and formed a circle with it, thus gaining the maximum amount of area. The corresponding variational problem can be stated as follows

$$\begin{aligned} \delta \int_{s_0}^{s_1} f \, ds &= 0 \\ g(f) &= \int_{s_0}^{s_1} \sqrt{1 + f^2} \, ds = L \\ f(s_0) &= f_0, \quad f(s_1) = f_1 \end{aligned} \tag{2.4}$$

or

$$\begin{aligned} \delta \int_{s_0}^{s_1} f \, ds &= 0 \\ \dot{g} &= \sqrt{1 + f^2} \\ f(s_0) &= f_0, \quad f(s_1) = f_1 \\ g(s_0) &= 0, \quad g(s_1) = L \end{aligned} \tag{2.5}$$

where equation (2.4) is the integral formulation and equation (2.5) is the differential formulation. The more general problem of determining a plane figure of the largest possible area whose boundary has a specified length is called an *isoperimetric problem*.

Example 2.1. Dido's problem

ing as many new functions  $\lambda_i(s)$  as constraints have to be satisfied and define

$$F = f + \sum_{i=1}^m \lambda_i(s) g_i. \tag{2.6}$$

The  $\lambda_i(s)$  are called Lagrange multipliers. Again, these have to fulfill the Euler-Lagrange equations

$$\frac{d}{ds} \left( \frac{\partial}{\partial \dot{\xi}_i} F \right) - \frac{\partial}{\partial \xi_i} F = 0, \quad i \in [1, k]. \quad (2.7)$$

## 2.2 Free energy of a canonical ensemble

In classical statistical thermodynamics a canonical ensemble describes a statistical system with constant temperature  $T$ , constant volume  $V$  and constant number of particles  $N$ .<sup>[17]</sup>

### 2.2.1 Partition sum

A fundamental thermodynamic entity is the partition sum  $Z$ , since every thermodynamic potential can be derived from the partition sum. With a given partition sum and the inverse thermal energy  $\beta = \frac{1}{k_B T}$ , the free energy  $F$  can be calculated via

$$F = -\frac{1}{\beta} \log Z. \quad (2.8)$$

Since the particles of an ideal gas do not interact, the  $N$ -particle partition sum can be directly computed by the one particle partition sum  $Z_1$

$$Z = Z_1^N. \quad (2.9)$$

The Hamiltonian  $\mathcal{H}(\mathbf{r}, \mathbf{p})$  is a function that describes the total energy of a conservative physical system in terms of the generalized coordinates  $\mathbf{r}$  and  $\mathbf{p}$ , which correspond to the three spatial coordinates and three mechanical impulses for the ideal gas. For an ideal gas consisting of particles of mass  $M$  that are subject to the gravitational acceleration  $g$  the Hamiltonian reads

$$\mathcal{H}(\mathbf{r}, \mathbf{p}) = \sum_{i=1}^N \frac{\mathbf{p}_i^2}{2M} + Mgz_i, \quad (2.10)$$

where  $z_i$  is the  $z$ -coordinate of particle  $i$  in a cartesian or cylindrical coordinate system.



Using the Hamiltonian, the one particle partition sum is defined by an integral over the enclosing volume  $V$

$$\begin{aligned} Z_1 &= \frac{1}{h^3} \int d^3\mathbf{r} \int d^3\mathbf{p} e^{-\beta\mathcal{H}(\mathbf{r},\mathbf{p})} \\ &= \left(\frac{2\pi M}{h^2\beta}\right)^{\frac{3}{2}} \int e^{-\beta Mgz} dV. \end{aligned} \quad (2.11)$$

Examples 2.2 to 2.4 show the one particle partition sum for the cases of a spheric, a tubular and a conic compartment.


$$\begin{aligned} Z_1 &= \left(\frac{2\pi M}{h^2\beta}\right)^{\frac{3}{2}} \int e^{-\beta Mgz} dV \\ &= \left(\frac{2\pi M}{h^2\beta}\right)^{\frac{3}{2}} 2\pi \int_0^{2R} \int_0^{\sqrt{R^2-(z-R)^2}} e^{-\beta Mgz} r dr dz \\ &= \left(\frac{2\pi M}{h^2\beta}\right)^{\frac{3}{2}} \left( \frac{4\pi e^{-\beta MgR} (\beta MgR \cosh(\beta MgR) - \sinh(\beta MgR))}{(\beta Mg)^3} \right) \end{aligned}$$

Example 2.2. Partition sum inside a sphere of radius  $R$ .

$$\begin{aligned} Z_1 &= \left(\frac{2\pi M}{h^2\beta}\right)^{\frac{3}{2}} \int e^{-\beta Mgz} dV \\ &= \left(\frac{2\pi M}{h^2\beta}\right)^{\frac{3}{2}} \pi R^2 \int_0^L e^{-\beta Mgz} dz \\ &= \left(\frac{2\pi M}{h^2\beta}\right)^{\frac{3}{2}} \frac{\pi R^2}{\beta Mg} (1 - e^{-\beta MgL}) \end{aligned}$$

Example 2.3. Partition sum inside a tube of height  $L$  and radius  $R$ .

$$\begin{aligned}
Z_1 &= \left( \frac{2\pi M}{h^2 \beta} \right)^{\frac{3}{2}} \int e^{-\beta M g z} dV \\
&= \left( \frac{2\pi M}{h^2 \beta} \right)^{\frac{3}{2}} \frac{\pi}{(\beta M g)^3} \int_0^L e^{-\beta M g z} r(z)^2 dz \\
&= \left( \frac{2\pi M}{h^2 \beta} \right)^{\frac{3}{2}} \frac{\pi e^{-\beta M g L}}{(2\beta M g)^3 \cos^2 \alpha} \left( (\cos(2\alpha) - 1) \right. \\
&\quad \left( (1 - e^{\beta M g L}) (8 + (\beta M g L)^2) + 4\beta M g L (1 + e^{\beta M g L}) \right) \\
&\quad - (\cos(2\alpha) + 1) 4(\beta M g R)^2 (1 - e^{\beta M g L}) \\
&\quad \left. + 4\beta M g R \sin(2\alpha) (2(1 - e^{\beta M g L}) + \beta M g L (1 + e^{\beta M g L})) \right)
\end{aligned}$$

Example 2.4. Partition sum inside a cone of height  $L$  and mid-height radius  $R$  and opening angle  $\alpha$ .  $r(z)$  is defined by equation (3.20). 

### 3 *Flexible and rigid membrane compartments*

Biological membranes mainly consist of glycerophospholipids whose amphipathic<sup>1</sup> nature drives the formation of a bilayered structure. These bilayers are very anisotropic: they have a thickness of a few nanometers, while their lateral size can extend over hundreds of micrometer. The ability of the lipids to laterally diffuse in the bilayer allows a smooth shape where the individual positions of the lipids are not very important. It is rather the elastic properties on the larger scale that define the overall shape. This allows to model it as a continuous yet flexible surface, rather than as an ensemble of many individual lipids<sup>2</sup>.

It is also possible to attach a lipid bilayer to a solid support<sup>[18,19]</sup>. In this case the shape is determined by the shape of the support. Also the rigid walls of the channels in microfluidic devices<sup>[20,21]</sup> or the tip of micropipettes<sup>[22–25]</sup> force vesicles to take a shape that is conformant with these boundaries.

This chapter explains the mathematical modeling of asymmetric flexible membranes using the spontaneous curvature model in the first section and the mathematical description of truncated cones in the second section.

<sup>1</sup>This means that glycerophospholipids have a hydrophobic part, which is the tail, as well as a hydrophilic part, which is the polar head group

<sup>2</sup>Which is what is done in molecular dynamics simulations

### 3.1 Spontaneous curvature model

Vesicle sizes vary from 15nm-30nm in diameter (small unilamellar vesicles (SUVs)) to 100nm-200nm in diameter (large unilamellar vesicles (LUVs)) to 5  $\mu$ m-200  $\mu$ m (GUVs)<sup>[26]</sup>. These sizes have to be compared to the thickness of the lipid bilayer which is typically 4nm-5nm<sup>[27]</sup>. Thus, for large scale shape transformations the membrane of a vesicle can be modelled as a continuous surface in space. The bending energy of such a vesicle with mean curvature  $\mathcal{M}$ , spontaneous curvature  $m$ , bending rigidity  $\kappa$  and surface area  $A$  is given by<sup>[28-30]</sup> <sup>3</sup>

$$\mathcal{E}_{\text{be}} = 2\kappa \int (\mathcal{M} - m)^2 dA. \quad (3.1)$$

Vesicles that stay isolated in constant osmotic conditions also have approximately constant area and volume. This is accounted for by adding two Lagrange multipliers as mentioned in section 2.1.1: the surface tension  $\Sigma$  that ensures constant area  $A$  and the difference in osmotic pressure  $\Delta P$  that ensures constant volume  $V$ .

$$\mathcal{E} = \mathcal{E}_{\text{be}} + \Sigma A - \Delta P V. \quad (3.2)$$

#### 3.1.1 Scales of a sphere

Even if osmotic conditions vary, the surface area of vesicles does not change much for isothermal processes<sup>[30]</sup>. Treating it as conserved is a very good approximation in these cases and therefore the surface area is a good candidate for defining the basic length-scale of the system. Furthermore, a sphere is the form with the minimal surface area for a given volume and is hence chosen as the reference shape. Thus, the vesicle radius  $R_{\text{ve}}$  is defined by the radius of a sphere with the same surface area as the vesicle

$$R_{\text{ve}} = \sqrt{A/(4\pi)}. \quad (3.3)$$

<sup>3</sup>The bending energy actually contains an additional term depending on the gaussian curvature, which depends on the topological genus of the surface. But since in this thesis only surfaces with one connected component are considered, this term is constant and can be neglected.

Consequently all curvatures will be scaled with  $R_{\text{ve}}$ :

$$\bar{m} = mR_{\text{ve}}, \quad (3.4)$$

$$\bar{\mathcal{M}} = \mathcal{M}R_{\text{ve}}. \quad (3.5)$$

Volume and area are scaled by their spheric equivalent:

$$\bar{A} = \frac{A}{4\pi R_{\text{ve}}^2} = 1, \quad (3.6)$$

$$v = \frac{V}{\frac{4\pi}{3}R_{\text{ve}}^3} = 6\sqrt{\pi}\frac{V}{A^{\frac{3}{2}}}. \quad (3.7)$$

The normalized volume  $v$  is also known as reduced volume or area-to-volume ratio in the literature. The bending energy of a sphere with zero spontaneous curvature is  $8\pi\kappa$ . This is a common choice for the basic energy scale

$$\bar{\mathcal{E}} = \mathcal{E}/(8\pi\kappa) = \bar{\mathcal{E}}_{\text{be}} + \frac{\Sigma A}{8\pi\kappa} - \frac{\Delta PV}{8\pi\kappa}. \quad (3.8)$$

Finally, by introducing the dimensionless surface tension  $\bar{\Sigma}$

$$\bar{\Sigma} = \frac{\Sigma R_{\text{ve}}^2}{\kappa} \quad (3.9)$$

and osmotic pressure difference  $\Delta\bar{P}$

$$\Delta\bar{P} = \frac{\Delta P R_{\text{ve}}^3}{\kappa} \quad (3.10)$$

equation (3.2) reads

$$\bar{\mathcal{E}} = \int (\bar{\mathcal{M}} - \bar{m})^2 d\bar{A} + \frac{1}{2} \left( \bar{\Sigma} - \frac{\Delta\bar{P}}{3}v \right). \quad (3.11)$$

An additional parameter that is important in the next section is the arc-length  $S$ , which gets scaled by the arc-length of a semi-circle because that is the minimal integration length

$$\bar{S} = \frac{S}{\pi R_{\text{ve}}}. \quad (3.12)$$

## 3.1.2 Axisymmetric vesicles

In particular, axisymmetric vesicles can be described solely by a one dimensional curve  $\bar{r}(s)$ , where  $s \in [0, 1]$  is the position along the arc-length  $S$ . The bending energy can then be expressed in terms of  $\bar{r}(s)$  and its derivatives. However, it is far more convenient to use a parameterization in terms of  $\bar{r}(s)$  as well as the bending angle  $\psi(s)$  and the bending curvature  $\bar{u}(s) = \pi\bar{S}\dot{\psi}(s)$ .

The bending angle  $\psi(s)$  and  $\bar{r}(s)$  are related via (cf. figure 3.1)

$$\dot{\bar{r}}(s) = \pi\bar{S} \cos \psi(s). \quad (3.13)$$

This non-trivial dependency makes it necessary to add an additional term to (3.11) containing a Lagrange parameter function  $\bar{\gamma}_r(s)$ <sup>[16]</sup>

$$\bar{\mathcal{E}} = \bar{\mathcal{E}}_{\text{be}} + \frac{1}{2} \left( \bar{\Sigma} - \frac{\Delta\bar{P}}{3} v \right) + \pi\bar{S} \int \bar{\gamma}_r(s) (\dot{\bar{r}}(s) - \pi\bar{S} \cos \psi(s)) ds. \quad (3.14)$$

Parameterizing the remaining terms yields

$$\begin{aligned} \bar{\mathcal{E}} = \pi\bar{S} \int & \left( \frac{\bar{r}}{8} \left( \frac{d}{ds} \psi(s) + \frac{\sin \psi(s)}{\bar{r}(s)} - 2\bar{m} \right)^2 + \frac{\bar{\Sigma}}{4} \bar{r}(s) - \frac{\Delta\bar{P}}{8} \bar{r}^2(s) \sin \psi(s) + \right. \\ & \left. \bar{\gamma}_r \left( \frac{d}{ds} \bar{r}(s) - \cos \psi(s) \right) \right) ds. \end{aligned} \quad (3.15)$$

Demanding the first variation of this functional to vanish yields the corresponding Euler-Lagrange-equations also known as the shape equations

$$\begin{aligned} \dot{\psi}(s) &= \pi\bar{S}\bar{u}(s) \\ \bar{u}(s) &= \pi\bar{S} \frac{(\bar{r}(s) (8\bar{\gamma}_r(s) \sin \psi(s) - \cos \psi(s) (\Delta\bar{P} \bar{r}^2(s) + 2\bar{u}(s))) + \sin(2\psi(s)))}{2\bar{r}(s)^2} \\ \dot{\bar{r}}(s) &= \pi\bar{S} \cos \psi(s) \\ \dot{\bar{\gamma}}_r(s) &= \frac{\pi\bar{S}}{8} \left( (\bar{u}(s) - 2\bar{m})^2 - 2\Delta\bar{P} \bar{r}(s) \sin \psi(s) - \frac{\sin^2 \psi(s)}{\bar{r}(s)^2} + 2\bar{\Sigma} \right). \end{aligned} \quad (3.16)$$

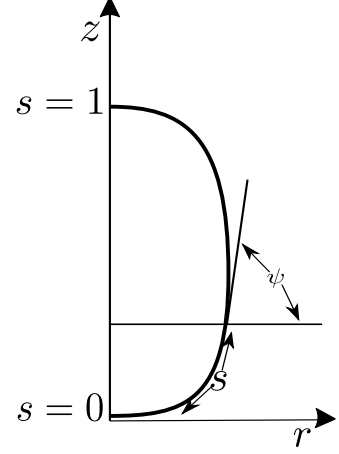


Figure 3.1. Illustration of the coordinate system of a vesicle that is parameterized along its arc-length  $s$ . The axis of rotation is  $z$ , the radial distance is  $r$  and the bending angle is denoted by  $\psi$ .

These have to satisfy the boundary conditions

$$\begin{aligned}
\psi(0) &= 0 \\
\psi(1) &= \pi \\
\bar{u}(0) &= \bar{u}_0 \\
\bar{u}(1) &= \bar{u}_1 \\
\bar{r}(0) &= \bar{r}(1) = 0 \\
\bar{\gamma}_r(0) &= \bar{\gamma}_r(1) = 0.
\end{aligned} \tag{3.17}$$

Special care has to be taken in the limit  $\bar{r}(s) \rightarrow 0$ , since the terms  $\frac{\sin \psi(s)}{\bar{r}(s)}$  can't be evaluated naively. From the Taylor expansions in appendix B follows that

$$\frac{\sin \psi(s)}{\bar{r}(s)} \Big|_{s=\{0,1\}} = u_{\{0,1\}}. \tag{3.18}$$

Thus, the shape equations at the endpoints read

$$\begin{aligned}
\dot{\psi}(s) &= \pi \bar{S} \bar{u}(s) \\
\dot{\bar{u}}(s) &= 4\pi \bar{S} \bar{u}(s) \bar{\gamma}_r(s) \\
\dot{\bar{r}}(s) &= \pi \bar{S} \cos \psi(s) \\
\dot{\bar{\gamma}}_r(s) &= \pi \bar{S} \left( \frac{1}{8} \left( (\bar{u}(s) - 2\bar{m})^2 - \bar{u}(s)^2 \right) + \frac{1}{4} \bar{\Sigma} \right) \\
&= \pi \bar{S} \left( \frac{1}{2} \left( \bar{m}^2 - \bar{m} \bar{u}(s) \right) + \frac{1}{4} \bar{\Sigma} \right).
\end{aligned} \tag{3.19}$$

In total this model has seven parameters:  $\Delta \bar{P}, \bar{\Sigma}, \bar{u}_0, \bar{u}_1, \bar{S}, \bar{m}$  and  $v$ .

### 3.2 Cones with constant area and volume

As mentioned in the beginning of chapter 3 besides flexible compartments also rigid compartments are part of this study. Particularly, the focus is on circular cones, which includes truncated cones and the special case of a tube. From a theoretical point of view rigid shapes can also act as a surrogate shape that facilitate analytic calculations to gain insight in the qualitative behaviour of vesicles.

An open cone is represented by its radial profile  $r(z)$  (cf. figure 3.2), which gives the three dimensional body by revolution around the  $z$ -axis

$$r(z) = R - \left( z - \frac{L}{2} \right) \tan \alpha. \quad (3.20)$$

Alternatively, it is also possible to parameterize the radial coordinate along the arc-length  $s$

$$r(s) = \begin{cases} s & 0 \leq s \leq \frac{R + \frac{1}{2}L \tan \alpha}{2R + L\sqrt{1 + \tan^2 \alpha}} \\ R - \left( s \left( 1 + \frac{2R}{L\sqrt{1 + \tan^2 \alpha}} \right) - \frac{R + \frac{1}{2}L \tan \alpha}{L\sqrt{1 + \tan^2 \alpha}} - \frac{1}{2} \right) L \tan \alpha & \frac{R + \frac{1}{2}L \tan \alpha}{2R + L\sqrt{1 + \tan^2 \alpha}} < s \wedge \\ & s < \frac{R + \frac{1}{2}L \tan \alpha + L\sqrt{1 + \tan^2 \alpha}}{2R + L\sqrt{1 + \tan^2 \alpha}} \\ 2R + L\sqrt{1 + \tan^2 \alpha}(1 - s) & \frac{R + \frac{1}{2}L \tan \alpha + L\sqrt{1 + \tan^2 \alpha}}{2R + L\sqrt{1 + \tan^2 \alpha}} \leq s \wedge \\ & s \leq 1 \end{cases} \quad (3.21)$$

which describes a closed cone. However, it is also possible to use equation (3.20) for closed cones, when the two circular disks at the ends are treated separately in the calculation of derived quantities like the area. Figure 3.2 illustrates the geometry of a closed cone; its two kinks are marked as point **A** and point **B**.

When points **A** and **B** are represented as position vectors in the  $z$ - $r$ -plane, they read as follows

$$\mathbf{A} = \begin{bmatrix} 0 \\ R + \frac{L}{2} \tan \alpha \end{bmatrix}, \quad \mathbf{B} = \begin{bmatrix} L \\ R - \frac{L}{2} \tan \alpha \end{bmatrix}.$$



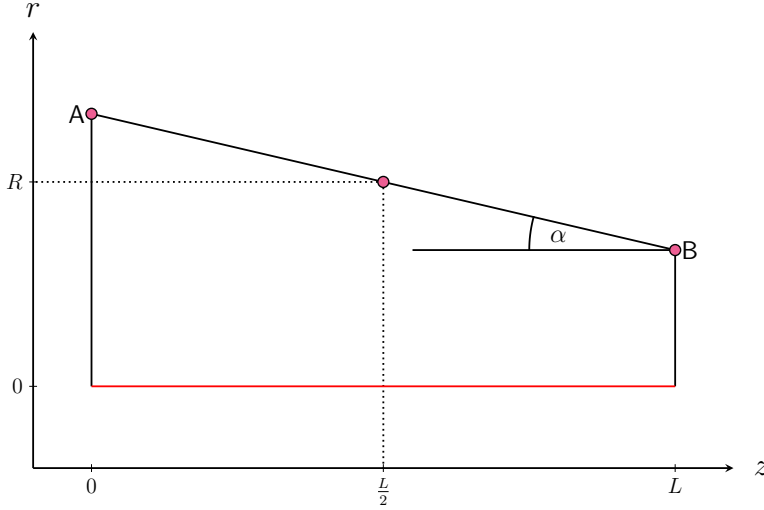


Figure 3.2. Cross section of a truncated cone as considered in this thesis. Halfway between point A and point B the radius  $R$  is kept constant. The length of the cone is the distance between the  $z$ -coordinates of point A and point B. Finally, the opening angle  $\alpha$  is measured between the  $z$ -axis and the connecting line of A and B.

The values of the opening angle  $\alpha$  lie in the closed interval  $\alpha \in [-\alpha_c, \alpha_c]$  with the critical value

$$\alpha_c = \arctan\left(\frac{2R}{L}\right). \quad (3.22)$$

If  $\alpha = -\alpha_c$  point A lies on the  $z$ -axis (red line in figure 3.2) and respectively point B lies on the  $z$ -axis for  $\alpha = \alpha_c$ .

### 3.2.1 Volume and Area

Volume  $V$  and surface area  $A$  of these cones are given by standard calculus

$$\begin{aligned} A &= 2\pi \int_0^L r(z) dz + \pi (r(0)^2 + r(L)^2) \\ &= \frac{\pi}{2} (L^2 \tan^2(\alpha) + 4R(L + R)) \\ V &= \pi \int_0^L r(z)^2 dz \\ &= \pi \left( \frac{1}{12} L^3 \tan^2(\alpha) + LR^2 \right). \end{aligned}$$

However, inverting those equations to get radius and length of cones with constant area and volume for a given opening angle cannot be done analytically, because the following equation (3.23) for determining the height  $L$  is a sixth order polynomial and it is proven that there is no general analytical solution for polynomials with higher order than

four<sup>[31]</sup>. These equations read

$$\begin{aligned} & \pi^2 L^6 \tan^2 \alpha \left( \tan^2 \alpha + 3 \right) - 6\pi AL^4 \tan^2 \alpha \\ & + 12\pi VL^3 \left( \tan^2 \alpha - 3 \right) + (3LA - 6V)^2 = 0 \end{aligned} \quad (3.23)$$

$$R_i(\alpha) = \frac{1}{2} \sqrt{\frac{4V}{\pi L_i(\alpha)} - \frac{1}{3} L_i^2(\alpha) \tan^2(\alpha)}. \quad (3.24)$$

$$i = 1, 2$$

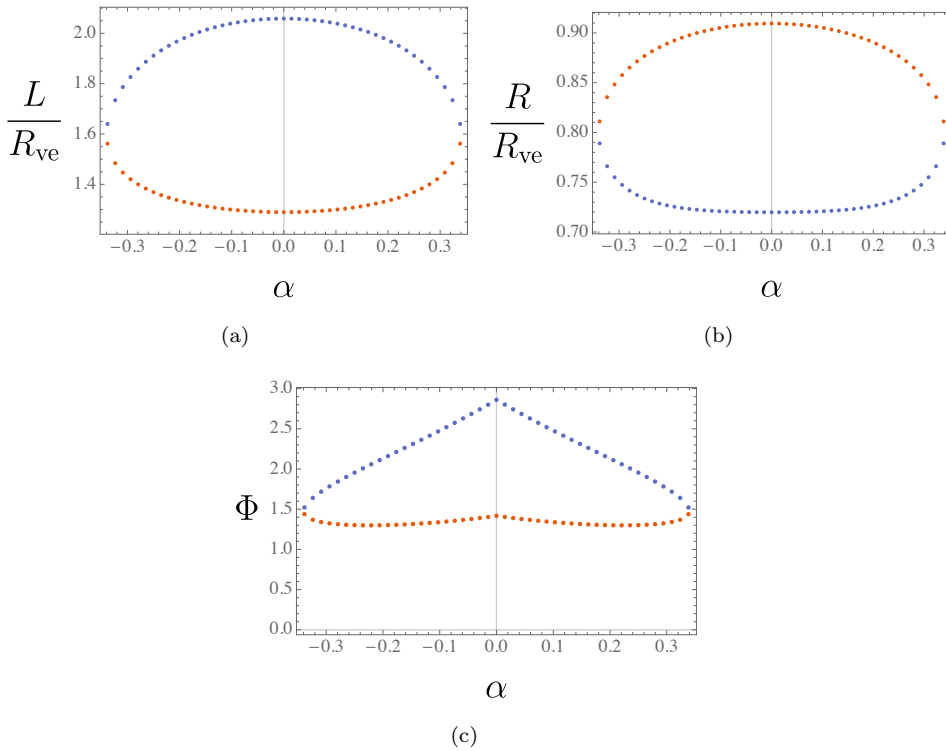


Figure 3.3. The two solutions to equation (3.24) (a) and equation (3.23) (b) as function of the opening angle  $\alpha$  for  $V = 1\text{pl}$ ,  $v = 0.8$  and  $m = 0$ . The orange solution is stretching the length of the cone and shrinking the radius to obtain a cylinder and the other solution is behaving the other way around. (c) The aspect ratio  $\Phi$  as given by equation (3.25). Shapes corresponding to the orange data points have a smaller aspect ratio than the solutions shown in blue, except for two critical angles  $\pm\alpha_c$  where both are equal to 1.5.

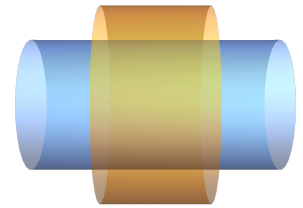


Figure 3.4. Illustration of the two solutions of equation (3.23) for  $\alpha = 0$ . The orange cylinder has a smaller height  $L$  and a larger radius  $R$  and vice versa for the blue cylinder.

A numerical solution of equations (3.23) and (3.24) can be seen in figure 3.3 and part of the parameter space provided by surface area  $A$ , volume  $V$  and opening angle  $\alpha$  is shown in figure 3.5. The region of the parameter space where two solutions exist is smaller than the region for the case of only one solution and has complex-shaped boundaries (cf. figures 3.5 and 3.6). When two solutions exist one has a larger height than the other but a smaller radius, e.g. the solution corresponding to the blue shape in figure 3.4 respectively the blue curves

in figure 3.3. In terms of the aspect ratio

$$\Phi = \frac{L}{R + \frac{L}{2} \tan |\alpha|} \quad (3.25)$$

the blue shapes have a larger aspect ratio than the orange shapes as shown in figure 3.3c.

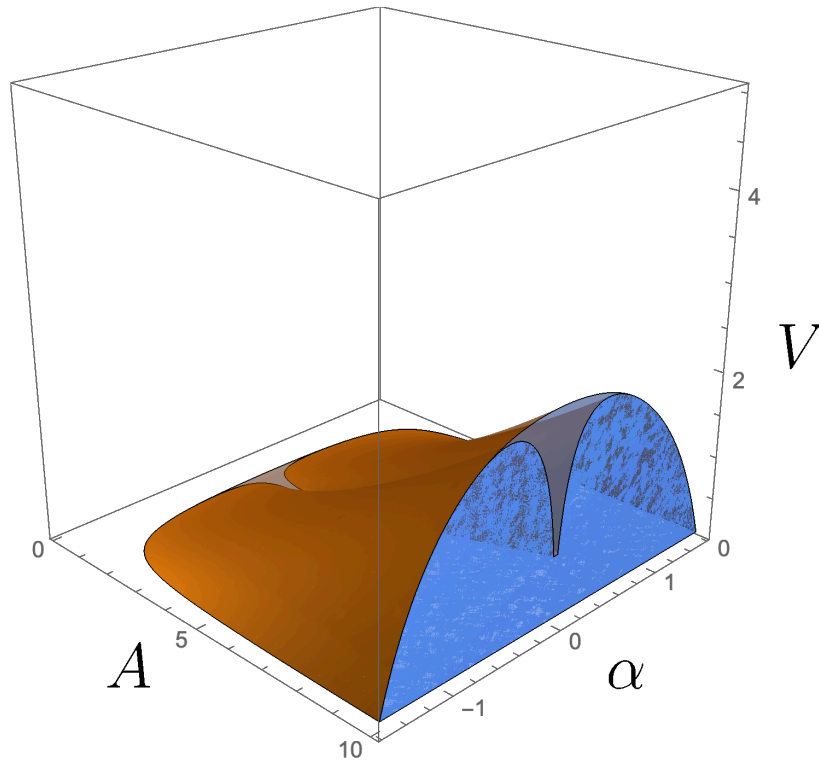


Figure 3.5. Parameter space of equation (3.23). In the transparent region exist two solutions for the height  $L$  and the radius  $R$ , whereas in the solid colored region only one solution exists. These regions are obtained by solving equation (3.23) symbolically using Mathematica<sup>[32]</sup> up to radicals and then plotting the conditions where those solutions exist [\[32\]](#).

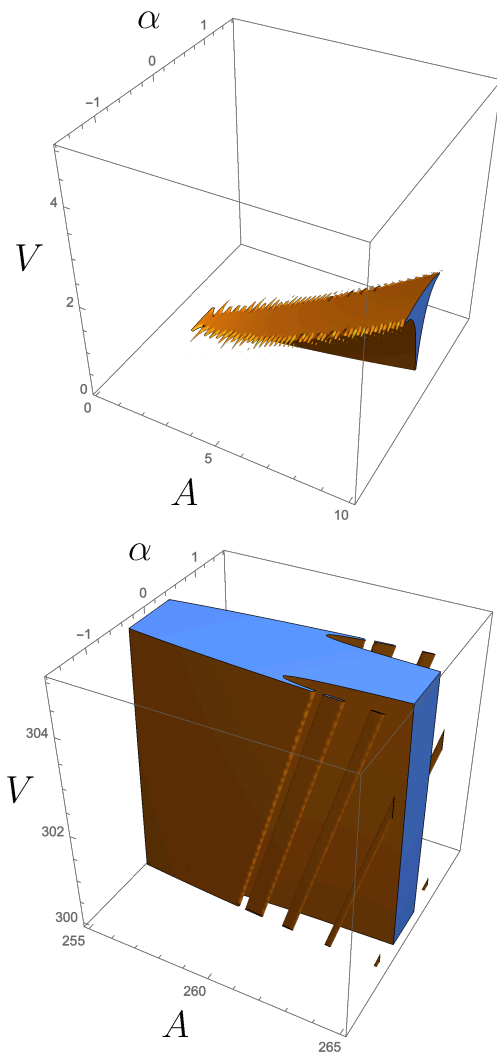



Figure 3.6. Parameter space where two solutions exist (the transparent region of figure 3.5). The boundaries of the region are not smooth but ragged. 

### 3.2.2 Bending energy

The bending energy  $\mathcal{E}_{\text{be}}$  of a cone has two contributions, the bending energy of the shell surface  $\mathcal{E}_{\text{be,s}}$  and the energy of the kinks  $\mathcal{E}_{\text{be,k}}$ .

### 3.2.3 Shell surface

The bending energy of the shell surface can be calculated from the radial profile. The planar caps of the cones are not curved and thus have zero mean curvature, so they only contribute to the bending energy, if the spontaneous curvature is non-zero

$$\begin{aligned}
 \mathcal{E}_{\text{be,s}} &= 2\kappa \int (\mathcal{M} - 2m)^2 dA \\
 &= 4\pi\kappa \int_0^L \left( \frac{1}{2r(z)} - 2m \right)^2 r(z) dz + 2\pi\kappa \left( r^2(0) + r^2(L) \right) m^2 \\
 &= \pi\kappa \left( \cot(\alpha) \log \left( \frac{2R + L \tan(\alpha)}{2R - L \tan(\alpha)} \right) - 8Lm + \left( 16LR + 2R^2 - 2RL \tan \alpha + \frac{L^2}{2} \tan^2 \alpha \right) m^2 \right).
 \end{aligned} \tag{3.26}$$

### 3.2.4 Kinks

The bending energy of a kink is undefined by the traditional definition of curvature, which requires a twice differentiable curve. However, it is obvious that some kinks are more acute than others. Thus, it should be possible to differentiate between differently kinked edges in terms of bending energy. The extreme case of a cone with  $\alpha = \pm\alpha_c$  will be considered first.

### 3.2.5 Spherical cap

In the case of a cone with  $\alpha = \pm\alpha_c$  the kink will be replaced with a spherical cap to get an estimate for the curvature of the kink<sup>[33]</sup>. Without loss of generality it is sufficient to calculate it for the case of  $\alpha = -\alpha_c$ , where point **A** becomes the tip of the cone. The solutions at point **B** can be retrieved by the substitution  $\alpha \rightarrow -\alpha$ . The area

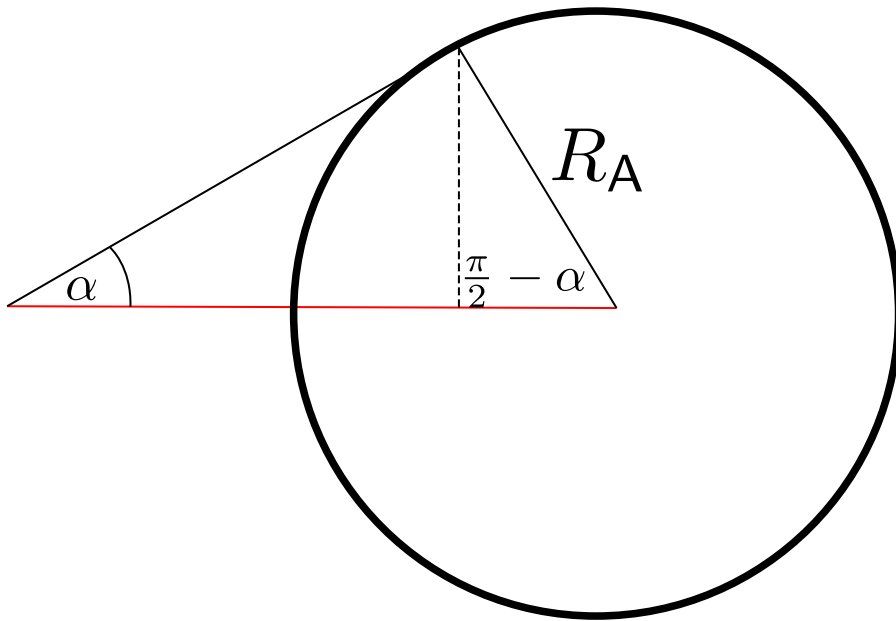


Figure 3.7. The tip of the cone with opening angle  $\alpha$  and the circle of radius  $R_A$ , whose cap replaces the conic cap to calculate the mean curvature.

differential for a spherical cap reads

$$dA_{\text{sphere}} = 2\pi R_A^2 \sin \theta d\theta. \quad (3.27)$$

The mean curvature on any point of the sphere is

$$\mathcal{M}_{\text{sphere}} = \frac{1}{R_A} \quad (3.28)$$

and thus the bending energy (neglecting spontaneous curvature) is

$$\mathcal{E}_{\text{be,k}} = 2\kappa \int \mathcal{M}_{\text{sphere}}^2 dA_{\text{sphere}} = 2\pi \int_0^{\frac{\pi}{2}-\alpha} \sin \theta d\theta = 4\pi\kappa(1 - \sin \alpha). \quad (3.29)$$

### 3.2.6 Toroidal ring

To generalize the ansatz to the case of a truncated cone, the tip of the sphere gets punctuated and stretched to a toroidal segment with a plane disk in between. A torus is characterised by two radii. The radius of the tube will be  $R_A$ , while the distance of the center from the tube to the z-axis is denoted by  $R_{\text{torus}}$ , which has to be calculated.

The mean curvature on any point of the torus is given by<sup>[34]</sup>

$$\mathcal{M}_{\text{torus}} = \frac{R_{\text{torus}} + 2R_A \sin \alpha}{2R_A (R_{\text{torus}} + R_A \sin \theta)} \quad (3.30)$$

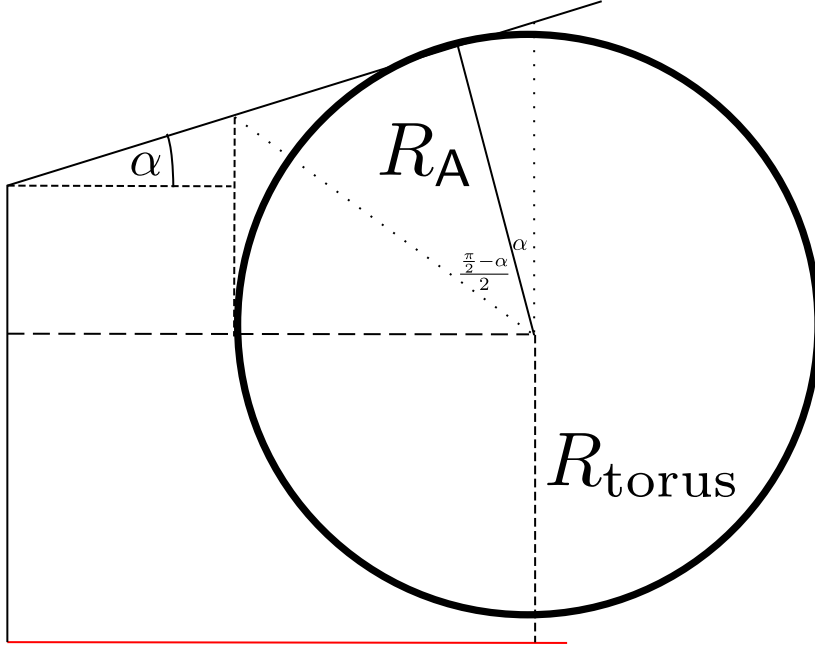


Figure 3.8. The tip of the truncated cone with opening angle  $\alpha$  and the circle of curvature with radius  $R_A$ . The distance of the center of the circle and the symmetry axis of the cone is  $R_{\text{torus}}$ . It is shown in this section that it is not consistently possible to have  $R_{\text{torus}} \neq 0$ .

and the area differential is

$$dA_{\text{torus}} = R_A (R_{\text{torus}} + R_A \sin \theta) d\varphi d\theta. \quad (3.31)$$

The bending energy differential is

$$\begin{aligned} d\mathcal{E}_{\text{be,k}} &= \mathcal{M}_{\text{torus}}^2 dA_{\text{torus}} \\ &= \sin \theta + \frac{R_{\text{torus}}^2}{4R_{\text{torus}}R_A + 4R_A^2 \sin \theta}. \end{aligned}$$

In order for the bending energy to be independent of  $R_A$

$$R_{\text{torus}} = cR_A \quad (3.32)$$

must hold for a constant  $c$  that is yet to be determined. Furthermore, in the extreme cases of a cylinder ( $\alpha = 0$ ) and a proper cone ( $\alpha = -\alpha_c$ ) the radius needs to satisfy

$$\begin{aligned} R_{\text{torus}}(\alpha = 0) &= R - R_A, \\ R_{\text{torus}}(\alpha = -\alpha_c) &= 0. \end{aligned} \quad (3.33)$$

The only way to satisfy these conditions is with  $c = 0$ , which means that the kink still gets approximated by a sphere, whose bending energy is given by equation (3.29) [↗](#).

The energy of both kinks is then given by

$$\mathcal{E}_{\text{be,k}} = \mathcal{E}_{\text{be,k}}(\alpha) + \mathcal{E}_{\text{be,k}}(-\alpha) = 8\pi\kappa. \quad (3.34)$$

### 3.2.7 Total energy

Combining these results, the total bending energy reads

$$\begin{aligned} \mathcal{E}_{\text{be}} &= \mathcal{E}_{\text{be,s}} + \mathcal{E}_{\text{be,k}} \\ &= \pi\kappa \left( \cot(\alpha) \log \left( \frac{2R + L \tan(\alpha)}{2R - L \tan(\alpha)} \right) - 8Lm + \left( 16LR + 2R^2 - 2RL \tan \alpha + \frac{L^2}{2} \tan^2 \alpha \right) m^2 \right) \\ &\quad + 8\pi\kappa. \end{aligned} \quad (3.35)$$

Figure 3.9 shows that the cones with lower aspect ratio are energet-

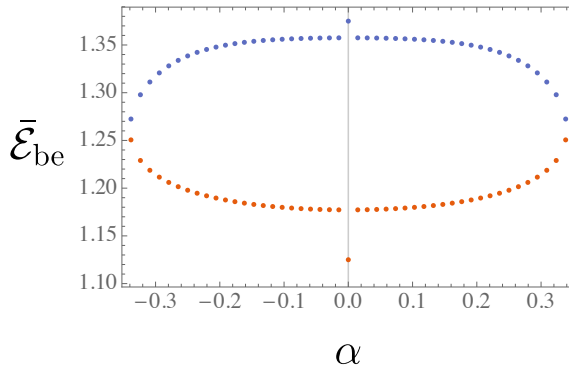


Figure 3.9. Bending energy as given by equation (3.35) of cones with  $V = 1\text{pl}$ ,  $v = 0.8$  and  $m = 0$ . Curves of different color correspond to different solutions for the height  $L$  and the radius  $R$  as shown in figure 3.4.

ically favored with the tube having the lowest energy. For the cones with the larger aspect ratio it is the other way around. Decreasing the volume-to-area ratio  $v$  the difference in the bending energy between the cones with larger aspect ratio and those with lower aspect ratio is becoming larger and larger while the parameter space for cones with larger aspect ratio is increasing and the parameter space for cones with larger aspect ratio is decreasing as shown in figure 3.10.



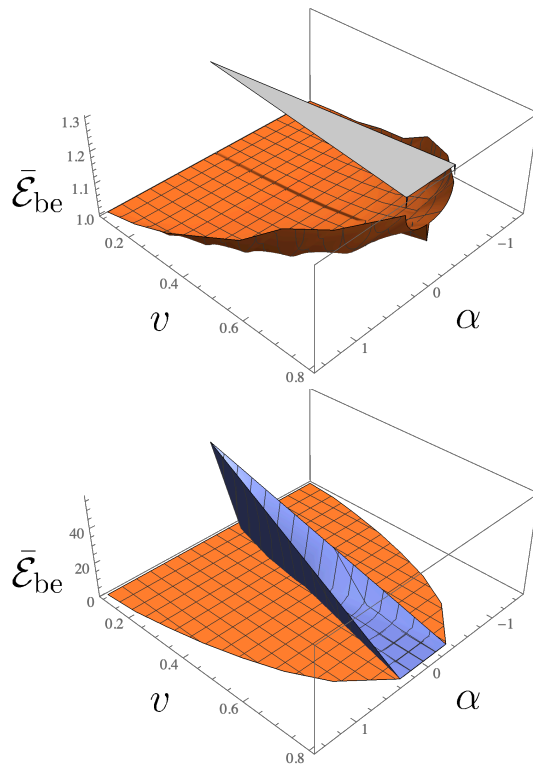


Figure 3.10. Parameter scan of bending energy of cones with  $V = 1\text{pl}$ ,  $v \in ]0, 0.8]$  and  $m = 0$ . Surfaces of different color correspond to the two different solutions for  $L$  and  $R$ .



## 4 Morphologies of uniform vesicles in equilibrium

The equilibrium shapes of uniform vesicles have been studied for a long period of time. Even the simplified models show a rich variety of vesicle shapes and new shapes can still be discovered.

The spontaneous curvature model as explained in section 3.1 is no exception and a large portion of morphologies were explored by Seifert *et al.*<sup>[29]</sup> and Deuling & Helfrich<sup>[35]</sup> by analytic and numeric investigation of the shape equations.

In the following their findings of morphologies for non-negative spontaneous curvature are reviewed. Special focus lies on the formation of necks, since necks lead to compartmentalization of vesicles. Compartmentalization is widely observed in cells of living organisms and plays a crucial role in cell division, endo- and exocytosis.

Finally, additional findings about multi-spherical vesicles that were discovered as part of this thesis are presented in section 4.2.1.

### 4.1 Zero spontaneous curvature

If the spontaneous curvature is zero ( $\bar{m} = 0$ ) four thermodynamically stable morphologies were found: spheres, prolates, oblates and stomatocytes. These shapes can be characterized by their reduced volume  $v$ .

By definition single spheres are only stable for  $v = 1$ . Whereas prolates were found to be stable in the region  $v \in [0.652\dots, 1[$  and

oblates in  $v \in [0.592\dots, 0.651\dots]$ . Finally stomatocytes are stable for  $v \in ]0, 0.591\dots[$  (cf. figure 4.1). The limit shape  $L^{sto}$  at  $v = 0$  corresponds to an inverted sphere<sup>1</sup>, that is connected to a normal sphere by an ideal neck. This shape has a bending energy of  $\mathcal{E}_{be} = 16\pi\kappa$ . The transition between the shapes takes place via discontinuous bifurcations as shown in figure 4.1.

<sup>1</sup> that is a sphere whose surface normals point inwards

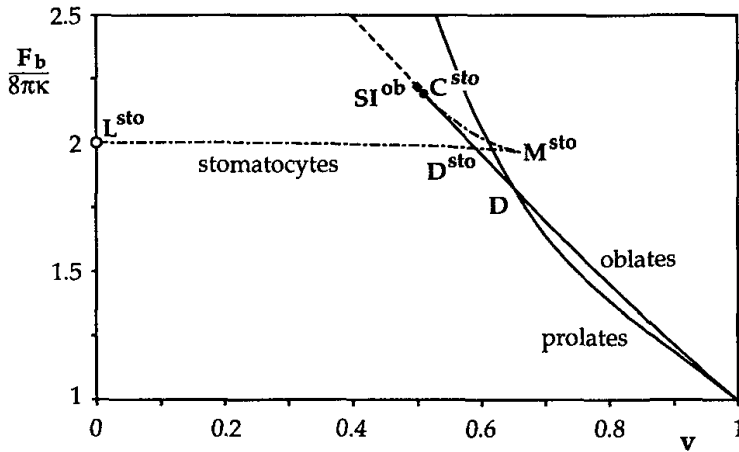
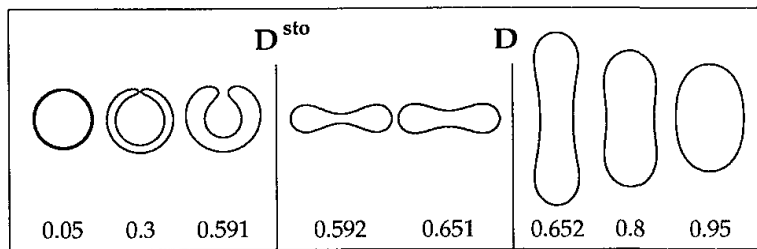


Figure 4.1. Energy diagram for vesicles with zero spontaneous curvature and the corresponding shapes as shown by Seifert *et al.*<sup>[29]</sup>.

Note, that the symbol used by Seifert *et al.*<sup>[29]</sup> for the bending energy is  $F_b$  while in this thesis  $\mathcal{E}_{be}$  is used.

(a) Bending energies for the three branches. Reading from  $v = 1$  to  $v = 0$  prolates are the stable shapes until the discontinuous bifurcation at  $D$ . Between  $D$  and  $D^{sto}$  oblates are the shapes with the minimal bending energy. Finally, stomatocytes are locally stable between  $M^{sto}$  and  $L^{sto}$ , reach its maximum volume at  $M^{sto} \approx 0.66$  and are globally stable between  $D^{sto}$  and  $L^{sto}$ .  $L^{sto}$  denotes the limit shape of a membrane with an inbud that is the same size as the containing sphere and an ideal neck. Solutions of the oblate branch beyond  $SI^{ob}$  begin to self-intersect and are not physically meaningful.



(b) Examples of the thermodynamically stable stomatocytes, oblates and prolates. All shapes have the same area.

## 4.2 Positive spontaneous curvature

Increasing the spontaneous curvature generally leads to shapes with regions that are more narrow and eventually to the formation of necks. Such necks are effectively dividing the vesicle into different compartments. The upcoming section is about vesicles that are a conjunction of spheres. These limit shapes play a special role, since they are connected by a perfect neck, which means that the radius of the neck goes to zero. But having a point where the radius is zero inside of the integration interval when integrating the shape equations (equation (3.16)) is causing numerical instability as well as a discontinuity in the bending angle  $\psi$ . Therefore these shapes are limiting to the exploration of the morphology diagram (cf. figures 4.4 and 4.6) via numerical methods.

### 4.2.1 Regions of spheres

Fortunately, the case of  $n$  spheres connected by a point-like neck can be studied analytically. A neck that connects a sphere of radius  $\bar{R}_1$  to a sphere of radius  $\bar{R}_2$  has to fulfill the neck closure condition<sup>[30]</sup>, which connects the radii of the spheres to the spontaneous curvature  $\bar{m}$

$$\bar{m} \geq \frac{1}{2} \left( \frac{1}{\bar{R}_1} + \frac{1}{\bar{R}_2} \right). \quad (4.1)$$

Using the Euler-Lagrange equation it can be shown<sup>[30]</sup> that each of the  $n$  spheres can only have one of two possible radii, either a small radius  $\bar{R}_s$  or a large radius  $\bar{R}_l$ .

In the following, each configuration of the  $n$  connected spheres is denoted by a specific sequence composed of the letters  $s$  and  $l$ : For example, a large sphere connected to small sphere that is connected to another small sphere is denoted by  $lss$  (cf. figure 4.2). A sphere can be connected to more than two other spheres simultaneously, which is expressed by a prefixed number: As an example,  $l3s$  refers to a large sphere connected to three small spheres.

Note that the shapes that contain a number don't have rotational symmetry in general and thus cannot be described by the shape equations. The only exceptions are  $l2s$  and  $s2l$ , which are equivalent to  $sls$  (cf. figure 4.3) and  $lsl$  respectively.

In order for the whole conformation to be stable all necks have to be stable. As a consequence of equation (4.1) the neck with the most spheres of radius  $\bar{R}_s$  will determine the lower bound of possible  $\bar{m}$  values.

The boundary of a region where  $n$  spheres are connected of which  $n_s$  spheres have the radius  $\bar{R}_s$  and  $n_l$  have the radius  $\bar{R}_l$  can be calculated via

$$\bar{R}_s = \begin{cases} \frac{1}{\bar{m}} & \text{if at least one } ss\text{-neck exists} \\ \frac{1}{\sqrt{n}} & \text{if } \bar{R}_s = \bar{R}_l \\ \frac{\bar{R}_l}{2\bar{m}\bar{R}_l - 1} & \text{else,} \end{cases}$$

$$1 = n_l \bar{R}_l^2 + n_s \bar{R}_s^2,$$

$$v = n_l \bar{R}_l^3 + n_s \bar{R}_s^3. \quad (4.2)$$

Solving these equations will give unique solutions for  $n = n_l + n_s$  spheres. The large radius can have values in  $\bar{R}_l \in [\frac{1}{\sqrt{n}}, 1]$  and the small radius in  $\bar{R}_s \in [0, \frac{1}{\sqrt{n}}]$ . The lowest possible value of the reduced volume  $v$  is reached when  $\bar{R}_l = \bar{R}_s$  which leads to  $v_{\min}(n) = \frac{1}{\sqrt{n}}$ . The maximal value of the reduced volume,  $v_{\max}(n_l) = \frac{1}{\sqrt{n_l}}$ , is reached in the limit  $\bar{R}_s \rightarrow 0$ . Note, that the shape only varies with the volume-to-area ratio  $v$  and not with the spontaneous curvature  $\bar{m}$ , while the bending energy is minimal for

$$\bar{m}_{\min}(v) = \frac{1}{2} \left( \frac{1}{\bar{R}_s} + \frac{1}{\bar{R}_l} \right) \quad (4.3)$$

and increases with larger  $\bar{m}$ . Thus, shapes observed in experiments most likely have a spontaneous curvature close to  $\bar{m}_{\min}(v)$ . The boundary line  $v(\bar{m})$  depends on the type of necks present for a given configuration.

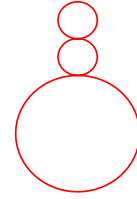


Figure 4.2. A multisphere  $lss$  solution consisting of one large and two small spheres at  $\bar{m} = 2\sqrt{3}$  and  $v = \frac{10\sqrt{10}+2}{24\sqrt{3}} \approx 0.809\dots$

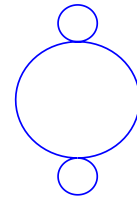


Figure 4.3. A multisphere  $l2s$  solution consisting of one large and two small spheres at  $\bar{m} = 2\sqrt{3}$  and  $v = 0.925\dots$

Figure 4.4 shows the resulting boundaries for  $n = 2$  (black),  $n = 3$  (blue) and  $n = 4$  (red). Each color has different branches for those configurations that have the same neck constraint corresponding to the cases in equation (4.2) and the same number of small spheres  $n_s$ . For example the two configurations  $lsl$  and  $lls$  both contain a  $ls$ -neck and have  $n_s = 1$  and thus approach the limit shape  $ll$ , while the configuration  $sls$  also contains a  $ls$ -neck, but since  $n_s = 2$  it approaches the limit shape  $l$  in the limit  $\bar{m} \rightarrow \infty$ .

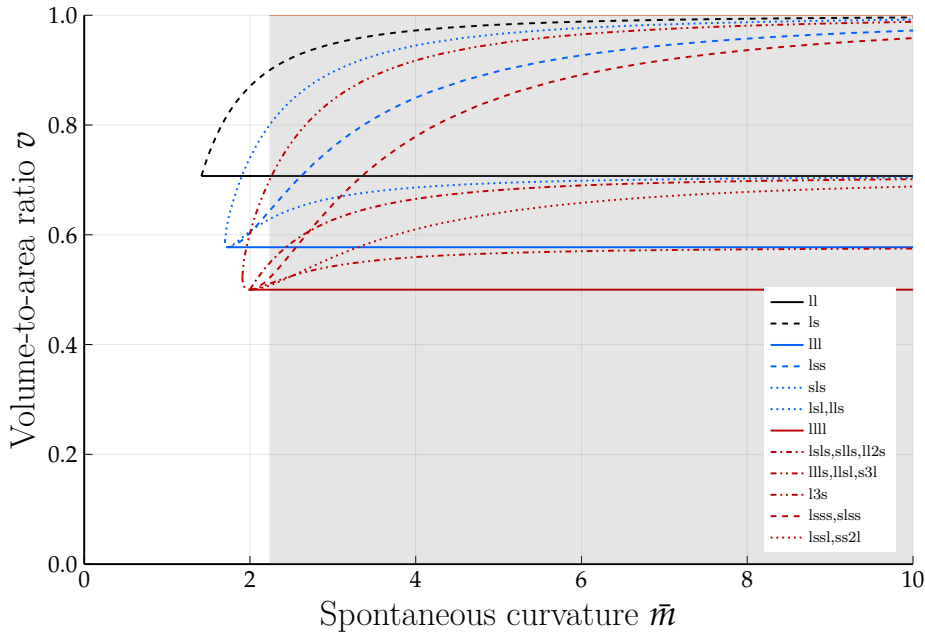


Figure 4.4: Regions of existence for multi-sphere solutions for 2 (—), 3 (—) and 4 (—) spheres in the plane spanned by the reduced volume  $v$  and the dimensionless spontaneous curvature  $\bar{m}$ . Labels that are mirror images of each other are omitted. So labels like  $ls$  include its mirror image  $sl$ . In the case where all spheres are of the same size the label with all  $l$ 's is used, while using  $s$  would be equally valid. The gray region starting at  $\bar{m} = \sqrt{5}$  indicates the region where more than 4 spheres are connected. These additional lines are omitted for the sake of readability but still cover a large enough interval such that the asymptotics of the boundaries are clear.

In the interval  $\bar{m} \in [0, 10]$  100 families of curves would have to be displayed otherwise. Note that the  $l3s$  line corresponds to non-axisymmetric solutions that can not be described by the shape equations.

### 4.2.2 Breaking of symmetry

Prolates and oblates with zero spontaneous curvature are in addition to their rotational symmetry symmetric with respect to a plane that crosses the axis of rotation in its center (see figure 4.5).

However, in experiments, deflation of vesicles typically leads to the formation of buds<sup>[36]</sup>, which were discussed in section 4.2.1(cf. figures 4.2 and 4.3). These multi-sphere vesicles do not have this additional symmetry and might not even be axisymmetric. As shown in figure 4.4 multi-sphere vesicles exist for larger values of the spontaneous curvature in the morphology diagram. The fact, that they do occur for the same value of the reduced volume as the symmetric prolates, indicates that there has to be a transition region.

Indeed, Seifert *et al.*<sup>[29]</sup> reported such a transition region for the case of two connected spheres. Figure 4.6 shows this region between the lines  $D^{\text{pear}}$  and  $L_{1+1}$ . The line  $D^{\text{pear}}$  describes a discontinuous transition between prolates with two symmetry axes and prolates with one symmetry axis. The line  $L_{1+1}$  is identical to the line labeled as  $l_s$  in figure 4.4. The asymptotic behaviour when the spontaneous curvature goes to infinity ( $\bar{m} \rightarrow \infty$ ) can be calculated by solving the equation<sup>[29]</sup>

$$v = \frac{2\bar{m}(4 - 3(\bar{R}_s + \bar{R}_l)) - 3}{2(\bar{m} - 3)}, \quad (4.4)$$

where  $\bar{R}_s$  and  $\bar{R}_l$  are given by equation (4.2) for  $n_l = n_s = 1$ . The lower solid part of the line  $D^{\text{pear}}$  was obtained by numerically tracking the point where the shapes of the symmetric and asymmetric branch have equal energy. The dotted lines correspond to cubic splines that connect the numeric and analytic solutions.

The line of limit shapes that have two spheres with different radii  $L_{1+1}$  is described by the functional relationship<sup>[29]</sup>

$$v = v_{1+1}(\bar{m}) \equiv -\frac{1}{4\bar{m}^3} + \left(1 - \frac{1}{2\bar{m}^2}\right) \sqrt{1 + \frac{1}{4\bar{m}^2}} \quad \text{for } \bar{m} \geq \sqrt{2}. \quad (4.5)$$

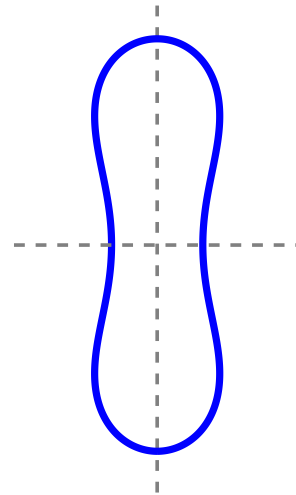


Figure 4.5. Symmetry axes of a prolate with  $\bar{m} = 0$  and  $v = 0.7$ .



The line of limit shapes that have two spheres of equal radius  $L_{2^*}$  is located at<sup>[30]</sup>

$$v = v_* \equiv \frac{1}{\sqrt{2}} \approx 0.707 \quad \text{and} \quad \bar{m} \geq m_* \equiv \sqrt{2} \approx 1.414. \quad (4.6)$$

The two boundary lines meet in a corner point with  $\bar{m} = \bar{m}_* = \sqrt{2}$  and  $v = v_* = 1/\sqrt{2}$ . At this corner point of the morphology diagram, the dumbbell shape consists of two equally sized spheres with radius  $\bar{R}_s = \bar{R}_l = 1/\sqrt{2}$  and vanishing bending energy. Transitions

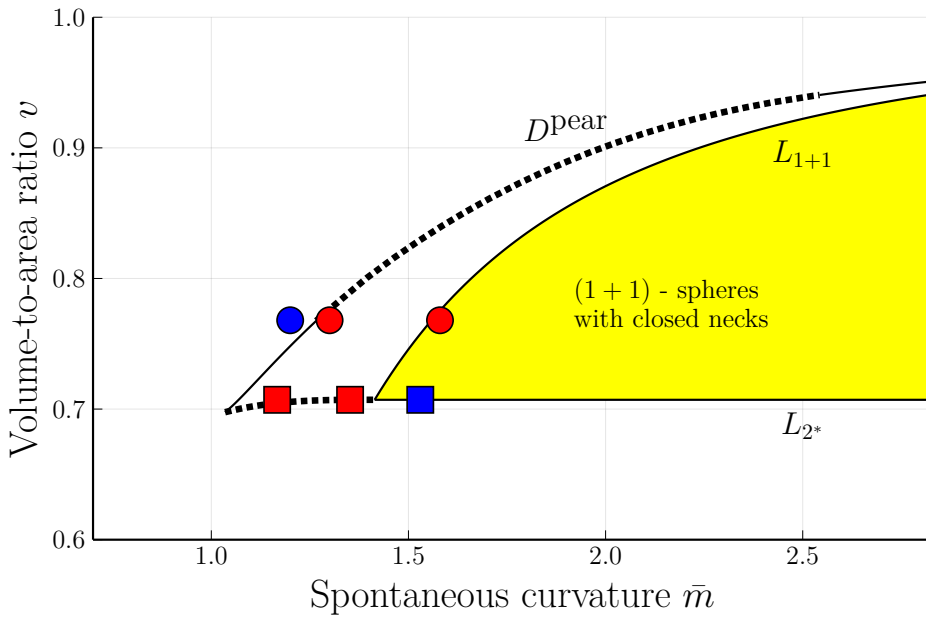


Figure 4.6: Morphology diagram of prolates and dumbbells for positive spontaneous curvature  $\bar{m}$  with  $0.7 \leq \bar{m} \leq 2.8$  and volume-to-area ratio  $v \geq 0.6$ . The horizontal line with  $v = 1$  corresponds to a single sphere. Along the solid line  $L_{1+1}$ , the vesicles form limit shapes consisting of two different spheres connected by a closed membrane neck. The location of this line is given by the algebraic expression in equation (4.5). Along the solid line  $L_{2^*}$  with  $v = 1/\sqrt{2} \approx 0.707$  and  $\bar{m} \geq \sqrt{2}$ , the vesicles consist of two equally sized spheres connected by a closed neck. The parameter region between the two lines  $L_{1+1}$  and  $L_{2^*}$  defines the yellow stability regime for  $(1+1)$ -spheres, in which the vesicle shape depends only on  $v$  but is independent of  $\bar{m}$ . The black dotted line  $D^{\text{pear}}$  separates up-down symmetric from asymmetric dumbbells with open necks. The latter line is obtained using cubic splines to connect numerical and analytical solutions. The solid blue and red circles correspond to shapes with  $v = 0.768$  as displayed in figure 4.7a, the solid red and blue squares to shapes with  $v = 1/\sqrt{2}$  as in figure 4.7b. Red markers correspond to asymmetric shapes and blue markers to symmetric shapes.

from fully symmetric prolates to prolates that are only axisymmetric were found to happen discontinuously whereas the transition of these prolates into two connected spheres is continuous<sup>[29]</sup>. Solutions with

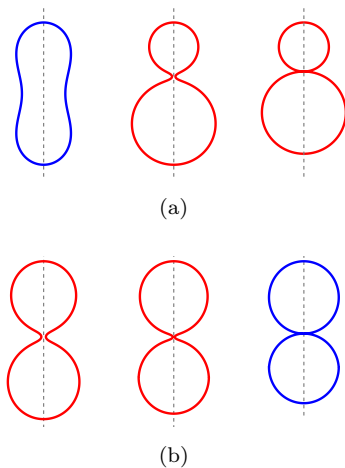


Figure 4.7: Examples for dumbbell shapes with open and closed necks: (a) Dumbbells with  $v = 0.768$ , corresponding to the three solid circles in figure 4.6. From left to right, these shapes have the rescaled spontaneous curvatures  $\bar{m} = 1.2, 1.3$  and  $\geq 1.56$ , where the rightmost shape corresponds to the limit shape  $L_{1+1}$  with  $v = 0.768$ ; (b) Dumbbells with  $v = v_* = 1/\sqrt{2} = 0.707$  corresponding to the three solid squares in figure 4.6. From left to right, these shapes have the spontaneous curvature  $\bar{m} = 1.167, 1.352$ , and  $\bar{m} \geq \bar{m}_* = \sqrt{2} = 1.414$ . The two shapes with  $\bar{m} = 1.352$  and  $\bar{m} = \bar{m}_*$  are unduloids as explained in section 4.3, while the other shapes are solutions of the shape equations.

broken symmetry have a significantly lower minimum of the radial coordinate than their symmetric counterpart (cf. figure 4.7a). This means that for fixed volume-to-area ratio  $v$  narrow necks can occur for lower values of the spontaneous curvature  $\bar{m}$  if the symmetry perpendicular to the axis of rotation is broken <sup>2</sup>.

<sup>2</sup> See also figures 5.4 and 5.5

### 4.3 Bridging the gap - parameterization for narrow necks

As the neck closes, solving the shape equations becomes more and more difficult because of numerical instabilities when the neck radius goes to zero. For narrow necks a prolate can be approximated by two spherical caps joined by two unduloid segments<sup>[37]</sup>. This approximation has the advantage that it can be treated analytically.

The parameterization consists of four regions. The first region is a spherical cap with radius  $\bar{R}_s$ <sup>3</sup> and curvature  $\psi(\mathbf{s}) = \frac{1}{\bar{R}_s}$  between  $\mathbf{s}_0 = 0$  and  $\mathbf{s}_1 = \frac{\pi}{2}\bar{R}_s$ . The second region connects the spherical cap with radius  $\bar{R}_s$  with the neck of radius  $\bar{R}_{ne}$  with an unduloid segment,

<sup>3</sup> without loss of generality, it can be assumed that the first spherical segment is smaller than the second

while the third region connects the neck to the second spherical cap of radius  $\bar{R}_l$ .

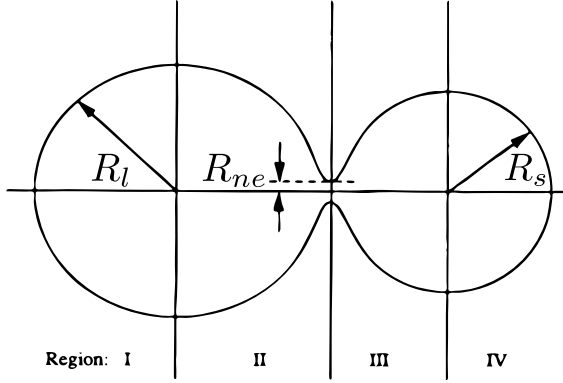


Figure 4.8. Illustration of the four regions of the approximation for dumbbell shaped vesicles with narrow necks. Region I is a spherical cap with radius  $\bar{R}_l$  and region IV a spherical cap with radius  $\bar{R}_s$ . Region II and III are unduloids whose parameterization is given by equation (4.7).<sup>[37]</sup>

The parameterization of the unduloid segments as shown by Fourcade *et al.*<sup>[37]</sup> reads

$$\sin \psi(s) = \frac{1}{\bar{R}_i + \bar{R}_{ne}} \left( \bar{r}(s) + \frac{\bar{R}_i \bar{R}_{ne}}{\bar{r}(s)} \right) \quad i \in \{s, l\}, \quad (4.7)$$

where  $i = s$  in the second region and  $i = l$  in the third. By taking the derivative with respect to the arc-length  $s$  the curvature  $\dot{\psi}(s)$  can be calculated:

$$\begin{aligned} \dot{\psi}(s) &= \frac{\pi \bar{S}}{\bar{R}_i + \bar{R}_{ne}} \left( 1 - \frac{\bar{R}_i \bar{R}_{ne}}{r^2(s)} \right) \quad i \in \{s, l\}, \\ \dot{r}(s) &= \pi \bar{S} \cos(\psi(s)). \end{aligned} \quad (4.8)$$

The fourth region is a spherical cap of radius  $\bar{R}_l$  and curvature  $\dot{\psi}(s) = \frac{1}{\bar{R}_l}$  from  $s = 1 - \frac{\bar{R}_l}{2\bar{S}}$  to  $s = 1$ .

The total area  $A_u$  and volume  $V_u$  of shapes consisting of all four regions are given by<sup>[37]</sup>

$$\begin{aligned} A_u &= 4\pi \left( \bar{R}_l^2 + \bar{R}_s^2 \right) + 2\pi \bar{R}_{ne} \left( \bar{R}_l + \bar{R}_s \right) + \mathcal{O}(\bar{R}_{ne}^2 \log(\bar{R}_{ne})), \\ V_u &= \frac{4\pi \left( \bar{R}_l^3 + \bar{R}_s^3 \right)}{3} + \pi \bar{R}_{ne} \left( \bar{R}_l^2 + \bar{R}_s^2 \right) + \mathcal{O}(\bar{R}_{ne}^2). \end{aligned} \quad (4.9)$$

## 4.3.1 Matching to shape equations

When starting with a shape that has a reduced volume  $v = 1/\sqrt{2}$  and a spontaneous curvature  $\bar{m} = 0$  and approaching the limit shape  $L_{2^*}$  at  $v = 1/\sqrt{2}$  and  $\bar{m} = \sqrt{2}^4$ , the numerical instability of the closing neck eventually causes the algorithm to fail. The last available shape obtained by solving the shape equations is at  $\bar{m} = 1.306$ . Using the values of the area and the volume of this solution,  $\bar{R}_l$  and  $\bar{R}_s$  are calculated via (4.9) using a root finding algorithm. Here, the trust-region algorithm provided by `NLsolve.jl`<sup>[38]</sup> was used. The neck radius was computed by finding the minimum between the two maxima of the radial component of the solution. The values are  $\bar{R}_{ne} \approx 0.023$ ,  $\bar{R}_l \approx 0.723$  and  $\bar{R}_s \approx 0.679$ . These values are then used to obtain an unduloid shape via equation (4.8). The resulting relative error is below 2% for area and volume with respect to the solutions of the shape equations (cf. figure 4.9).

<sup>4</sup>this is the egde of the yellow region in figure 4.6

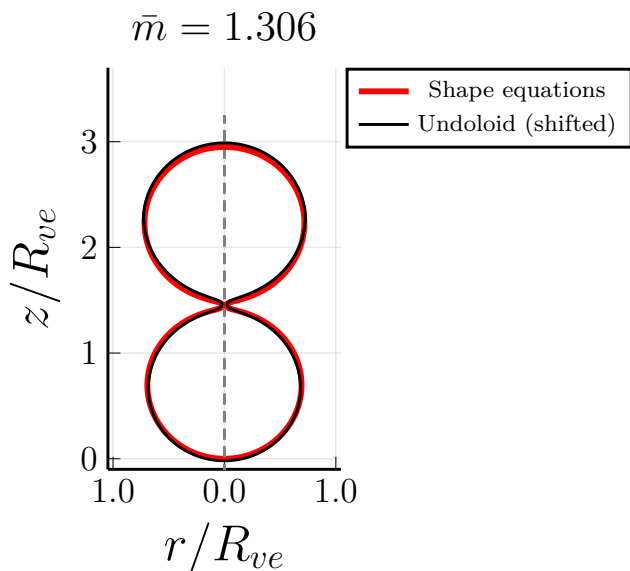


Figure 4.9. Fitting of parameterization at  $\bar{m} = 1.306$  and  $v = 1/\sqrt{2}$ . The solution of the shape equations is shown in red and the unduloid parameterization with the same neck radius  $\bar{R}_{ne} \approx 0.023$  is shown in black. The unduloid shape was slightly shifted in  $z$  direction to be symmetric relative to the solution of the shape equations.

## 4.3.2 Closing neck interpolation

As shown in figure 4.6, an ideal neck with  $\bar{R}_{ne} = 0$  connecting two spheres of equal radius  $\bar{R}_l = \bar{R}_s = \frac{1}{\sqrt{2}}$  forms at  $\bar{m} = \sqrt{2}$ . The neck radius can now be linearly interpolated between  $\bar{R}_{ne} \approx 0.023$  and 0,

which yields

$$\bar{R}_{\text{ne}}(\bar{m}) \approx 0.3005 - 0.2125\bar{m}. \quad (4.10)$$

For any  $\bar{m}$ , the values of  $\bar{R}_s$  and  $\bar{R}_l$  can be calculated from equation (4.9) as in section 4.3.1.

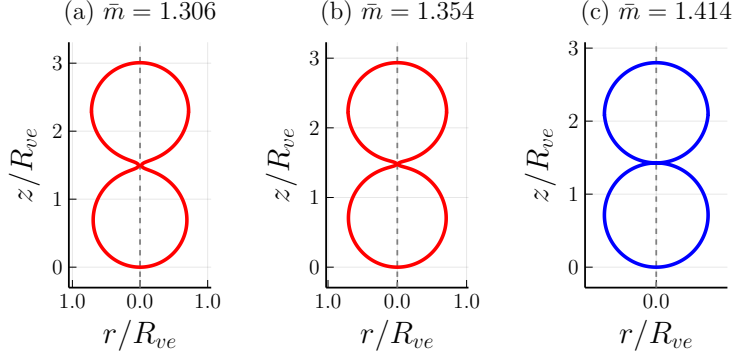


Figure 4.10. Contours corresponding to the linear interpolation in equation (4.10). (a) The same contour as in figure 4.9 with  $\bar{R}_{\text{ne}} \approx 0.023$ . (b) Intermediate shape with  $\bar{R}_{\text{ne}} \approx 0.013$ . (c) Limit shape with a closed neck  $\bar{R}_{\text{ne}} = 0$ .



## 5 *Non-equilibrium shape transformations*

### 5.1 *Shape oscillations in GUVs filled with min-proteins*

The previous section dealt with the different shapes of axisymmetric vesicles as they can be computed using the spontaneous curvature model. In this section this model is used to analyse the shapes of GUVs in vitro and thus provide a way to estimate spontaneous curvature and neck radii below the optical limit.

#### 5.1.1 *The experiment*

In the experiment by Litschel *et al.*<sup>[6]</sup> fluorescently labeled GUVs were produced via continuous droplet interface crossing encapsulation (cDICE)<sup>[39]</sup> and observed simultaneously by differential interference contrast microscopy (DIC) and confocal fluorescence microscopy. The aqueous buffer enclosed by the GUVs contained two Min proteins, MinD and MinE, as well as adenosine triphosphate (ATP) and enhanced green fluorescent proteins (eGFPs). The corresponding solution concentrations were 1.5  $\mu\text{M}$  MinD, 1.4  $\mu\text{M}$  eGFP-MinD, 3  $\mu\text{M}$  MinE, and 5 mM ATP.<sup>[6]</sup> Thus, about half of the MinD proteins were fluorescently labeled and the overall MinD concentration was roughly equal to the MinE concentration. The lipid bilayer of the GUVs was composed of zwitterionic 1,2-Dioleoyl-sn-glycero-3-phosphocholine (DOPC) and anionic 1,2-Dioleoyl-sn-glycero-3-phosphoglycerol (DOPG) in a ratio of 4:1.


MinD adsorbs onto lipid membranes when loaded with ATP.<sup>[40]</sup> MinE binds to membrane-bound MinD-ATP and the resulting MinD-ATP-


MinE complex stimulates ATP hydrolysis by MinD, causing both proteins to desorb again from the membrane. In the presence of a sufficient amount of ATP, this MinD-MinE system undergoes many repetitive cycles of adsorption and desorption. For osmotically deflated vesicles, this periodic molecular process leads to shape oscillations of the vesicles which can be directly observed in the optical microscope.<sup>[6]</sup> Different types of shape oscillations have been detected; the two most frequent types of oscillations were denoted by ‘periodic dumbbell splitting’ and ‘periodic budding’ in Ref. 6.

The analysis in this section focuses on the dumbbell case as displayed in figures 5.1 and 5.2. In this case, the fluorescence of the eGFP-labeled MinD adjacent to the inner leaflet of the GUV membrane was observed to be laterally uniform. Therefore, membrane segments with a lateral extension of about  $300 \text{ nm}$ <sup>1</sup> can be considered to have, on average, a laterally uniform molecular composition which implies that they have uniform elastic properties as well. As shown in chapter 4, the shape of uniform GUV membranes strongly depends on spontaneous curvature of these membranes.<sup>[41]</sup>

<sup>1</sup> this corresponds to the limit of optical resolution

### 5.1.2 Analysis

The theoretical analysis is based on the time-lapse Movie1  which consists of 200 snapshots or frames, each of which displays a different image of the same GUV as obtained by differential interference contrast microscopy. The movie was taken with the predefined time interval  $\Delta t = 7.61 \text{ s}$  between successive frames and displays the whole series of 200 frames within 20 s, corresponding to about 1500 s or 25 min real time. Apart from a few frames at the beginning and at the end, the movie consists of 26 complete shape oscillations with an average time period of 55.9 s as described in more detail further below.

All individual snapshots of Movie1  are consistent with the view that the observed shapes represent essentially axisymmetric shapes that are tilted with respect to the focal plane and are deformed by



relative displacements of the two subcompartments with respect to the closed membrane neck, which acts as a flexible hinge. The two shape sequences in figure 5.1a-c and figure 5.2a-c have been selected as good candidates to be analyzed because they can be well approximated by axisymmetric shapes without additional deformations arising from relative displacements around the hinge-like membrane neck.

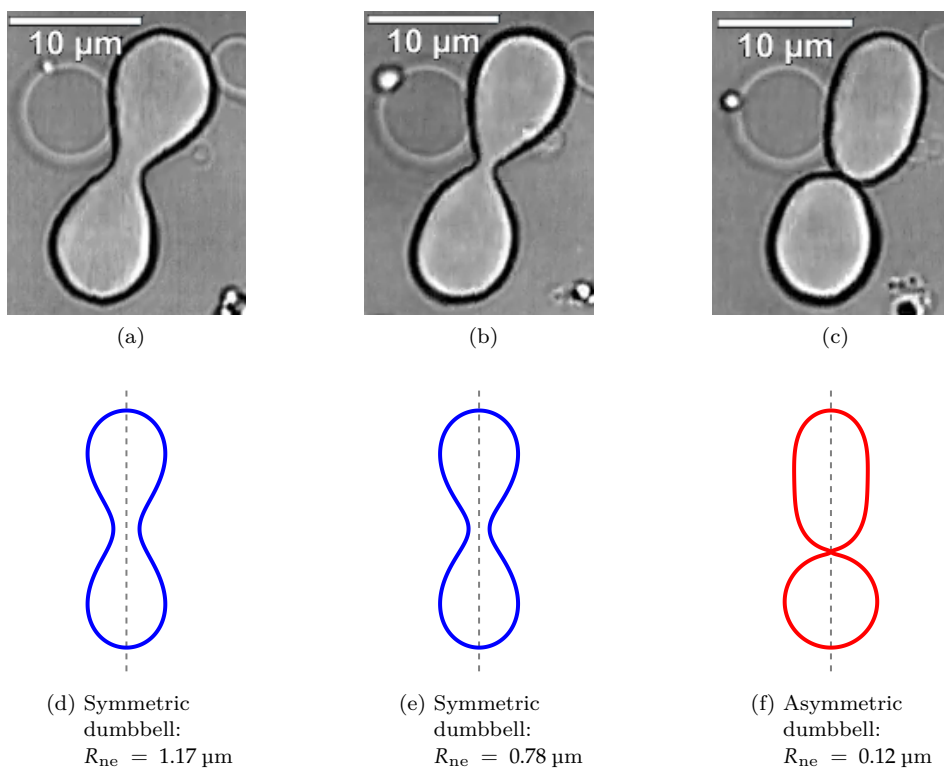


Figure 5.1. Symmetry-breaking transformation during one shape oscillation: Comparison of experimentally observed vesicle shapes in (a-c) with theoretically calculated shapes in (d-f) that match the neck radius measured from the corresponding experimental images. The neck radius  $R_{ne}$  attains its largest value of  $1.17 \mu\text{m}$  in (a,d) and its smallest value of  $0.12 \mu\text{m}$  in (c,f). The up-down symmetry of the symmetric dumbbells (blue shape contours) in (a,d) and (b,e) is broken for the asymmetric dumbbell (red shape contour) in (c,f). The three images in panels a-c were obtained by differential interference contrast microscopy<sup>[6]</sup> and represent three subsequent frames of the time-lapse Movie1. The dashed vertical lines in panels d-f represent axes of rotational symmetry.<sup>[41]</sup>

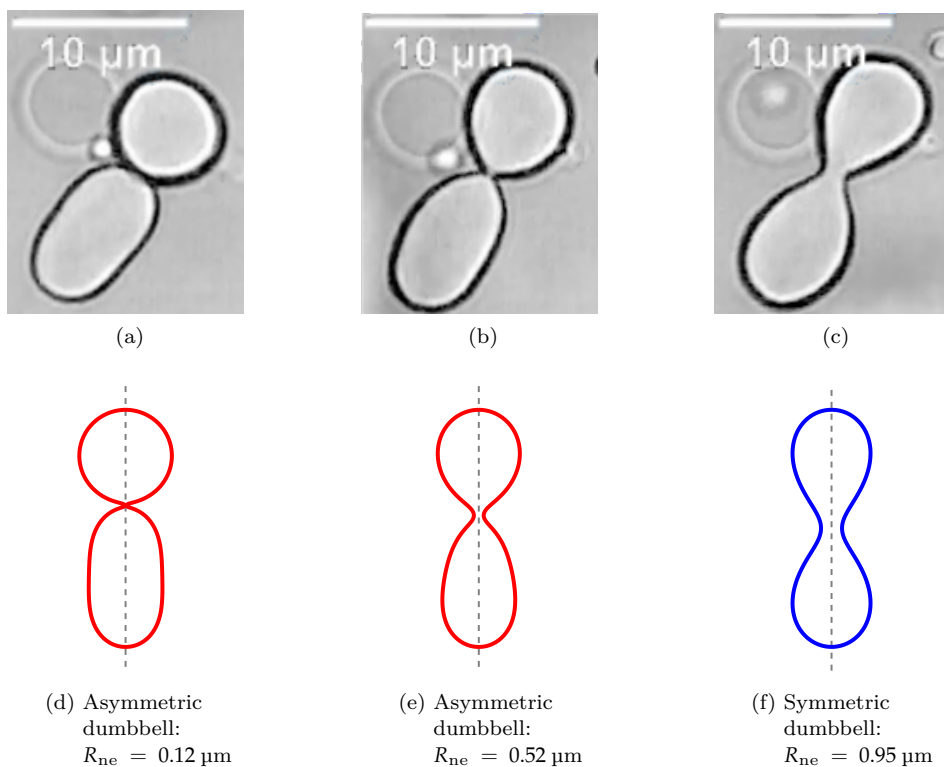


Figure 5.2. Symmetry-restoring transformation during one shape oscillation: Comparison of experimentally observed vesicle shapes in (a-c) with theoretically calculated shapes in (d-f). The neck radius  $R_{ne}$  attains its smallest value of  $0.12 \mu\text{m}$  in (a,d) and its largest value of  $0.95 \mu\text{m}$  in (c,f). The up-down symmetry is broken for the red shapes of (a,d) but restored for the blue shape of (c,f). The asymmetric shape in (a,d) is the same shape as in figure 5.1c,f but flipped upside-down. The three images in panels a-c represent three subsequent frames of the time-lapse Movie1.<sup>[41]</sup>

During the observed shape changes, both the membrane area and the volume of the GUVs were essentially conserved. These properties were explicitly demonstrated for the six snapshots in figure 5.1a-c and figure 5.2a-c by manually fitting splines to the shape contours of these images, assuming rotational symmetry of the shapes, and then measuring the membrane area  $A$  and the vesicle volume  $V$  as well as the neck radius  $R_{\text{ne}}$ .<sup>[1,42]</sup> The numerical estimates for these geometric quantities are given in table 5.1.

	$A$ [ $\mu\text{m}^2$ ]	$V$ [ $\mu\text{m}^3$ ]	$v$	$R_{\text{ne}}$ [ $\mu\text{m}$ ]
Fig. 5.1a	$390 \pm 30$	$490 \pm 60$	$0.68 \pm 0.01$	$1.1 \pm 0.2$
Fig. 5.1b	$380 \pm 30$	$470 \pm 60$	$0.68 \pm 0.01$	$0.8 \pm 0.2$
Fig. 5.1c	$380 \pm 30$	$460 \pm 50$	$0.66 \pm 0.02$	$< 0.3$
Fig. 5.2a	$380 \pm 30$	$470 \pm 53$	$0.67 \pm 0.01$	$< 0.3$
Fig. 5.2b	$380 \pm 30$	$463 \pm 52$	$0.68 \pm 0.01$	$0.6 \pm 0.2$
Fig. 5.2c	$380 \pm 30$	$483 \pm 55$	$0.68 \pm 0.01$	$0.9 \pm 0.2$

Table 5.1: Membrane area  $A$ , vesicle volume  $V$ , dimensionless volume-to-area ratio  $v$  defined in equation (3.7), and neck radius  $R_{\text{ne}}$ , as estimated from the optical images in figure 5.1a-c and figure 5.2a-c via fitting with splines. In the third and fourth row, the upper bound for  $R_{\text{ne}}$  corresponds to the optical resolution of differential interference contrast microscopy. The error of the spline fitting was estimated with  $\pm 2$  pixels which corresponds to  $\pm 132\text{nm}$  and the uncertainties of the displayed values is obtained by linear error propagation using Measurements.jl<sup>[43,44]</sup>.<sup>[41]</sup>

	$v$	$\bar{m}$	$\bar{R}_{\text{ne}}$	$m$ [ $\mu\text{m}^{-1}$ ]	$R_{\text{ne}}$ [ $\mu\text{m}$ ]
Fig. 5.1d	0.670	1.18	0.21	0.21	1.17
Fig. 5.1e	0.670	1.63	0.14	0.29	0.78
Fig. 5.1f	0.670	1.89	0.021	0.34	0.12
Fig. 5.2d	0.670	1.89	0.021	0.34	0.12
Fig. 5.2e	0.670	1.93	0.094	0.35	0.52
Fig. 5.2f	0.670	1.40	0.17	0.25	0.95

Table 5.2: Dimensionless shape parameters  $v$  and  $\bar{m}$  that were used to compute the dumbbell shapes in figure 5.1d-f and figure 5.2d-f, see also figure 5.4. The third column contains the rescaled neck radius  $\bar{R}_{\text{ne}} = R_{\text{ne}}/R_{\text{ve}}$  of the computed shapes. The spontaneous curvature  $m = \bar{m}/R_{\text{ve}}$  and the neck radius  $R_{\text{ne}} = \bar{R}_{\text{ne}} R_{\text{ve}}$  in the fourth and fifth column were computed using the vesicle size  $R_{\text{ve}} = \sqrt{A/(4\pi)} = 5.57 \mu\text{m}$  as obtained from the membrane area  $A = 390 \mu\text{m}^2$  for the image in figure 5.1a.<sup>[41]</sup>

The theoretical shapes in figure 5.1d-f and figure 5.2d-f were then calculated using the volume-to-area ratio  $v = 0.670$  and several values of the rescaled spontaneous curvature  $\bar{m}$  as given in table 5.2 and displayed in the morphology diagram of figure 5.4. These values of the spontaneous curvature were chosen by measuring the neck radius

of the experimental shapes and comparing them to the radii of the computed shapes as shown in figure 5.7. Furthermore, to obtain the dimensionful quantities from the dimensionless ones, the vesicle size  $R_{\text{ve}} = \sqrt{A/(4\pi)} = 5.57 \mu\text{m}$  as obtained from the area  $A = 390 \mu\text{m}^2$  of the image in figure 5.1a was used, see first row in table 5.1.

### 5.1.3 Finding shapes assuming $v = 0.670$

The symmetric and asymmetric dumbbells as displayed in figure 5.5 were obtained by numerical solution of the shape equations as explained in more detail in appendix B. The region of the morphology diagram that was traversed is displayed in figure 5.3. These shapes belong to two different branches of the bending energy  $\mathcal{E}_{\text{be}}$  as shown in figure 5.6. The branch of the asymmetric shapes is connected to the branch of the symmetric shapes by a continuous bifurcation  $B_{\text{op}}$ . From this point on the neck radius decreases until it reaches the limit shape of a sphere connected to a prolate. This limit shape is labeled by the symbol  $L_{\text{ps}}$ . As visible in figures 5.6 and 5.7, the two branches of shapes coexist in a rather narrow interval of values for the spontaneous curvature with  $\bar{m}(L_{\text{ps}}) < \bar{m} < \bar{m}(B_{\text{op}})$ . From extrapolation of the neck radii of the computed shapes  $\bar{m}(L_{\text{ps}}) \simeq 1.84$  is estimated as indicated by the red star in figure 5.7. The bifurcation value of the spontaneous curvature for the continuous bifurcation  $\bar{m} = \bar{m}(B_{\text{op}})$  is given by the point where the energy of both shapes is equal. From the shapes shown in figure 5.5 it is concluded that the value of  $\bar{m}(B_{\text{op}})$  is in the interval  $]1.933, 1.94[$ . The continuous bifurcation at the point  $B_{\text{op}}$  is confirmed by the functional form of the bending energy, see inset in figure 5.6.

The latter inset displays the rescaled bending energy difference

$$\Delta\bar{\mathcal{E}}_{\text{be}} \equiv (\bar{\mathcal{E}}_{\text{be}}^{\text{asym}} - \bar{\mathcal{E}}_{\text{be}}^{\text{sym}}) / (8\pi\kappa) \quad (5.1)$$

between the bending energy  $\bar{\mathcal{E}}_{\text{be}}^{\text{asym}}$  of the asymmetric branch and the bending energy  $\bar{\mathcal{E}}_{\text{be}}^{\text{sym}}$  of the symmetric branch. Inspection of this inset

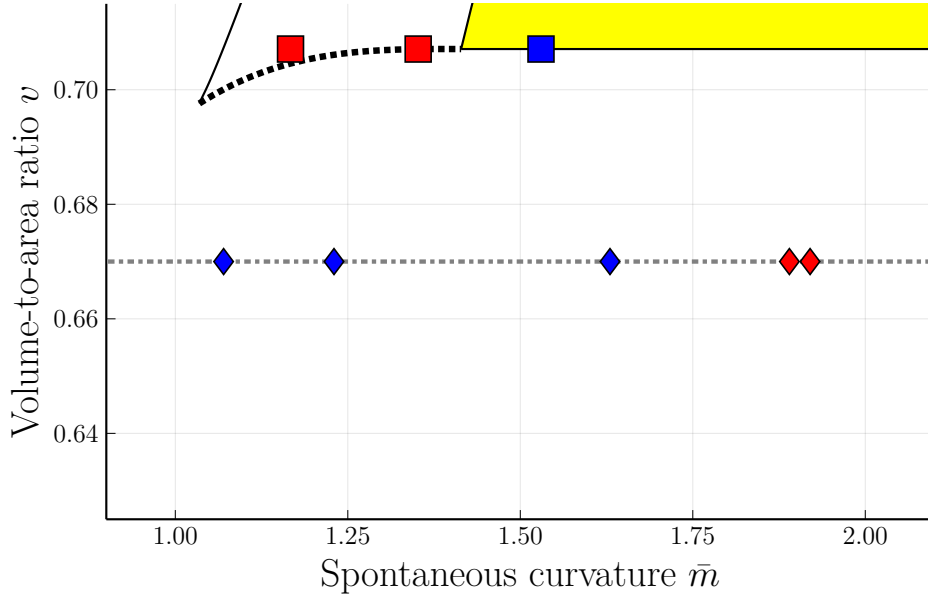


Figure 5.3. Close up of figure 4.6. The gray line at  $v = 0.670$  indicates the direction in which solutions were obtained. Starting at  $\bar{m} = 0$  the spontaneous curvature has been stepwise increased to find new solutions. The blue and red squares correspond to the solutions shown in figure 4.7. The blue and red diamonds correspond to the solutions shown in figure 5.3. Red markers indicate solutions on asymmetric branches and blue markers solutions on symmetric branches.

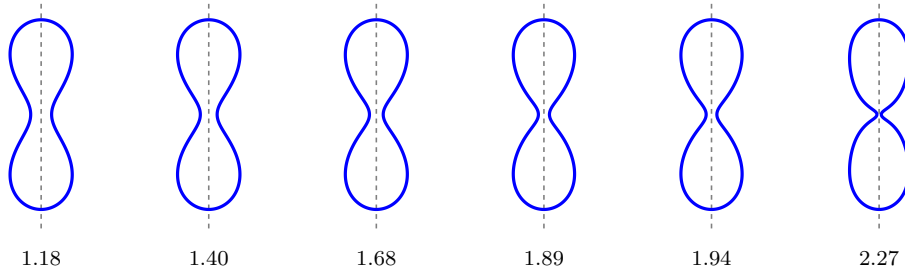


Figure 5.4: Symmetric dumbbell shapes (blue) for constant volume-to-area ratio  $v = 0.670$  and rescaled spontaneous curvature  $\bar{m}$  as given by the numerals below the shapes. The first three shapes correspond to the blue diamonds in figure 5.3. This sequence of shapes illustrates the closure of the membrane neck along the symmetric branch the value of the spontaneous curvature  $\bar{m}$  is increased from 1.18 to 2.27.<sup>[41]</sup>

reveals that the two energy branches merge with a common tangent for a critical  $\bar{m}$ -value close to 1.94. The latter behavior agrees with the shape evolution in figure 5.5, which directly demonstrates that the up-down asymmetric shapes become more and more symmetric as the bifurcation value  $\bar{m}(B_{\text{op}})$  of the spontaneous curvature is approached.

The bending energy difference  $\Delta\bar{\mathcal{E}}_{\text{be}}$  displayed in the inset of figure 5.6 is always positive, i.e., the asymmetric branch has an increased bending energy compared to the symmetric one. However, this energy increase is rather small for the whole range of  $\bar{m}$ -values covered by the shape oscillations. For  $\bar{m} = 1.89$ , for example, the bending energy of

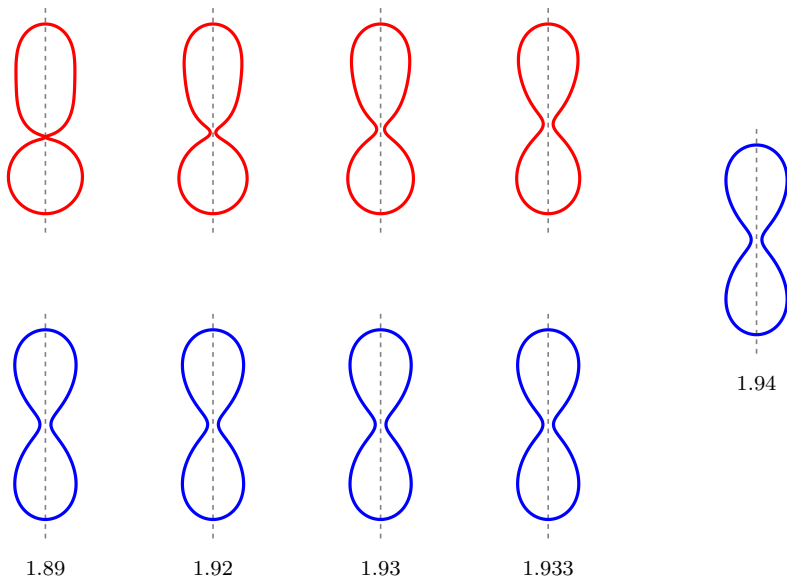


Figure 5.5: Up-down symmetric (blue) and asymmetric (red) dumbbells for  $v = 0.670$  and five values of the rescaled spontaneous curvature  $\bar{m}$  as indicated by the numerals below the shapes. The asymmetric dumbbells with  $\bar{m} = 1.89$  and  $1.93$  correspond to the red diamonds in figure 5.3. The two types of shapes coexist between  $\bar{m} = 1.89$  and  $\bar{m} = 1.933$ . For  $\bar{m} = 1.94$ , only the symmetric shape is found which implies that the asymmetric branch merges with the symmetric one at a critical value of the spontaneous curvature slightly above  $\bar{m} = 1.933$ . Comparison of the asymmetric and symmetric shapes reveals that the asymmetric shapes approach the symmetric ones in a continuous manner as we increase the spontaneous curvature towards its critical value. This conclusion is further corroborated by the corresponding energy branches in figure 5.6. Note that the neck radius of the asymmetric (red) dumbbells increases with increasing  $\bar{m}$ , in contrast to the behavior of the symmetric (blue) dumbbells.<sup>[41]</sup>

the asymmetric dumbbell is only  $0.002 \times 8\pi\kappa$  larger than the bending energy of the symmetric dumbbell. For the typical bending rigidity  $\kappa = 20k_{\text{B}}T$  at room temperature, the energy scale  $8\pi\kappa$  is  $503k_{\text{B}}T$  and the bending energy difference  $\Delta\bar{\mathcal{E}}_{\text{be}}$  is of the order of one  $k_{\text{B}}T$  for  $\bar{m} = 1.89$ .

For each dumbbell shape, the two subcompartments are connected by a membrane neck with a circular waistline. The radius of this waistline defines the neck radius  $R_{\text{ne}}$ , see figures 5.1 and 5.2, which changes during the shape oscillations.

In figure 5.7a, the rescaled neck radius  $\bar{R}_{\text{ne}}$  is displayed as a function of the spontaneous curvature  $\bar{m} = mR_{\text{ve}}$ , along the symmetric (blue) and asymmetric (red) branch of dumbbells. In addition to the two branches of the neck radius as a function of spontaneous curvature,

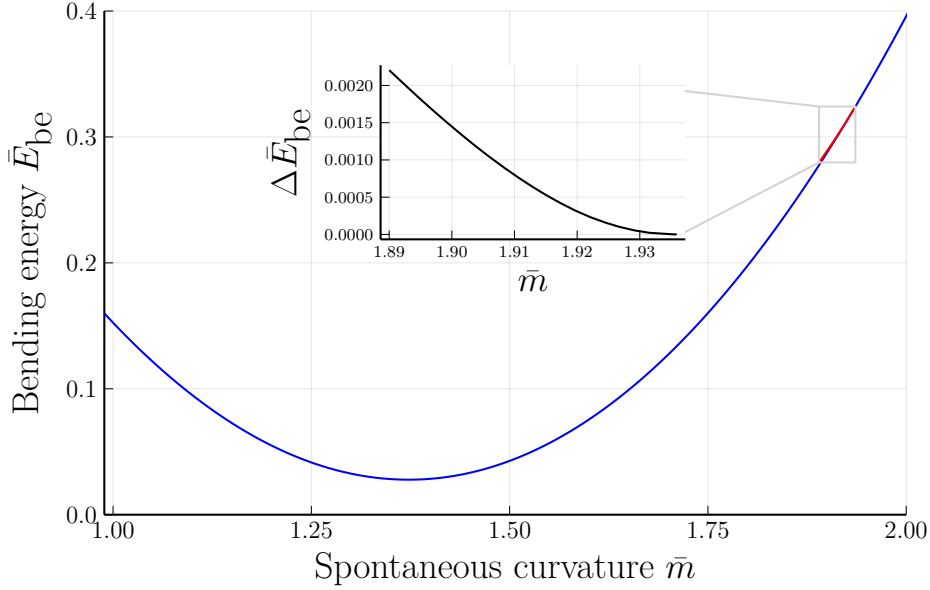


Figure 5.6: Rescaled bending energy  $\bar{\mathcal{E}}_{be} = \mathcal{E}_{be}/(8\pi\kappa)$  as a function of rescaled spontaneous curvature  $\bar{m}$  for volume-to-area ratio  $v = 0.670$ .  $\kappa$  is the bending rigidity. The  $\mathcal{E}_{be}$ -values are displayed in blue for the symmetric dumbbells and in red for the asymmetric ones. The inset shows the energy difference  $\Delta\bar{\mathcal{E}}_{be}$  between the asymmetric and the symmetric branch as defined in equation (5.1). The asymmetric branch (red) has a slightly larger bending energy than the symmetric branch (blue). In addition, the two branches merge with a common tangent at a critical  $\bar{m}$ -value slightly above  $\bar{m} = 1.933$ , see figure 5.5. The symmetric branch exhibits a pronounced minimum at  $\bar{m} = 1.373$  which reflects the vicinity of the corner point with  $v = 1/\sqrt{2}$  and  $\bar{m} = \sqrt{2}$ , see the morphology diagram in figure 5.3, at which the bending energy vanishes.<sup>[41]</sup>

the two panels b and c of figure 5.7 contain the numerical values of the neck radius  $\bar{R}_{ne}$  and the spontaneous curvature  $\bar{m}$  for the three dumbbell shapes in figures 5.1 and 5.2. The latter plots show once more that the neck radius decreases and increases monotonically along the symmetric and asymmetric branches, respectively, as the spontaneous curvature of the GUV membrane is increased. They also show how the uncertainties in the neck radius lead to different uncertainties in the spontaneous curvature, depending on the value of the radius as well as the branch to which the shape belongs. The steeper the curve of the neck radius is, the more accurate can the spontaneous curvature be estimated. Additionally the bifurcation point  $B_{op}$  and the optical limit are natural boundaries at which the error bars can be truncated.

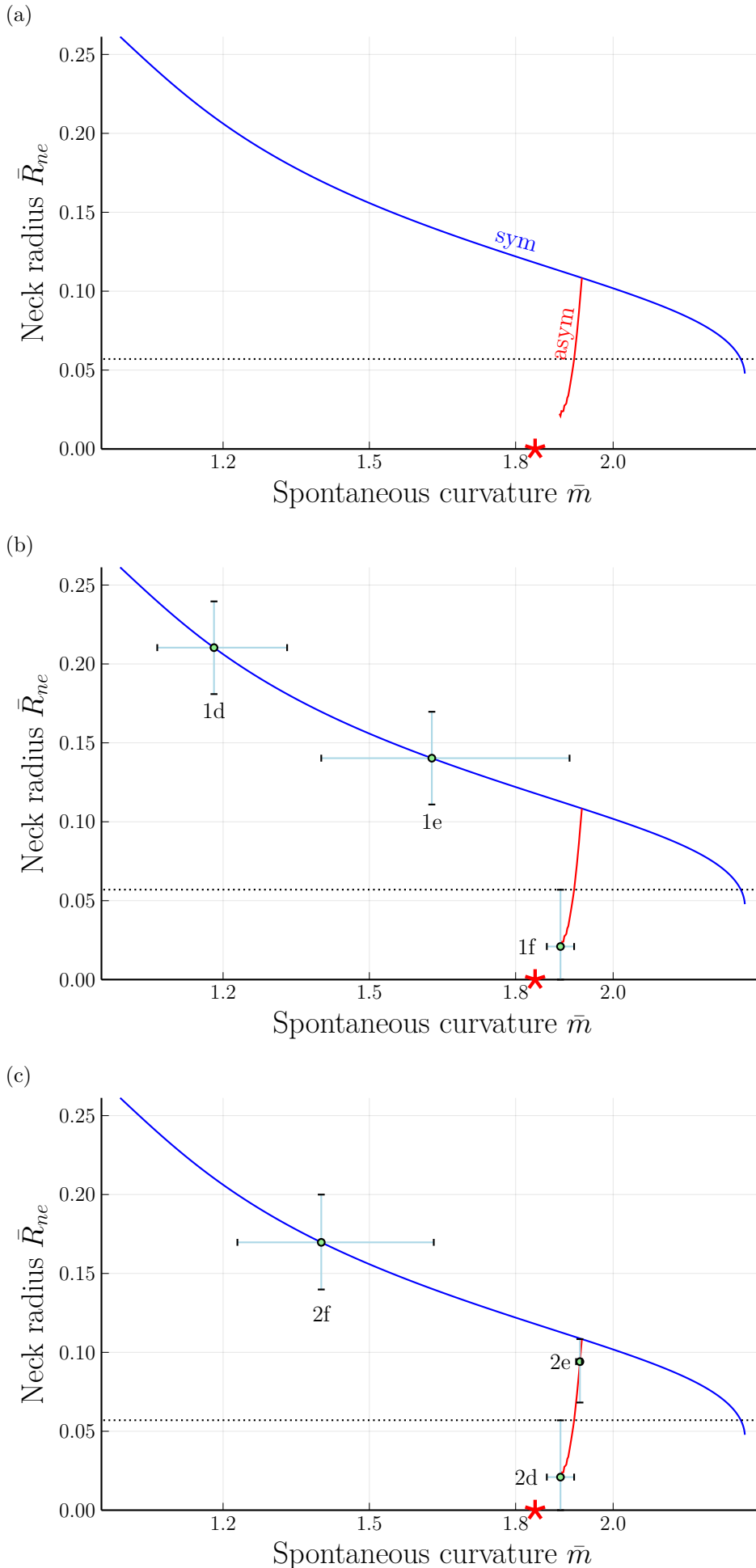


Figure 5.7. Rescaled radius  $\bar{R}_{ne} = R_{ne}/R_{ve}$  of membrane neck as a function of spontaneous curvature  $\bar{m}$  for  $v = 0.670$ : (a) Computed variation of the neck radius along the symmetric (blue) and asymmetric (red) dumb-bell branches. As the spontaneous curvature  $\bar{m}$  is increased, the neck radius decreases along the symmetric but increases along the asymmetric branch. The red star indicates the estimate  $\bar{m} \simeq 1.84$  for the spontaneous curvature of the prolate-sphere limit shape  $L_{ps}$  with  $\bar{R}_{ne} = 0$ ; (b) Evolution of neck radius and spontaneous curvature for the three shapes in figure 5.1 that describe the symmetry-breaking transformation; and (c) Evolution of neck radius and spontaneous curvature for the three shapes in figure 5.2 that describe the symmetry-restoring transformation. The error bars of the neck radius correspond to the uncertainty of the neck radius as obtained by approximating the experimental shape contours in figure 5.1a-c and figure 5.2a-c with splines, truncated at the bifurcation point and the threshold of the optical resolution. The error bars of the spontaneous curvature correspond to the resulting uncertainty of the spontaneous curvature given the non-linear shape of the curve. The horizontal dotted lines correspond to the optical resolution limit of 300 nm.<sup>[41]</sup>



#### 5.1.4 Finding shapes assuming $v = 0.685$

Table 5.1 shows that there is an interval of values for the reduced volume  $v$  that are compatible with the measurements. Choosing  $v = 0.685$  the shapes in figures 5.1a to 5.1c, 5.2a and 5.2c could also be matched as shown in figures 5.8 to 5.10, while there are no asymmetric solutions available for the range of values of the neck radius  $\bar{R}_{\text{ne}}$  measured for figure 5.2b as indicated by the orange bar in figure 5.10c. Hence, the assumption of  $v = 0.685$  is not in agreement with the experimental data. Finding rigorous bounds on the values of the volume-to-area ratio that are in agreement with the experiment remains an open task.

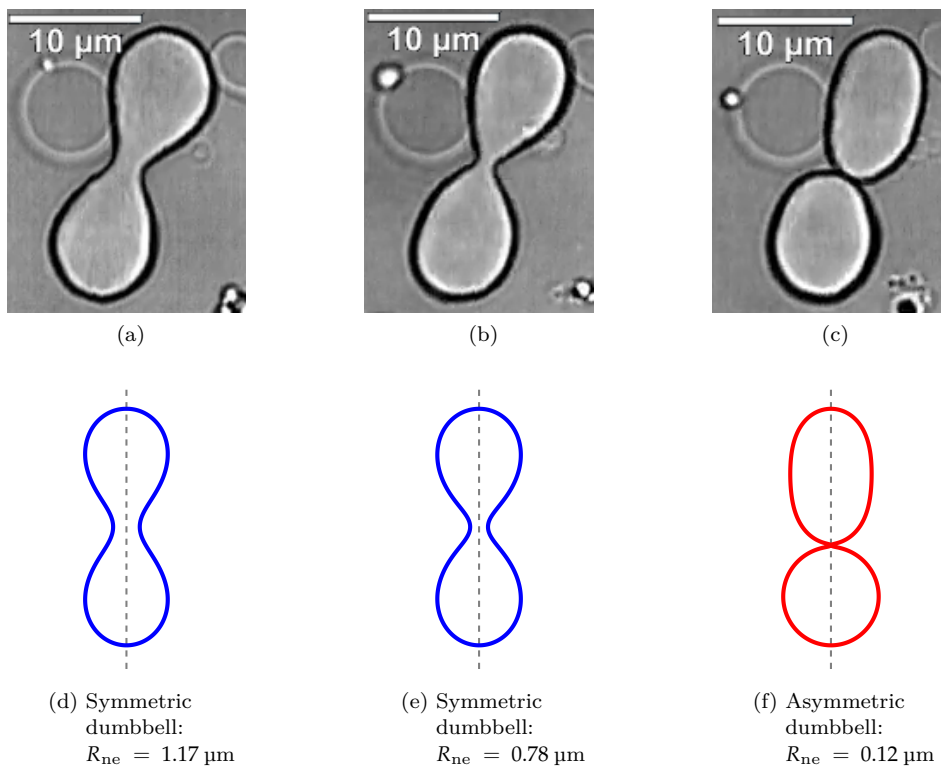


Figure 5.8. Same comparison as in figure 5.1 but the theoretical shapes (d), (e) and (f) are calculated assuming  $v = 0.685$ . These theoretical shapes are slightly less elongated and a bit wider as those in figure 5.1.

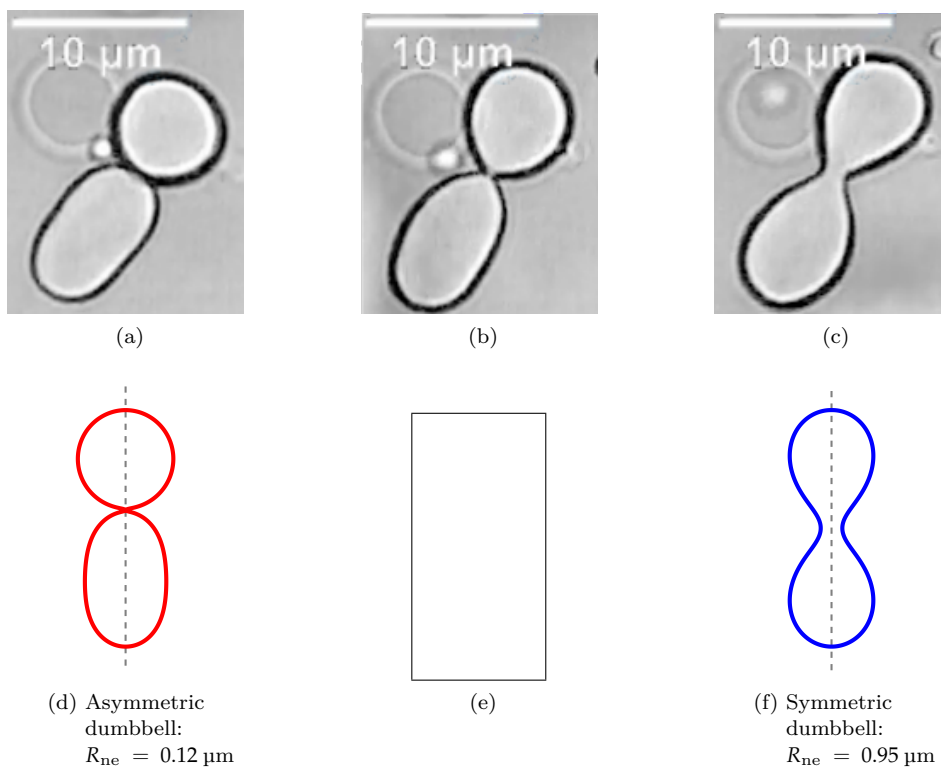


Figure 5.9. Same comparison as in figure 5.2 but the theoretical shapes (d) and (f) are calculated assuming  $v = 0.685$ . (e) For  $v = 0.685$  there is no asymmetric shape available that matches the measured neck of the shape in panel (c) as shown in figure 5.10.

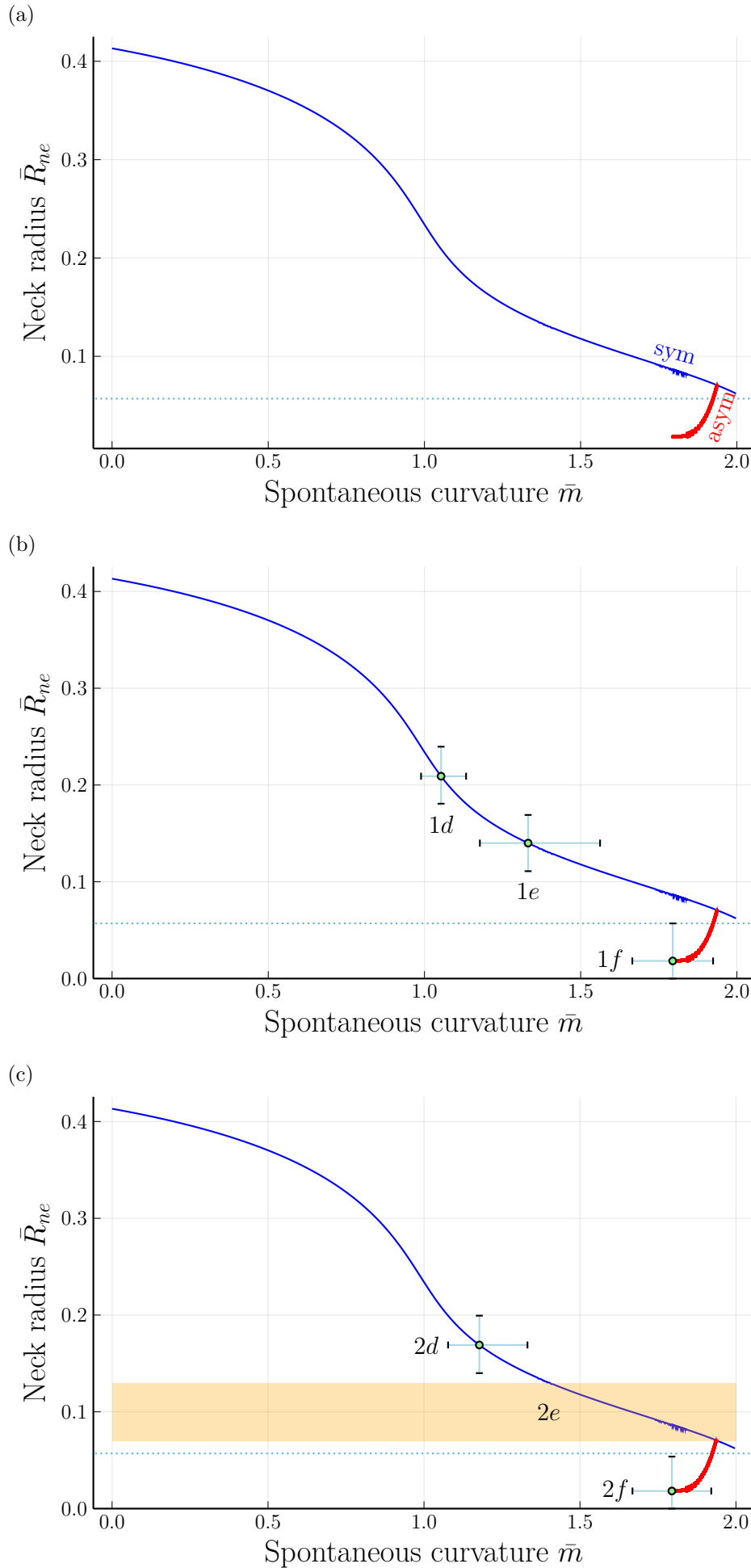




Figure 5.10. Rescaled radius  $\bar{R}_{ne} = R_{ne}/R_{ve}$  of membrane neck as a function of spontaneous curvature  $\bar{m}$  for  $v = 0.685$ : (a) Computed variation of the neck radius along the symmetric (blue) and asymmetric (red) dumb-bell branches. The qualitative behaviour of the neck radius as a function of the the spontaneous curvature  $\bar{m}$  is the same as in figure 5.7, but the region where both branches coexist is larger. (b) Evolution of neck radius and spontaneous curvature for the three shapes in figure 5.8 that describe the symmetry-breaking transformation; and (c) Evolution of neck radius and spontaneous curvature for the three shapes in figure 5.9 that describe the symmetry-restoring transformation. The orange band referring to figure 5.9e shows that there are no asymmetric solutions corresponding to the radii measured for figure 5.9b. This means that these data are not compatible with the choice of  $v = 0.685$ . It can be matched with lower  $v$  as shown in figure 5.7. The error bars of the spontaneous curvature correspond to the resulting uncertainty of the spontaneous curvature given the non-linear shape of the curve. The horizontal dotted lines correspond to the optical resolution limit of 300 nm.

### 5.1.5 Time evolution

The time-lapse Movie1  consists of 200 individual snapshots or frames which were taken with the predefined time interval  $\Delta t = 7.61$  s between successive frames. The frame number is identified by the index  $i$  from  $i = 1$  to  $i = 200$  and each frame is labeled as ‘open’ if it displays an open neck and as ‘closed’ if the neck appears to be closed on the optical image. In this way, the sequence of 200 vesicle images is mapped onto a sequence of open and closed states. Both types of states are persistent and form short subseries of successive open states that alternate with short subseries of successive closed states.

Neck closure events are provided by those frames that display a closed neck and are directly preceded by a frame with an open neck. Furthermore, a complete shape oscillation is defined by the sequence of  $\Delta i$  frames between two successive closure events. Such a sequence consists of a subseries of three to four successive images with closed necks, followed by a subseries of three to four successive images with open necks. Movie1  displays 191 frames between the first and the last closure event, which form 26 complete shape oscillations. Thus, the average number of frames,  $\langle \Delta i \rangle$ , per complete shape oscillation is equal to  $191/26 = 7.35$  frames and the average time period for one complete oscillation is given by  $\langle \Delta i \rangle \Delta t = 7.35 \times 7.61$  s = 55.9 s, which is similar to the cycle time observed for Min oscillations in other compartments<sup>[45,46]</sup>.

Most of the 26 complete shape oscillations consist of 7 or 8 successive images or frames. The 7-frame oscillations are observed 15 times, the 8-frame oscillations 10 times. In addition, one complete oscillation with only 6 successive frames is present. Thus, including these statistical fluctuations, the estimate  $\Delta i = \langle \Delta i \rangle \pm 1 = 7.35 \pm 1$  is obtained for the individual shape oscillations which shows that these oscillations are quite regular and almost clock-like. The small deviations from a perfect clock reflect the stochastic adsorption-desorption kinetics of

the Min proteins.<sup>[40,47]</sup> Furthermore, when these molecular oscillations drive the shape transformations of the GUVs, small differences in the initial shapes tend to become amplified during the shape evolution and to generate relative displacements of the two subcompartments around the membrane neck. To obtain a quantitative description of the experimentally observed shapes in terms of axisymmetric shapes, the images  $i = 1, 2$ , and 3 were selected for the symmetry-breaking transformation in figure 5.1 and the images  $i = 68, 69$ , and 70 for the symmetry-restoring transformation in figure 5.2.

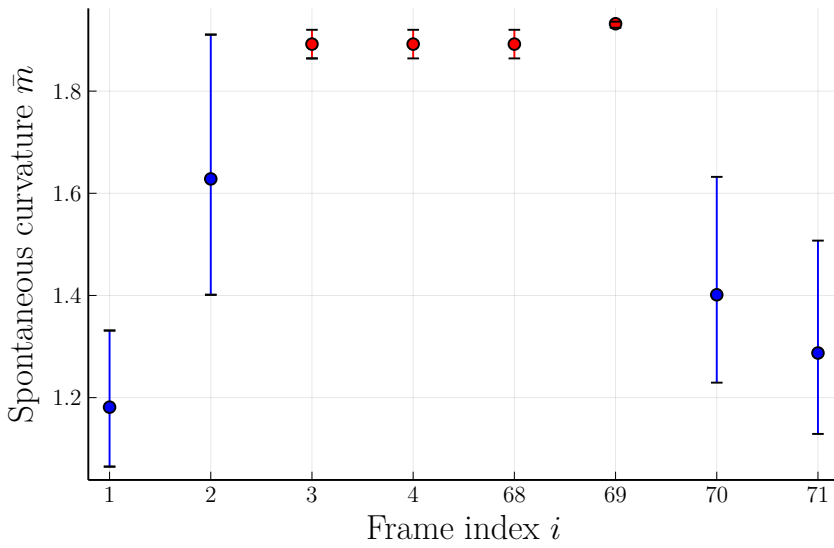


Figure 5.11: Rescaled spontaneous curvature  $\bar{m}$  versus frame index  $i$ . The frame  $i$  was taken at time  $t = (i - 1) \times 7.61$  s after the initial frame with index  $i = 1$ . The blue data points correspond to up-down symmetric dumbbell shapes, the red data points to asymmetric ones. The symmetry-breaking transformation in figure 5.1 corresponds to  $i = 1, 2$ , and 3, the symmetry-restoring transformation in figure 5.2 to  $i = 68, 69$ , and 70. The image  $i = 4$  displays a slightly distorted version of  $i = 3$  and is thus taken to have the same  $\bar{m}$ -value as  $i = 3$ . The image  $i = 71$  displays a symmetric dumbbell with an increased neck radius compared to  $i = 70$ . This increased radius implies the spontaneous curvature  $\bar{m} = 1.32$ . The combined sequence of all eight images represents one complete shape oscillation with an average time period of 55.9 s. The error bars are obtained as in figure 5.7.<sup>[41]</sup>

The theoretical shapes in figures 5.1 and 5.2 were obtained for the parameter values in table 5.2. The resulting time-dependence of the spontaneous curvature  $\bar{m}$  is shown in figure 5.11 where the spontaneous curvature  $\bar{m}$  is plotted versus the frame index  $i$  which corresponds to the time

$$t = (i - 1)\Delta t = (i - 1) \times 7.61 \text{ s} \quad (5.2)$$

after the initial image  $i = 1$ . For each spontaneous curvature  $\bar{m} = \bar{m}(i)$  in figure 5.11, the GUV shape has a certain neck radius  $\bar{R}_{\text{ne}} = \bar{R}_{\text{ne}}(\bar{m})$  as plotted in figure 5.7b and c. When these two relationships are combined, the time dependence of the neck radius  $\bar{R}_{\text{ne}} = \bar{R}_{\text{ne}}(i)$  as shown in figure 5.12 is obtained.

Because of the relatively large error bars for the data in figure 5.12, depicting the time-dependence of the neck radius  $\bar{R}_{\text{ne}}$ , it is difficult to fit these data in a quantitative manner. The presumably simplest fit is provided by a single Fourier mode of the form

$$\bar{R}_{\text{ne}} = a + b \cos[2\pi(i - 1)/7], \quad (5.3)$$

where the frame indices  $i = 68, \dots, 71$ <sup>2</sup> in figure 5.12 are identified with the indices  $i = 5, \dots, 8$  as well as the frame indices  $i = 8$  and  $i = 1$ , thereby taking the oscillation period to be  $\Delta i = 7$ . Using the method of least squares provided by LsqFit.jl<sup>[48]</sup>, the parameter values  $a = 0.10 \pm 0.02$  and  $b = 0.09 \pm 0.03$  are retrieved as used in figure 5.12.<sup>[41]</sup>

<sup>2</sup> As a reminder: these frames were taken instead of the succeeding frames  $i = 5, \dots, 8$  because the vesicle is less tilted around its neck in those frames. They correspond to the same phase of the oscillation, just shifted by 9 periods.

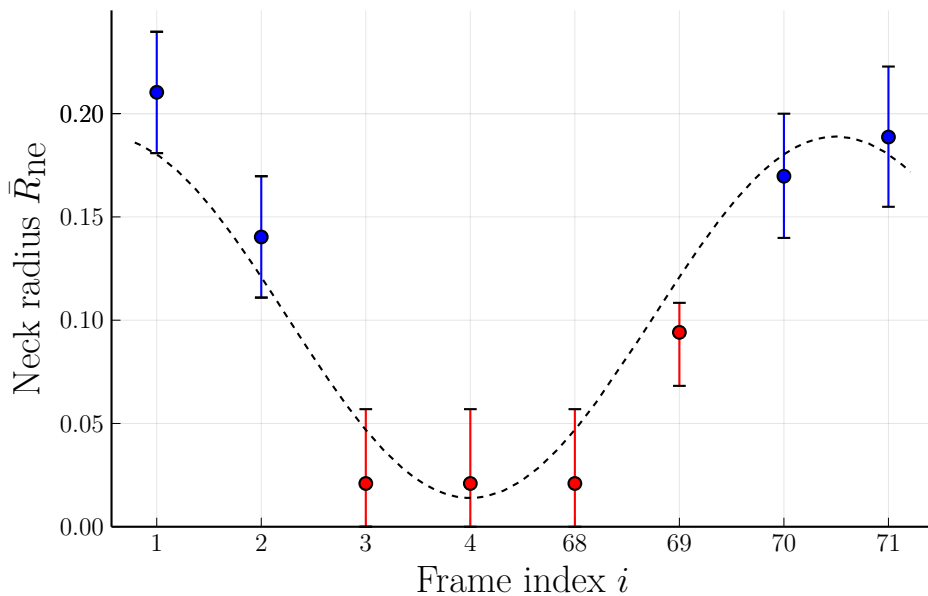


Figure 5.12. Rescaled neck radius  $\bar{R}_{\text{ne}}$  versus frame index  $i$  corresponding to time  $t = (i - 1) \times 7.61$  s. Direct inspection of the frame with index  $i = 71$  leads to the neck radius  $\bar{R}_{\text{ne}} = 0.189$  for this image. The combined sequence of all eight images represents one complete shape oscillation which takes, on average, 55.9 s. The color code of the data points is the same as in figure 5.11. The trigonometric curve (dashed black line) through the data provides the best fit to a single Fourier mode as parametrized by equation (5.3). The error bars are obtained as in figure 5.7.<sup>[41]</sup>

## 6 Concentration gradients in rigid compartments

The previous chapters mostly showed possible shape transformations in the case of homogeneously filled vesicles. By itself homogeneous vesicles are quite a complex system and thus when adding another complexity in form of concentration gradients, it is instructive to reduce the complexity of the compartment by substitution of the flexible vesicle with a rigid compartment. In particular rigid cone-like compartments and their interaction with an ideal gas in a gravitational field or a solution of processive molecular motors are studied. An outlook of how to deal with gradients in vesicles can be seen in appendix A.

### 6.1 Ideal gas in cones

The simplest case is a conic compartment as introduced in section 3.2 filled with an ideal gas in a gravitational field as depicted in figure 6.1.

How to calculate the free energy  $F$  for this system was covered in section 3.2 when combining equation (2.8) with example 2.4. For the sake of comparability the same energy scale as for the bending energy in chapters 4 and 5 is chosen

$$\bar{F} = \frac{F}{8\pi\kappa}. \quad (6.1)$$

The gas will have a different free energy depending on the opening angle  $\alpha$  of the cone, given that the rotation axis of the cone is aligned with the vector of the gravitational field. The free energy of the gas

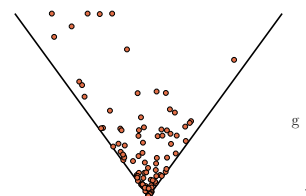


Figure 6.1. Schematic of ideal gas particles confined in a conic compartment in the gravitational field of the earth.

has been calculated in section 2.2.1 and reads

$$\bar{F} = -\frac{N}{8\pi\kappa\beta} \log(Z_1(L, R, \alpha)) , \tag{6.2}$$

where  $Z_1(L, R, \alpha)$  is the same as in example 2.4. Figure 6.2 shows that the free energy of the gas is lower the wider the base of the cone is and a small influence when forming sharp kinks as the minimal/maximal opening angle  $\alpha_c$  is approached. This leads to an optimal opening angle that is below the maximum opening angle.

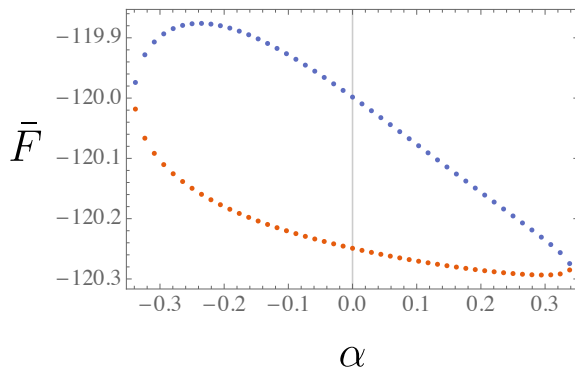


Figure 6.2. Free energy of an ideal gas subject to gravity as given by equation (6.2) with  $\beta = 0.25 \cdot 10^{21} \frac{1}{J}$ ,  $M = 5 \cdot 10^{-26} \text{kg}$  and  $N = 600$  in conic compartment with  $V = 1 \text{pl}$ ,  $v = 0.8$ ,  $\kappa = 8 \cdot 10^{-21} \text{J}$  and  $m = 0$ . Curves of different color correspond to the two different solutions of equations (3.23) and (3.24).

*Total Energy*

The total energy  $\bar{\mathcal{E}}_{\text{tot}} = \bar{\mathcal{E}}_{\text{be}} + \bar{F}$  can have a different minimum of energy when the particle density is low enough to not compensate the cost of increasing the bending energy as shown in figure 6.3. The bending energy of this system was derived in equation (3.35) and the free energy is given by equation (6.2).

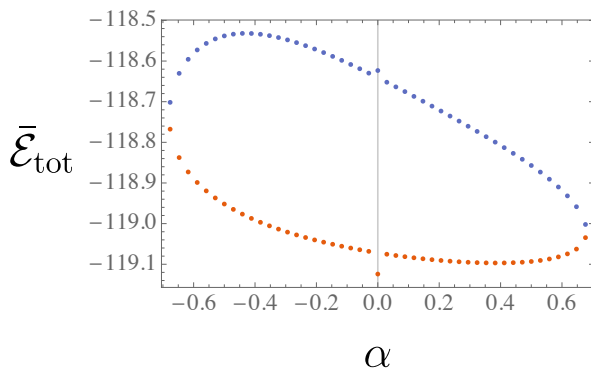


Figure 6.3. Total energy of an ideal gas subject to gravity with  $\beta = 0.25 \cdot 10^{21} \frac{1}{J}$ ,  $M = 5 \cdot 10^{-26} \text{kg}$  and  $N = 600$  in conic compartment with  $V = 1 \text{pl}$ ,  $v = 0.8$ , and  $m = 0$ . Curves of different color correspond to the two different solutions of equations (3.23) and (3.24). In contrast to figure 6.2 the tube is now the preferred shape. If the number of particles would be increased, the graph will gradually start to look more like figure 6.2.



### Conclusions

This short detour illustrates the counter play between the strive of the ideal gas to maximize the volume in the direction of the gradient and the bending energy which penalizes highly curved regions. This can lead to the counter-intuitive result of an optimal opening angle below the critical angle  $\alpha_c$  if only the free energy of the gas is considered. If the bending energy is included and the magnitude of the energies is comparable, the tube remarkably robust.

### 6.2 Cytoskeletal molecular motors

The rest of this chapter is about molecular motors in rigid compartments. Therefore a short introduction about the biological function of the type of molecular motors that are considered in this thesis follows.

The cytoskeleton has a major influence on the shape of the cell. It can have three types of filaments: microtubuli, actin filaments and intermediate filaments. Besides being a main component for the mechanical properties of the cell they also serve as tracks or anchors for molecular motors and play a role in the inner dynamics of the cell.

Molecular motors have at least two parts: one part which can bind to and unbind from cytoskeletal filaments and another part which can bind to cargo or loads. Furthermore, the amount of steps that motors typically perform before detaching does vary and motors that perform many steps are called *processive* molecular motors (e.g. kinesin and dynein), while those that detach after only a few conformation changes are non-processive motors (e.g. myosin II).

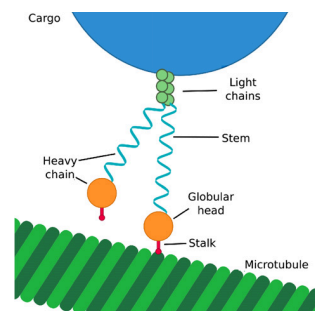


Figure 6.4. Structure of a processive molecular motor. The motor is attached to the microtubulus via its two head proteins. The heads are then connected via two different chains to the cargo. Typically multiple motors are attached to one cargo.<sup>[49]</sup>

Processive motors walk along polar filaments usually in a preferred direction but in a stochastic fashion, that is they occasionally step backwards or sideways<sup>[50]</sup>. They use energy gained by hydrolysis of adenosine triphosphate (ATP) to perform various kinds of motion. Kinesin for example walks in a hand-over-hand fashion (cf. figure 6.5)<sup>[51]</sup>.

They can transport organelles, vesicles<sup>[52]</sup>, filament precursors, mRNA granules<sup>[53]</sup>, lipid droplets<sup>[54]</sup>, viral capsids<sup>[55]</sup>, lysosomes, or even objects as large as mitochondria<sup>[56]</sup>. Thus they play an important role in intracellular transport.

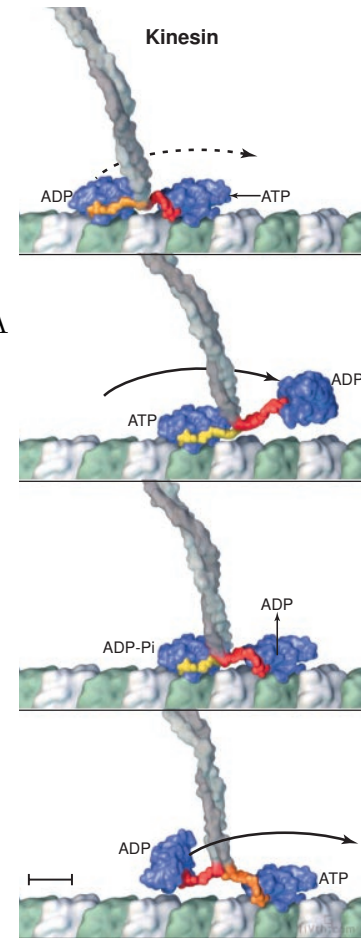


Figure 6.5. The two heads of kinesin move in a coordinated hand-over-hand fashion. By binding ATP to the leading head the conformation change of the linker protein (red/ orange) is induced, which flips the rear head over the front head. Then hydrolyzation of the ATP produces ADP and inorganic phosphate. Meanwhile the new leading head binds tightly to the filament site. From this configuration the process can be repeated as long as ATP supply is sufficient.<sup>[51]</sup>

### 6.3 Molecular motors in tubes

Creating gradients in vesicles by gravitation might be difficult because the effect of gravitation is relatively small compared to hydrodynamic forces and diffusion effects. Nonetheless it was instructive to inspect this system since the qualitative effects should be the same as in other systems with gradients.

Another way to create gradients in vesicles is via an active process like processive molecular motors (cf. figure 6.4). This has the drawback that the free energy  $F$  of the system can't be calculated by equilibrium thermodynamics. Instead the density of the particles themselves have to be considered.

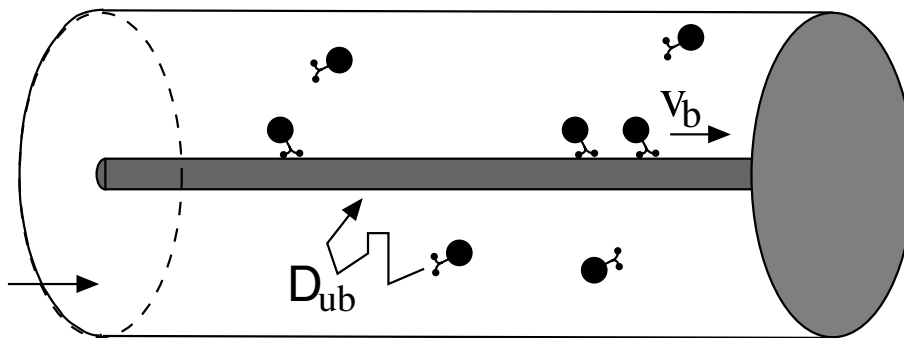


Figure 6.6. Model system of molecular motors in a half-open tube with a microtubule along the axis of rotation. Motors diffuse in the bulk and perform a biased random walk along the microtubule.<sup>[57]</sup>

As mentioned in section 6.2 motors can bind to microtubuli and perform stochastic directed motion by hydrolyzation of ATP.

A model system studied by Müller *et al.*<sup>[57]</sup> is a half-open tube of length  $L$ , radius  $R$  and cross-section  $\sigma_{\text{cyl}}$  with one microtubulus along the axis of rotation (cf. figure 6.6). Such a half-open compartment can be viewed as a part of a larger compartment, such as the end of an axon. Molecular motors travel along the tubulus in their preferred direction with the effective velocity  $v_b$ , detach, diffuse undirected in the cytosol with the diffusion rate  $D_{\text{ub}}$  and reattach. This leads eventually to a higher concentration of molecular motors in the region towards which the motors are preferably moving. If the motor density  $\rho_b$  of

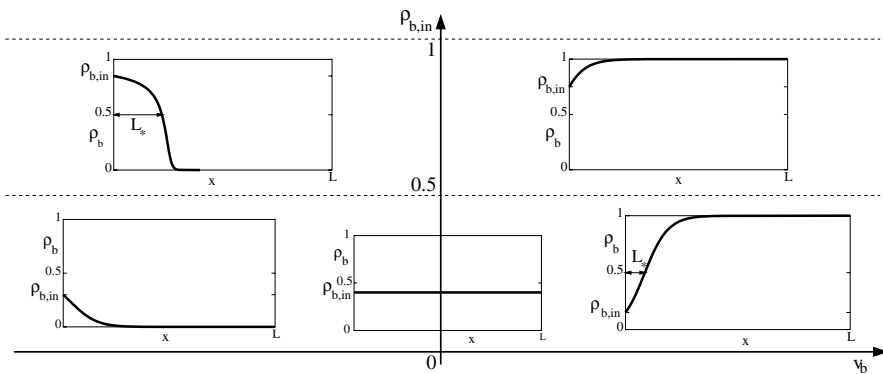


Figure 6.7. Possible density profiles along the axis of rotation for a half-open tube. Depending on the direction of movement along the microtubuli (positive or negative velocity of bound motors  $v_b$ ) and initial concentration of bound motors  $\rho_{b, \text{in}}$  the tube gets either crowded or drained. If the motor don't have undirected motion on the filament the density is homogenous.  $L_*$  is called the jam length.<sup>[57]</sup>

the motors that are bound to the microtubulus is considered, three different states can be observed: When the motors are moving towards the closed end of the tube (positive  $v_b$ ) the density increases towards the closed end and the microtubulus gets crowded. While when the net velocity is zero the bound motor density will be match the initial density in equilibrium. Finally, if the motors effectively move towards the open end, the motor density will only reach a finite amount that is less than the tube length into the tube (cf. figure 6.7). In both cases of velocities different from zero the distance until which the bound motor density reaches 0.5 is referred to as the jam length  $L_*$ <sup>[57]</sup>, which is a measure of the location of the concentration gradient.

It was shown that the jam length depends on two relative characteristics connected to the two possible kinds of motion, the desorption constant  $K$  is the ratio of the unbinding rate  $\gamma_{\text{ub}}$  to the binding rate  $\gamma_b$

$$K = \frac{\gamma_{\text{ub}}}{\gamma_b} \quad (6.3)$$

whereas the ratio of the times that are needed to travel the distance  $L$  in the bounded or unbounded state respectively is denoted by  $\mu$

$$\mu = \frac{L v_b}{\sigma_{\text{cyl}} D_{\text{ub}}}. \quad (6.4)$$

Furthermore, with these the jam length was found to be determined by<sup>[57]</sup>

$$g(\rho, K) = \frac{-1}{\frac{1}{1-K} - \rho} + K \ln(\rho) - \frac{1}{K} \ln(1 - \rho) + \frac{1 - K^2}{K} \ln \left| \frac{1}{1 - K} - \rho \right| \quad (6.5)$$

$$\frac{L_*}{L} = \frac{1}{\mu} \left[ g \left( \frac{1}{2}, K \right) - g(\rho_{b, in}, K) \right]. \quad (6.6)$$

Which simplifies in the special case of  $K = 1$  to

$$\frac{L_*}{L} = \frac{1}{\mu} \ln \left( \frac{1 - \rho_{b, in}}{\rho_{b, in}} \right). \quad (6.7)$$

#### 6.4 Density of molecular motors in conic compartments

In this section the result of section 6.3 is generalized to geometries of cones and numerical particle simulations are used to verify the results. In the two-state approximation<sup>[57]</sup> the unbound motor density is integrated over the dimensions perpendicular to the filament. Motors bind to the filament with binding rate  $\gamma_b$  and unbind with rate  $\gamma_{ub}$ , resp. with binding probability  $p_b$  and unbinding probability  $p_{ub}$ . On the filament they perform a biased random walk with forward rate  $\gamma_+$  ( $p_+$ ) and backward rate  $\gamma_-$  ( $p_-$ ) and in the bulk they perform an undirected random walk. The mean diffusion time of the un-/bound motors is denoted by  $\tau/\tau_b$ .

Using mean-field theory, the equations for the stationary density profiles of bound motors  $\rho_b$  and unbound motors  $\rho_{ub}$  are given by the equation for zero net current

$$0 = v_b \rho_b (1 - \rho_b) - \sigma(z) D_{ub} \frac{\partial}{\partial z} \rho_{ub} \quad (6.8)$$

$$v_b = \frac{L(p_+ - p_-)}{\tau_b},$$

where  $v_b$  is the effective velocity of the bound motors and the balance of currents at any filament site

$$\frac{\partial}{\partial z} [v_b \rho_b (1 - \rho_b)] = v_b (1 - 2\rho_b) \frac{\partial}{\partial z} \rho_b = \gamma_b \rho_{ub} (1 - \rho_b) - \gamma_{ub} \rho_b (1 - \rho_{ub}). \quad (6.9)$$

If the probability of an unbinding event at any filament site is equal to an binding event it is called adsorption equilibrium. In terms of the motor densities it reads

$$\gamma_b \rho_{ub} (1 - \rho_b) = \gamma_{ub} \rho_b (1 - \rho_{ub}). \quad (6.10)$$

Using this assumption, the mean-field equation for the bound and unbound motor density becomes

$$\frac{\partial}{\partial z} \rho_b(z) = \mu(z) \frac{(1-K)^2}{K} \rho_b(1-\rho_b) \left( \frac{1}{1-K} - \rho_b \right)^2 \quad (6.11)$$

$$\frac{\partial}{\partial z} \rho_{ub} = \mu(z) \frac{K \rho_{ub}(1-\rho_{ub})}{(\rho_{ub} + K(1-\rho_{ub}))^2}. \quad (6.12)$$

Since the radius  $r(z)$  is now a function of  $z$ , so is the cross-section  $\sigma(z)$  and the relative motility  $\mu(z)$

$$\sigma(z) \cong \pi r(z)^2 \quad (6.13)$$

$$\mu(z) = \frac{L(p_+ - p_-)}{\tau_b \sigma(z) D_{ub}}. \quad (6.14)$$

Equation (6.9) leads to the conclusion that adsorption equilibrium strictly holds in regions where  $\rho_b = \frac{1}{2}$  and where the spatial derivative of the bound motors vanishes and in the trivial case where the effective movement along the microtubulus is zero.

In a closed cone the particle conservation requires

$$N = \int_0^L \rho_b(z) + \sigma(z) \rho_{ub}(z) dz. \quad (6.15)$$

#### 6.4.1 Motor densities for $K = 1$

If the desorption constant is  $K = 1$  both equations (6.11) and (6.12) become

$$\frac{\partial}{\partial z} \rho(z) = \mu(z) \rho(1-\rho). \quad (6.16)$$

Equation (6.16) can be solved by integration by parts

$$\frac{\partial \rho}{\rho(1-\rho)} = \partial z \mu(z) \quad (6.17)$$

$$(\log(\rho) - \log((1-\rho))) = \int \mu(z') dz' + c \quad (6.18)$$

$$\frac{\rho}{1-\rho} = e^{\frac{1}{c} \int_0^z \frac{1}{r(z')^2} dz' + c} \quad (6.19)$$

Finally, with  $\rho(0) = \rho_0$

$$\rho(z) = \frac{1}{1 + \frac{1-\rho_0}{\rho_0} e^{-\frac{1}{L} \int_0^z \mu(z') dz'}}. \quad (6.20)$$

The only thing that is left, is the calculation of the integral in the exponent of equation (6.20)

$$\begin{aligned} \frac{1}{L} \int_0^z \mu(z') dz' &= \frac{(p_+ - p_-) L}{\tau_b \pi D_{ub}} \int_0^z \frac{1}{r^2(z')} dz' = \\ \frac{L}{C} \int_0^z \frac{1}{r^2(z')} dz' &= \frac{L}{C} \frac{z}{\left(R + \frac{L}{2} \tan \alpha\right) \left(R + \left(\frac{L}{2} - z\right) \tan \alpha\right)}, \end{aligned} \quad (6.21)$$

where  $C = \frac{\tau_b \pi D_{ub}}{(p_+ - p_-)}$ .

For open compartments  $\rho_0$  is a given parameter, whereas for closed compartments  $\rho_0$  has to be calculated from equation (6.15).

#### 6.4.2 Jam length in open conic compartments

*Analytic results for  $K = 1$ :*

Using the definition of the jam-length  $\rho(L_*) = 1/2$  in equation (6.20) yields

$$\frac{L}{C} \int_0^{L_*} \frac{1}{r^2(z)} dz = -\log \left( \frac{\rho_0}{1 - \rho_0} \right),^1 \quad (6.22)$$

where  $C = \frac{\tau_b \pi D_{ub}}{(p_+ - p_-)}$ .

<sup>1</sup> Another measure that can be interesting is the decay length  $L_*$  defined by  $\rho(L_*) = \frac{\rho_0}{2}$ . This would yield  $\log \left( \frac{2-\rho_0}{1-\rho_0} \right)$ .

#### 6.4.3 Variation of opening angle with constant length and radius

This kind of transformation is aimed to mimic the behaviour when part of a tubular cell gets squeezed at the closed end.  $R$  refers to the radius at the open left end of the compartment in this section. Also there is no conservation of either volume or area, instead the radius  $R$  and length  $L$  are kept constant. Two cases are considered:

*Global deformation:* Squeezing at the tip in a manner that the shape of the whole compartment is affected is the first case. The opening



angle varies from zero to the critical angle  $\alpha \in [0, \alpha_c]$  (cf. figure 6.8).

In this setup the critical angle is given by

$$\alpha_c = \arctan\left(\frac{R}{L}\right). \quad (6.23)$$

$$r(z) = R - z \tan(\alpha) \quad (6.24)$$

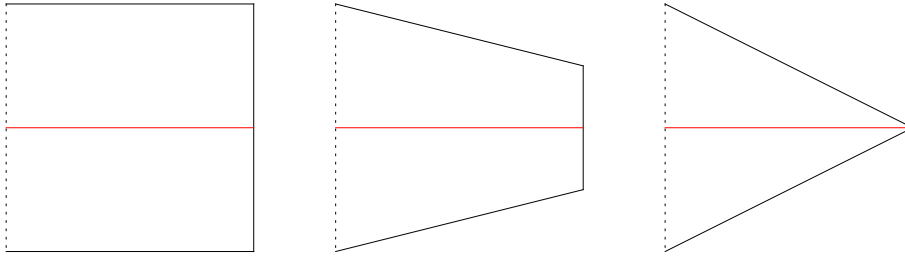


Figure 6.8. Cross section of parametric variation of the boundaries. Solid black lines are hard walls and dotted lines are open boundaries. The red line represents the microtubulus.

*Local deformation:* The other case is when the compartment only locally deforms. Thereby opening angles  $\alpha \in [\alpha_c, \pi/2]$  can be achieved (cf. figure 6.9).

$$r(z) = \begin{cases} R & z \leq L - R/\tan(\alpha) \\ (L - z) \tan(\alpha) & z \geq L - R/\tan(\alpha) \end{cases} \quad (6.25)$$

At  $\alpha = \alpha_c$  both methods coincide.

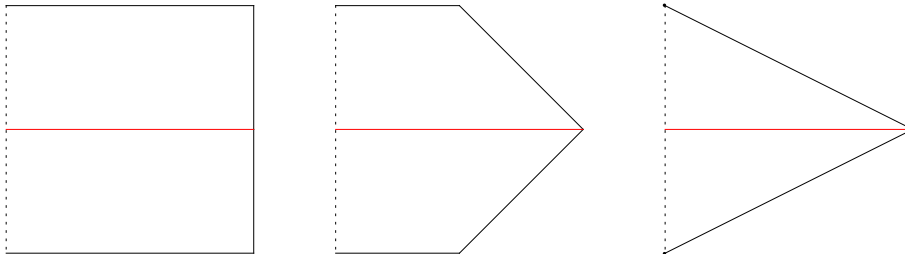


Figure 6.9. Cross section of parametric variation of the boundaries. Solid black lines are hard walls and dotted lines are open boundaries. The red line represents the microtubulus.

There are three regions at which equation (6.22) has to be evaluated:

1.  $\alpha \in [0, \alpha_c]$ ,
2.  $\alpha \in [\alpha_c, \alpha_{23}]$ ,
3.  $\alpha \in [\alpha_{23}, \pi/2]$ .

To this point  $\alpha_{23}$  is unknown, since it depends on the location of the gradient measured by  $L_*$ . The integral on the left hand side of equation (6.22) is calculated for the three cases in the upcoming paragraphs.

1.  $r(z) = R - z \tan(\alpha)$

$$\begin{aligned} \int_0^{L_*} \frac{1}{r^2(z)} dz &= \int_0^{L_*} \frac{1}{(R - z \tan(\alpha))^2} dz \\ &= \left. \frac{1}{\tan(\alpha) (R - z \tan(\alpha))} \right|_0^{L_*} \\ &= \frac{L_*}{R^2 - RL_* \tan(\alpha)} \end{aligned} \quad (6.26)$$

Inserting equation (6.26) into equation (6.22) results in

$$\frac{L_*}{L} = \frac{R^2}{RL \tan(\alpha) + L^2 \left[ C \log \left( \frac{\rho_0}{1-\rho_0} \right) \right]^{-1}}. \quad (6.27)$$

2.  $r(z)$  given by equation (6.25) and  $L_* \geq L - R/\tan(\alpha)$

$$\begin{aligned} \int_0^{L_*} \frac{1}{r^2(z)} dz &= \int_0^{L-R/\tan(\alpha)} \frac{1}{R^2} dz + \int_{L-R/\tan(\alpha)}^{L_*} \frac{1}{((L-z) \tan(\alpha))^2} dz \\ &= \frac{\cot^2(\alpha)}{L - L_*} + \frac{L}{R^2} - \frac{2 \cot(\alpha)}{R} \end{aligned} \quad (6.28)$$

Inserting equation (6.28) into equation (6.22) results in

$$\frac{L_*}{L} = 1 - \frac{R^2 \cot^2(\alpha)}{CR^2 \log \left( \frac{\rho_0}{1-\rho_0} \right) - L^2 + 2RL \cot(\alpha)} \quad (6.29)$$

3.  $r$  given by equation (6.25) and  $L_* \leq L - R/\tan(\alpha)$

$$\begin{aligned} \int_0^{L_*} \frac{1}{r^2(z)} dz &= \frac{L_*}{R^2} \\ \Rightarrow \frac{L_*}{L} &= \frac{CR^2}{L^2} \log\left(\frac{\rho_0}{1-\rho_0}\right) \end{aligned} \quad (6.30)$$

Now  $\alpha_{23}$  can be calculated by the point where equations (6.29) and (6.30) coincide.

$$\begin{aligned} \frac{CR^2}{L^2} \log\left(\frac{\rho_0}{1-\rho_0}\right) &= 1 - \frac{R^2 \cot^2(\alpha)}{CR^2 \log\left(\frac{\rho_0}{1-\rho_0}\right) - L^2 + 2RL \cot(\alpha)} \\ \Rightarrow \alpha_{23} &= \cot^{-1}\left(\frac{L^2 - CR^2 \log\left(\frac{\rho_0}{1-\rho_0}\right)}{RL}\right) \end{aligned} \quad (6.31)$$

From equation (6.31) follows also that

$$0 < R < \sqrt{\frac{L^2}{C \log\left(\frac{\rho_0}{1-\rho_0}\right)}} \quad (6.32)$$

to ensure a physically meaningful solution.

The relative reduction of  $L_*$  is given by

$$\begin{aligned} \Delta L_* &= 1 - \frac{L_*(\alpha = \alpha_c)}{L_*(\alpha = 0)} \\ &= \frac{1}{1 + \frac{L^2}{CR^2 \log\left(\frac{\rho_0}{1-\rho_0}\right)}}. \end{aligned} \quad (6.33)$$

*Verification:*

Numerical solution of equation (6.11) is used to compare it to the analytical curves of equation (6.27)-equation (6.30) [\(🔗\)](#). Figure 6.10 shows the corresponding curves. It is visible that the curves match the simulation all regions.

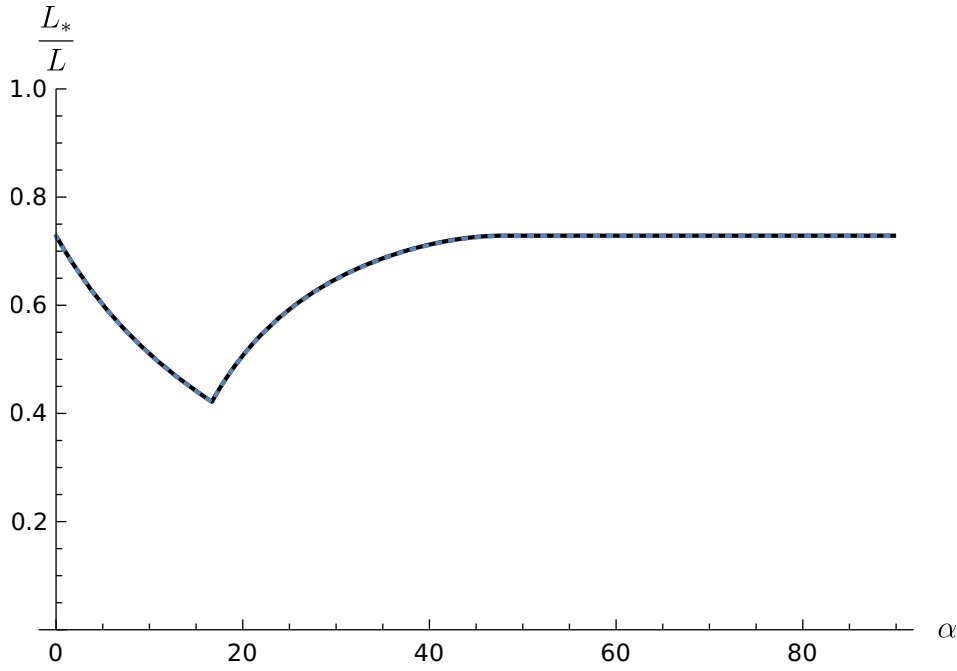


Figure 6.10. Comparison of numeric (solid black line) and analytic (dashed blue line) results for the jam length vs. the opening angle. The agreement is very good in all three regions. Parameters are:  $R = 30$ ,  $L = 100$ ,  $p_+ = 0.1$ ,  $p_- = 0.8$ ,  $p_b = 0.8$  and  $p_{ub} = 0.01$ .

*Results for  $K \neq 1$ :*

Integration of equation (6.11) yields a cumbersome transcendental equation for  $\rho(z)$ , which will not be displayed here. However, this equation has not to be resolved for calculation of the jam length. All calculations are analogue to the case of  $K = 1$  and the general results can be obtained by the following substitutions:

$$C \log \left( \frac{1 - \rho_0}{\rho_0} \right) \rightarrow C K \left( \frac{(1 - K)^2}{K} \frac{2\rho_0}{1 + K - (1 - K^2)\rho_0} + \log \left[ \frac{1 - (1 - K)\rho_0}{\rho_0} \left( \frac{1 - \rho_0}{1 - (1 - K)\rho_0} \right)^{\frac{1}{K^2}} (1 + K^2)^{\frac{K^2 - 1}{K^2}} \right] \right) \quad (6.34)$$

resp. if  $L_*$  is considered

$$C \log \left( \frac{1 - \rho_0}{2 - \rho_0} \right) \rightarrow C K \left( \frac{(1 - K)^2 \rho_0}{K(1 - (1 - K)\rho_0)(2 - (1 - K)\rho_0)} + \log \left[ \frac{1 - (1 - K)\rho_0}{2 - (1 - K)\rho_0} \left( \frac{(1 - \rho_0)(2 - (1 - K)\rho_0)}{(2 - \rho_0)(1 - (1 - K)\rho_0)} \right)^{\frac{1}{K^2}} \right] \right) \quad (6.35)$$

## 6.4.4 Simulation

Finally the results can be compared to the average particle densities obtained from a stochastic particle simulation (cf. appendix C). This simulation is performed by discretizing the space in a three-dimensional regular lattice with lattice constant  $a = 8\text{nm}$ , which corresponds to the step-length of kinesin motors. The molecular motors are modeled by hard core particles diffusing on a 3D-grid, with one central filament along the  $z$ -axis, which is identical to the axis of rotation of the cone. Measuring the jam-length after an initial equilibration time of 4000 time-steps the qualitative behaviour of the jam-length as shown in figure 6.11 matches results of the mean-field theory in figure 6.10 quite good. But there are also quantitative deviations due to large volume available for the unbound motors, which violates the two-state approximation.

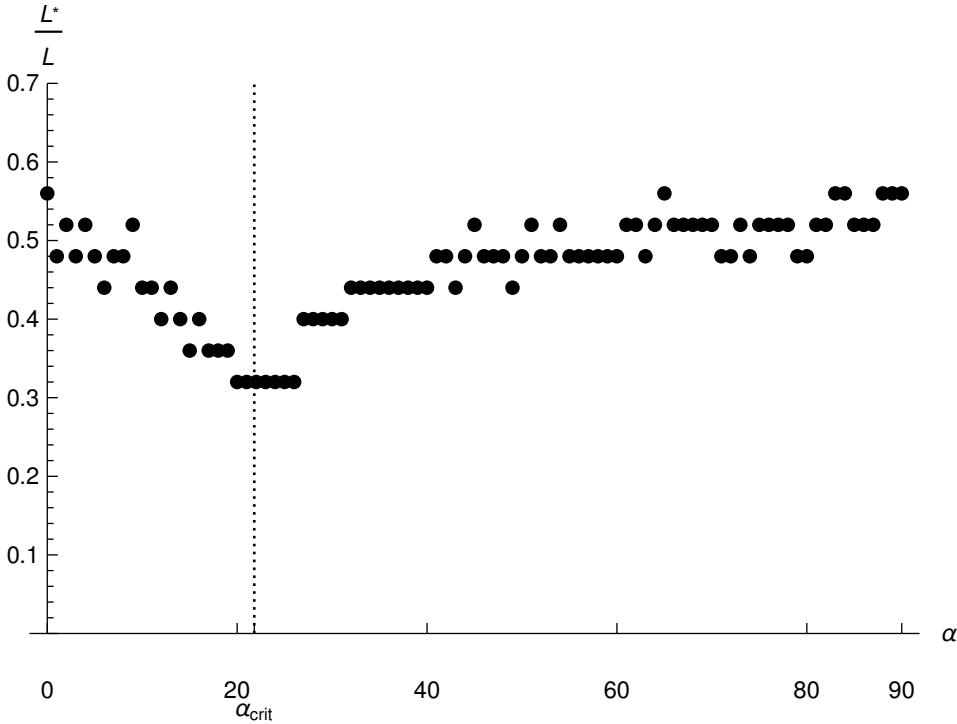


Figure 6.11. Jam length vs angle. Significant drop at  $\alpha_c$ . Parameters are:  $\tau = \tau_b = 1$ ,  $p_+ = 0.1$ ,  $p_- = 0.8$ ,  $p_b = 0.8$ ,  $p_{ub} = 0.05$ ,  $L = 25$  and  $R = 10$ .



## 7 *Discussion*

This chapter serves the purpose of discussion about the chosen strategies in this thesis and possible alternatives.

### *Solution of the shape equations*

One characteristic of the approach of using the Euler-Lagrange-equations is that its solutions are local extrema, given that the second variation does not vanish. This is useful, because you can track meta-stable solutions over a wider parameter regime as used in chapter 5. On the other hand, because the number of possible solutions is unbounded, it is hard to guarantee that a particular solution is the global minimum. A possible solution to this would be to replace  $\psi$  and  $\bar{r}$  in equation (3.1) with a finite parameter representation (e.g. by Chebyshev-series<sup>[58]</sup>, splines or a neural network) and fit the resulting parameters via a guaranteed global optimization procedure<sup>[59]</sup>. This way it should be possible to reliably find the thermodynamic stable shape. In addition, the explorable parameter regime is limited by the spherical regions discussed in section 4.2.1, since a closed neck will have a discontinuous bending angle at the neck. This could in principle be handled by a sophisticated event detection in the differential equation solver, but it gets complicated by the numerical instability once the radial coordinate gets sufficiently close to zero.

To get a complete picture of the morphology diagram of the spontaneous curvature model further analysis is necessary to either find analytically the feasible parameter regions or to reliably detect bifurcation points and systematically track the different branches.





## 8 *Summary*

Understanding the rich variety of shapes that liquid lipid membranes can have is a challenging task. Even restricting the possible shapes to be axisymmetric as in the Helfrich model introduced in section 3.1 still exposes a complex system that is not completely understood. When going even further and reducing the compartment to simple geometric forms like truncated cones shows that the volume and area conservation constraints result in a non-trivial parameter space as seen in section 3.2. This can be seen as an indication that the area and volume constraints are a main contributor to the complex shaped parameter spaces.

In chapter 4 solutions of equilibrium shapes of the parameter space of the spontaneous curvature model were calculated to get an overview of the morphologies of GUVs. Thereby the boundaries of the already known regions of the morphology diagram were extended. Unfortunately, the picture is still incomplete. But even incomplete knowledge can be useful, as shown in chapter 5, where the experimental observation of symmetry breaking shape oscillations of GUVs filled with Min-proteins could be successfully explained by a periodic but homogeneous change of the spontaneous curvature caused by the binding and unbinding of the proteins to the inner membrane surface.

A step beyond the system of isolated vesicles has been done by the investigation of concentration gradients within conic compartments. Two model systems were chosen in the case of conic compartments. Probably the simplest system available is an ideal gas in a constant external field like gravity, it has the advantage that many properties

like the free energy can be calculated analytically (cf. sections 2.2.1 and 6.1). A remaining task is the investigation of the effects when the spontaneous curvature model is considered. The corresponding equations are derived in appendix A.

The other system that is inspired by actual biological processes, are processive molecular motors. But since this is an active non-equilibrium system, analysis is much harder and numeric simulation becomes more important as used in sections 6.3 and 6.4 to get a qualitative insight in the distribution of the motors when the compartment changes. This could be extended to the case where the compartment reacts to the distribution of the motors, either due to the inhomogeneous pressure or an interaction of the motors with the compartment akin to the interaction of the Min proteins with the membrane that was observed in chapter 5.

# A Concentration gradients in flexible compartments

## A.1 Shape equations for an ideal gas in a vesicle

In this section a vesicle that is filled with an ideal gas within the earth's gravitational field is considered. The corresponding equations of evolution can be calculated by combining the energy functional of a vesicle as given by equation (3.2) plus the free energy of an ideal gas in gravity  $F$  as calculated in section 2.2.1.

$$\begin{aligned}
 \mathcal{E} &= \mathcal{E}_{\text{be}} + \Sigma A - \Delta P V + F \\
 &= \int \pi \kappa r \left( \dot{\psi} + \frac{\sin \psi}{r} - 2m \right)^2 + 2\pi \Sigma r - \pi \Delta P r^2 \sin \psi + \gamma_r (\dot{r} - \cos \psi) + \gamma_z (\dot{z} - \sin \psi) \, ds \\
 &\quad - \frac{N}{\beta} \log \left( \left( \frac{2\pi M}{h^2 \beta} \right)^{\frac{3}{2}} \pi \int e^{-\beta M g z r^2} \sin \psi \, ds \right) \\
 \delta \mathcal{E} &= \delta \int \pi \kappa r \left( \dot{\psi} + \frac{\sin \psi}{r} - 2m \right)^2 + 2\pi \Sigma r - \pi \Delta P r^2 \sin \psi + \gamma_r (\dot{r} - \cos \psi) + \gamma_z (\dot{z} - \sin \psi) \, ds \\
 &\quad - \frac{N}{\beta} \delta \int \frac{e^{-\beta M g z r^2} \sin \psi}{\zeta} \, ds.
 \end{aligned} \tag{A.1}$$

With surface tension  $\Sigma$ , pressure difference  $\Delta P$  and Lagrange multiplier functions  $\gamma_r$  and  $\gamma_z$ . As well as the shape dependent partition volume  $\zeta$

$$\zeta = \frac{Z_1}{\left( \frac{2\pi M}{h^2 \beta} \right)^{\frac{3}{2}} \pi} = \int e^{-\beta M g z r^2} \sin \psi \, ds'.$$

From equation (A.1) the shape equations can be calculated by standard calculus of variation as explained in section 2.1.

$$\begin{aligned}
\dot{\psi} &= u \\
\dot{u} &= \frac{1}{2\pi\kappa} \left( \pi r \cos \psi \left( -\Delta P - \frac{N}{\pi\beta} \frac{e^{-\beta Mgz}}{\zeta} \right) + \frac{\sin \psi}{r} \gamma_r - \frac{\cos \psi}{r} \gamma_z \right) + \frac{\sin \psi \cos \psi}{r^2} - \cos \psi \frac{u}{r} \\
\dot{r} &= \cos \psi \\
\dot{z} &= \sin \psi \\
\dot{\gamma}_r &= \pi\kappa \left( (u - 2m)^2 - \frac{\sin^2 \psi}{r^2} \right) + 2\pi\Sigma + 2\pi r \sin \psi \left( -\Delta P - \frac{N}{\pi\beta} \frac{e^{-\beta Mgz}}{\zeta} \right) \\
\dot{\gamma}_z &= NMg r^2 \sin \psi \frac{e^{-\beta Mgz}}{\zeta}.
\end{aligned} \tag{A.2}$$

with additional boundary conditions


$$\begin{aligned}
z(0) &= 0, & z(S) &= z_1 \\
\gamma_z(0) &= 0, & \gamma_z(S) &= 0
\end{aligned}$$

This shows that the difference to the shape equations shown by Seifert *et al.*

Agudo-Canalejo & Lipowsky<sup>[29,60]</sup>, apart from the two extra equations, is an effective  $P_{\text{eff}}(z) = \Delta P + \frac{N}{\pi\beta} \frac{e^{-\beta Mgz}}{\zeta}$  plus an extra term containing  $\gamma_z$ .

The shape dependence introduced by  $\zeta$  complicates the numerical solution of equation (A.2), since it requires now a self-consistent iteration on top of the shooting procedure. That is, starting with a trial shape an initial  $\zeta_0$  is calculated and with which the shape equations can be solved to obtain a new shape with which a new  $\zeta_1$  can be calculated and so on and so forth. This has to be done until the difference  $\Delta\zeta = \zeta_n - \zeta_{n-1}$  becomes zero.

## B VesicleForms.jl

The implementation of the shape equation solver is a julia reimplementa-  
tion of the matlab algorithm used by Agudo-Canalejo & Lipowsky<sup>[60]</sup>  
which both base on the algorithm sketched by Seifert *et al.*<sup>[29]</sup>. This  
code is packaged as *VesicleForms.jl*  and publicly available.

### B.1 Solving the shape equations

#### B.1.1 Conservation of area and volume

In order to ensure the conservation of area and volume it is useful to  
augment the shape equations (3.16) with the volume, area and energy  
differentials

$$\begin{aligned}\dot{A}(s) &= \frac{\pi\bar{S}}{4}\dot{\bar{r}}(s), \\ \dot{v}(s) &= \frac{\pi\bar{S}}{8}\dot{\bar{r}}(s)^2 \sin \psi(s), \\ \dot{\mathcal{E}}_{\text{be}}(s) &= \frac{\pi\bar{S}}{8}\dot{\bar{r}}(s) \left( \bar{u}(s) + \frac{\sin \psi(s)}{\bar{r}(s)} - 2\bar{m} \right)^2.\end{aligned}\quad (\text{B.1})$$

#### B.1.2 Taylor expansion near the boundary points

Due to the  $1/\bar{r}^2(s)$  terms in (3.16) numerical evaluation of the equa-  
tions near  $\bar{r} = 0$  is likely to be unstable. A way to alleviate this  
problem near the boundaries  $s = 0$  and  $s = 1$  is to expand (3.16)  
and (B.1) near those points and calculate the approximate solutions

analytically. At  $s = 0$  this yields

$$\begin{aligned}
\psi^0(ds) &= \pi\bar{S} ds\bar{u}_0 - \frac{(\pi\bar{S} ds)^3}{16} \left( \Delta\bar{P} - 2\bar{u}_0 \left( \bar{\Sigma} - 2\bar{m}\bar{u}_0 + 2\bar{m}^2 \right) \right) + \mathcal{O}(ds^5), \\
\bar{u}^0(ds) &= \bar{u}_0 - \frac{3(\pi\bar{S} ds)^2}{16} \left( \Delta\bar{P} - 2\bar{u}_0 \left( \bar{\Sigma} - 2\bar{m}\bar{u}_0 + 2\bar{m}^2 \right) \right) + \mathcal{O}(ds^4), \\
\bar{r}^0(ds) &= \pi\bar{S} ds - \frac{(\pi\bar{S} ds)^3}{6} \bar{u}_0^2 + \mathcal{O}(ds^5), \\
\bar{\gamma}_r^0(ds) &= \frac{\pi\bar{S} ds}{4} \left( \bar{\Sigma} - 2\bar{m}\bar{u}_0 + 2\bar{m}^2 \right) + \frac{(\pi\bar{S} ds)^3}{96} \left( \bar{m} \left( 3\Delta\bar{P} - 6\bar{\Sigma}\bar{u}_0 - 4\bar{u}_0^3 \right) \right. \\
&\quad \left. - 12\bar{m}^3\bar{u}_0 + 16\bar{m}^2\bar{u}_0^2 + \bar{u}_0 (2\bar{\Sigma}\bar{u}_0 - 9\Delta\bar{P}) \right) + \mathcal{O}(ds^4), \\
\bar{A}^0(ds) &= \frac{(\pi\bar{S} ds)^2}{4} - \frac{(\pi\bar{S} ds)^4}{48} \bar{u}_0^2 + \mathcal{O}(ds^6), \\
v^0(ds) &= \frac{3(\pi\bar{S} ds)^4}{16} \bar{u}_0 + \mathcal{O}(ds^6), \\
\bar{\mathcal{E}}_{\text{be}}^0(ds) &= \frac{(\pi\bar{S} ds)^2}{4} (\bar{u} - \bar{m})^2 \\
&\quad - \frac{(\pi\bar{S} ds)^4}{96} (\bar{u}_0 - \bar{m}) \left( 10\bar{m}\bar{u}_0^2 - 12\bar{m}^2\bar{u}_0 - 6\bar{\Sigma}\bar{u}_0 + 2\bar{u}_0^3 + 3\Delta\bar{P} \right) + \mathcal{O}(ds^6).
\end{aligned}$$

✍ (B.2)

While for  $s = 1$  the equations can be inferred by symmetry

$$\begin{aligned}
\psi^1(ds) &= \pi + \pi\bar{S} ds\bar{u}_1 - \frac{(\pi\bar{S} ds)^3}{16} \left( \Delta\bar{P} - 2\bar{u}_1 \left( \bar{\Sigma} - 2\bar{m}\bar{u}_1 + 2\bar{m}^2 \right) \right) + \mathcal{O}(ds^5), \\
\bar{u}^1(ds) &= \bar{u}_1 - \frac{3(\pi\bar{S} ds)^2}{16} \left( \Delta\bar{P} - 2\bar{u}_1 \left( \bar{\Sigma} - 2\bar{m}\bar{u}_1 + 2\bar{m}^2 \right) \right) + \mathcal{O}(ds^4), \\
\bar{r}^1(ds) &= -\pi\bar{S} ds + \frac{(\pi\bar{S} ds)^3}{6} \bar{u}_1^2 + \mathcal{O}(ds^5), \\
\bar{\gamma}_r^1(ds) &= \frac{\pi\bar{S} ds}{4} \left( \bar{\Sigma} - 2\bar{m}\bar{u}_1 + 2\bar{m}^2 \right) + \frac{(\pi\bar{S} ds)^3}{96} \left( \bar{m} \left( 3\Delta\bar{P} - 6\bar{\Sigma}\bar{u}_1 - 4\bar{u}_1^3 \right) \right. \\
&\quad \left. - 12\bar{m}^3\bar{u}_1 + 16\bar{m}^2\bar{u}_1^2 + \bar{u}_1 (2\bar{\Sigma}\bar{u}_1 - 9\Delta\bar{P}) \right) + \mathcal{O}(ds^4), \\
\bar{A}^1(ds) &= 1 - \frac{(\pi\bar{S} ds)^2}{4} + \frac{(\pi\bar{S} ds)^4}{48} \bar{u}_1^2 + \mathcal{O}(ds^6), \\
v^1(ds) &= v - \frac{3(\pi\bar{S} ds)^4}{16} \bar{u}_1 + \mathcal{O}(ds^6), \\
\bar{\mathcal{E}}_{\text{be}}^1(ds) &= \bar{\mathcal{E}}_{\text{be}}(1) - \frac{(\pi\bar{S} ds)^2}{4} (\bar{u} - \bar{m})^2 \\
&\quad + \frac{(\pi\bar{S} ds)^4}{96} (\bar{u}_1 - \bar{m}) \left( 10\bar{m}\bar{u}_1^2 - 12\bar{m}^2\bar{u}_1 - 6\bar{\Sigma}\bar{u}_1 + 2\bar{u}_1^3 + 3\Delta\bar{P} \right) + \mathcal{O}(ds^6).
\end{aligned}$$

(B.3)

$\bar{\mathcal{E}}_{\text{be}}(1)$  is unknown, but that is not important for the algorithm, since  $\bar{\mathcal{E}}_{\text{be}}^1(ds)$  as well as  $ds$  will be known after integration.

### B.1.3 Parameter estimation

This implementation is finding solutions to the shape equations by fixing  $\bar{m}$  as well as the area  $A$  and the volume  $V$  and therefore the reduced volume  $v^1$ . The other five parameters  $\Delta\bar{P}$ ,  $\bar{\Sigma}$ ,  $\bar{u}_0$ ,  $\bar{u}_1$  and  $\bar{S}$  are determined by using an initial guess ( e.g. via a nearby known solution ) to solve (3.16) and (B.1) using *DifferentialEquations.jl*<sup>[61]</sup> in an interval  $s \in [ds, 1 - ds]$ , the solutions at  $s = 1 - ds$  are used to compute

<sup>1</sup> While the description is written with scaled variables, version 0.1 only displays the results scaled and works internally dimensionful. The version 0.2 branch which has the ability to work in scaled variables exists but is not fully functional

$$\Delta\mathbf{u} = [ \begin{array}{l} \psi(1 - ds) - \psi^1(-ds), \\ \bar{r}(1 - ds) - \bar{r}^1(-ds), \\ \bar{\gamma}_r(1 - ds) - \bar{\gamma}_r^1(-ds), \\ \bar{A}(1 - ds) - \bar{A}^1(-ds), \\ v(1 - ds) - v^1(-ds) \end{array} ] .$$

Which the trust-region root-finding algorithm provided by *NLsolve.jl*<sup>[38]</sup> can use to adjust the five parameters such that  $\Delta\mathbf{u} < \epsilon$ .<sup>2</sup>

<sup>2</sup> usually with  $\epsilon = 10^{-12}$

### B.1.4 Testing


A good way to test the correctness of obtained solutions for  $\bar{m} = 0$  is to check whether the global shape equation<sup>[30]</sup> holds

$$3\Delta P V - 2\Sigma A = 0.$$





## C Molemoto

Molemoto  is a stochastic particle simulator for confined geometries written in C++. The aim is to simulate particles that diffuse homogeneously in the bulk and perform a biased 1D random walk along the microtubulus while taking steric interaction into account. It has a modular structure (cf. figure C.2) and is easily extendable. In its present state it supports closed and half-open tubes and cones as explained in chapter 3, bound and unbound diffusion as well as adherence to the compartment walls.

The usage of a KD-Tree for the storage of the particles changes the complexity for all operations that iterate over the particles from  $\mathcal{O}(N_x N_y N_z)$ , where  $N_i$  is the number of grid points in the  $i$ -th dimension to  $\mathcal{O}(N_p \log N_p)$  on average, where  $N_p$  is the number of particles. This enhances the runtime of the simulations in most cases significantly, especially in 3D. This has the positive side effect, that automatically enforces the steric interaction, since each node of the tree can only store one particle.

*KD-Tree:* A KD-Tree constructs a tree of points in a  $k$ -dimensional space by assigning  $k$ -dimensional points to its nodes and from each node branch to branches resulting from dividing the space by hyperplanes and sorting the following nodes with respect to the half-space lives in relative to the hyperplane. At each level one hyperplane perpendicular to the former is chosen (see figure C.3).

Time = 4000 Number of agents = 188

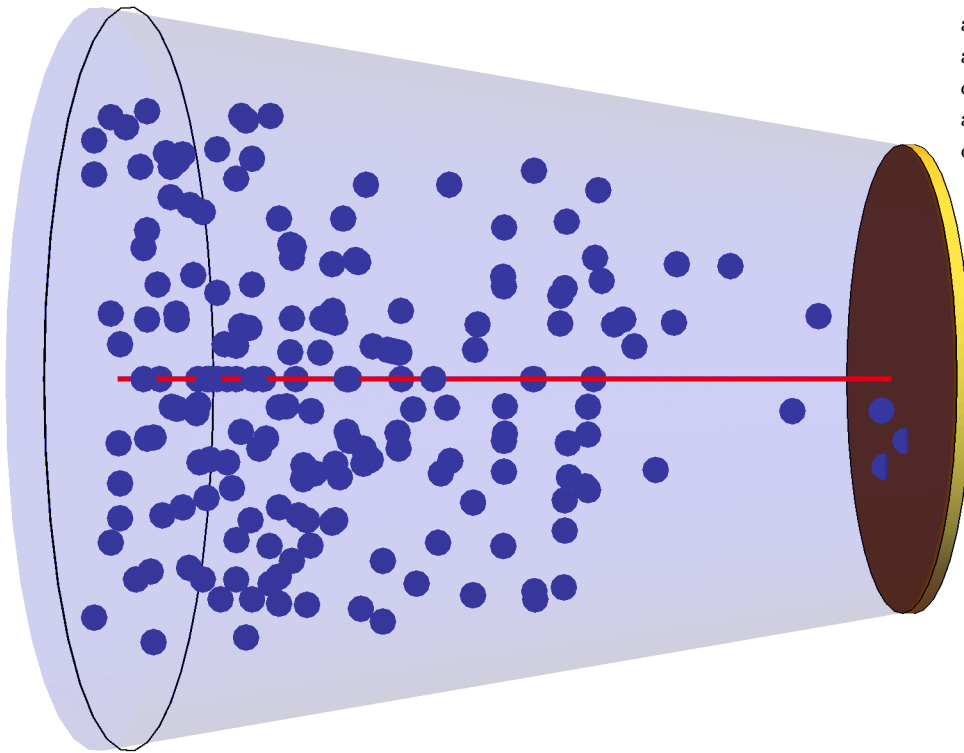


Figure C.1. Snapshot of a Molemoto simulation. Blue spheres represent molecular motors and the microtubulus is shown in red. The yellow end is a closed boundary whereas the black ring at the other end indicates an open boundary. The shell has also reflective boundary conditions.

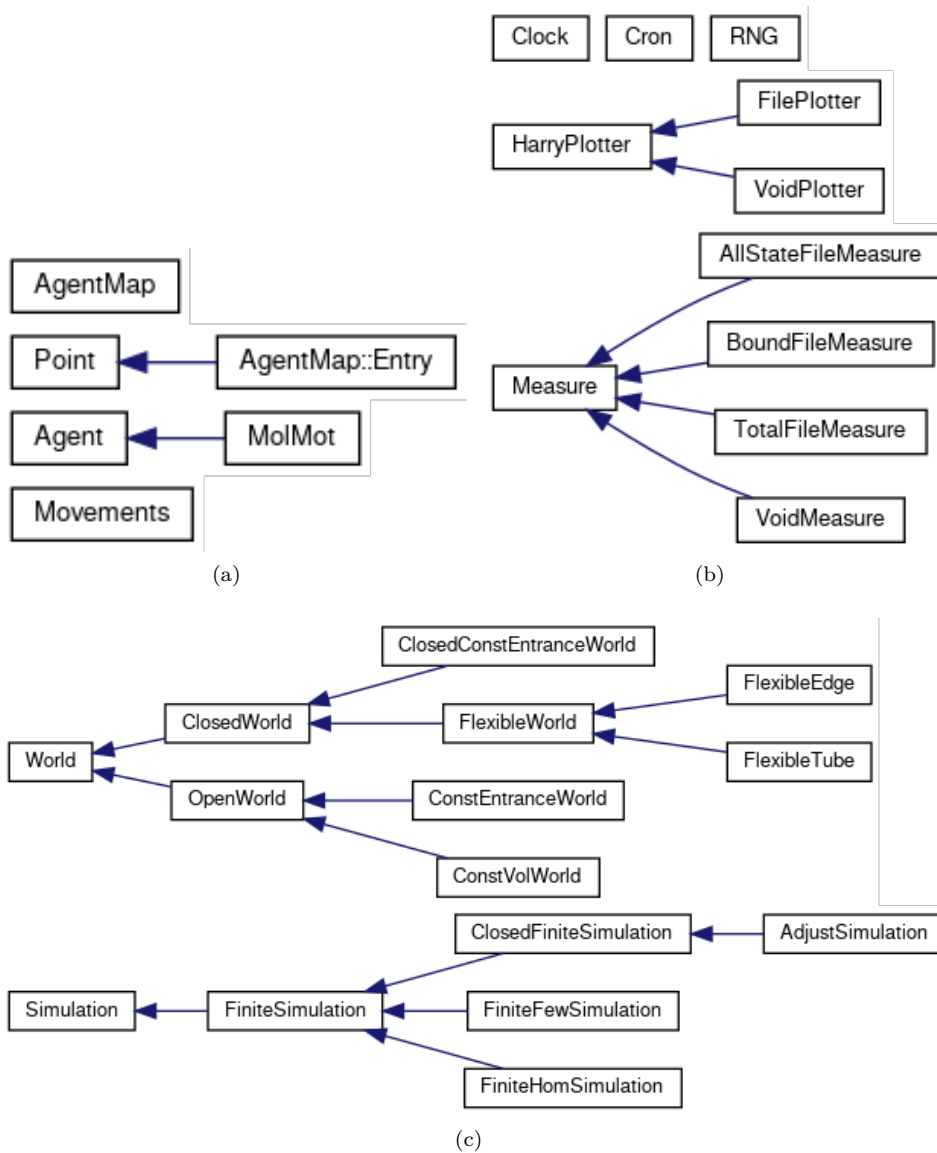


Figure C.2. Class hierarchy of Molemoto. Every class is a possible point of entry to extend the program.

Agents are stored in the AgentMap and associated with a Point in space and move according to their Movement (figure C.2a). A few utility classes allow controlling the scheduling of events (Clock, Cron, RNG), measuring observables (Measure and subclasses) and visualizing results (HarryPlotter and subclasses) (figure C.2b). Different geometries are implemented by instances of sub-classes of the World class. Coordination of the dynamics are handled by different Simulation classes (figure C.2c).

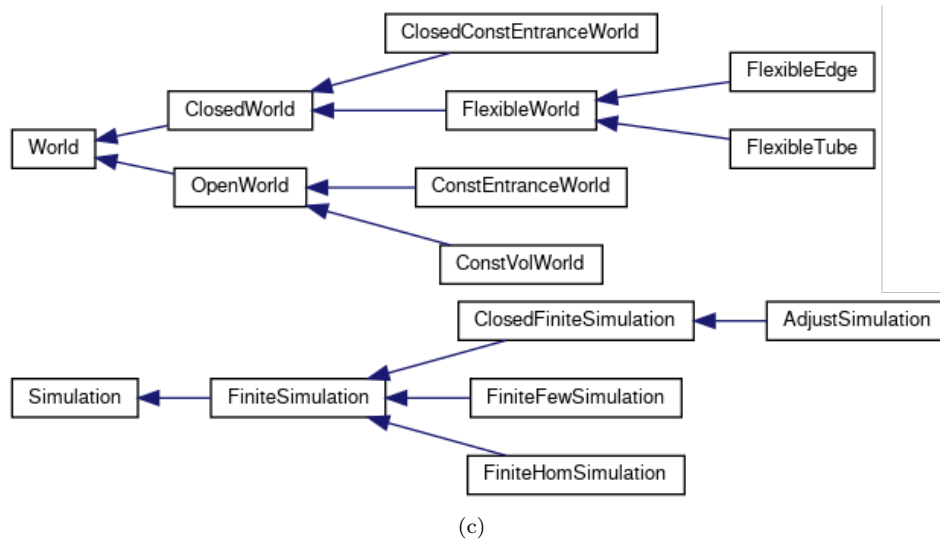
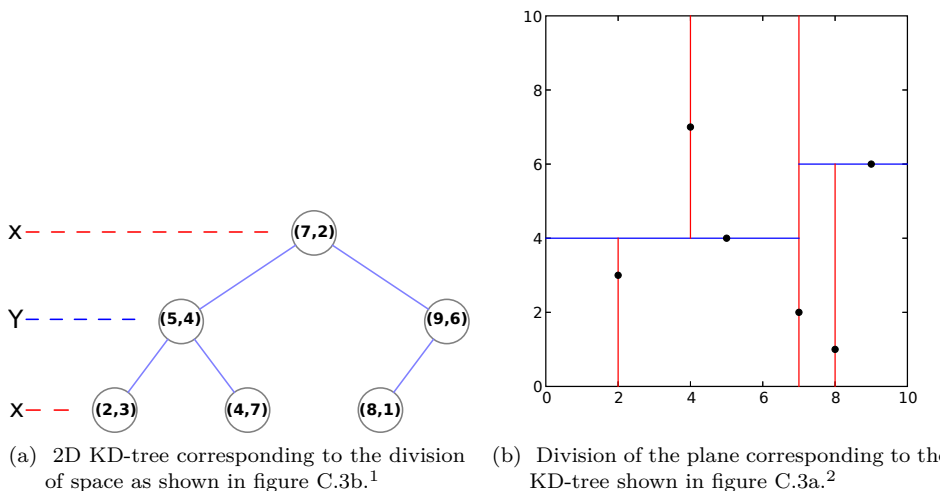


Figure C.3. Construction of a KD-tree.



(a) 2D KD-tree corresponding to the division of space as shown in figure C.3b.<sup>1</sup>

(b) Division of the plane corresponding to the KD-tree shown in figure C.3a.<sup>2</sup>

<sup>1</sup>: „Tree\_0001“ by MYguel - Own work. Licensed under Public Domain via Wikimedia Commons - [https://commons.wikimedia.org/wiki/File:Tree\\_0001.svg#/media/File:Tree\\_0001.svg](https://commons.wikimedia.org/wiki/File:Tree_0001.svg#/media/File:Tree_0001.svg)

<sup>2</sup>: „Kdtree\_2d“ by Original uploader was KiwiSunset at en.wikipedia - Transferred from en.wikipedia; transfer was stated to be made by User:KindDragon33.. Licensed under CC BY-SA 3.0 via Wikimedia Commons - [https://commons.wikimedia.org/wiki/File:Kdtree\\_2d.svg#/media/File:Kdtree\\_2d.svg](https://commons.wikimedia.org/wiki/File:Kdtree_2d.svg#/media/File:Kdtree_2d.svg)



## References

1. Bezanson, J., Edelman, A., Karpinski, S. & Shah, V. B. Julia: A Fresh Approach to Numerical Computing. *SIAM Rev.* doi: 10.1137/141000671 (2017) (cit. on pp. vii, 43).
2. Diez-Silva, M., Dao, M., Han, J., Lim, C.-T. & Suresh, S. Shape and Biomechanical Characteristics of Human Red Blood Cells in Health and Disease. *MRS Bull.* **35**, 382–388. doi: 10.1557/mrs2010.571 (2010) (cit. on p. 1).
3. *114903-050-CAFC50E4.Jpg (JPEG Image, 1600 × 1469 Pixels) - Scaled (47%)* <http://media-3.web.britannica.com/eb-media/03/114903-050-CAFC50E4.jpg> (2020) (cit. on p. 2).
4. *1200px-Liposome\_scheme-En.Svg.Png (PNG Image, 1200 × 850 Pixels) - Scaled (82%)* [https://upload.wikimedia.org/wikipedia/commons/thumb/0/01/Liposome\\_scheme-en.svg/1200px-Liposome\\_scheme-en.svg.png](https://upload.wikimedia.org/wikipedia/commons/thumb/0/01/Liposome_scheme-en.svg/1200px-Liposome_scheme-en.svg.png) (2020) (cit. on p. 2).
5. Ghosh, R., Satarifard, V., Grafmüller, A. & Lipowsky, R. Spherical Nanovesicles Transform into a Multitude of Nonspherical Shapes. *Nano Letters* **19**, 7703–7711. doi: 10.1021/acs.nanolett.9b02646 (2019) (cit. on p. 3).
6. Litschel, T., Ramm, B., Maas, R., Heymann, M. & Schwille, P. Beating Vesicles: Encapsulated Protein Oscillations Cause Dynamic Membrane Deformations. *Angew. Chemie Int. Ed.* **57**, 16286–16290. doi: 10.1002/anie.201808750. pmid: 30270475 (2018) (cit. on pp. 3, 39, 40, 42).
7. Tanaka, T., Sano, R., Yamashita, Y. & Yamazaki, M. Shape Changes and Vesicle Fission of Giant Unilamellar Vesicles of Liquid-Ordered Phase Membrane Induced by Lysophosphatidylcholine. *Langmuir* **20**, 9526–9534. doi: 10.1021/la049481g (2004) (cit. on p. 3).
8. Georgiev, V.N. *et al.* Area Increase and Budding in Giant Vesicles Triggered by Light: Behind the Scene. *Advanced Science* **5**, 1800432. doi: 10.1002/advs.201800432 (2018) (cit. on p. 3).
9. Bergenholtz, J. & Wagner, N.J. Formation of AOT/Brine Multilamellar Vesicles. *Langmuir* **12**, 3122–3126. doi: 10.1021/la950696n (1996) (cit. on p. 3).

10. Kim, S., Turker, M. S., Chi, E. Y., Sela, S. & Martin, G. M. Preparation of Multi-vesicular Liposomes. *Biochimica et Biophysica Acta (BBA) - Biomembranes* **728**, 339–348. doi: 10.1016/0005-2736(83)90504-7 (1983) (cit. on p. 3).
11. Wesolowska, O., Michalak, K., Maniewska, J. & Hendrich, A. B. Giant Unilamellar Vesicles - a Perfect Tool to Visualize Phase Separation and Lipid Rafts in Model Systems. *Acta Biochimica Polonica* **56**. doi: 10.18388/abp.2009\_2514 (1 2009) (cit. on p. 3).
12. Kahya, N., Scherfeld, D., Bacia, K. & Schwille, P. Lipid Domain Formation and Dynamics in Giant Unilamellar Vesicles Explored by Fluorescence Correlation Spectroscopy. *Journal of Structural Biology* **147**, 77–89. doi: 10.1016/j.jsb.2003.09.021 (2004) (cit. on p. 3).
13. Li & Cheng, J.-X. Coexisting Stripe- and Patch-Shaped Domains in Giant Unilamellar Vesicles. *Biochemistry* **45**, 11819–11826. doi: 10.1021/bi060808h (2006) (cit. on p. 3).
14. Schwille, P. *et al.* *MaxSynBio: Avenues Towards Creating Cells from the Bottom Up* doi: 10.1002/anie.201802288 (2018) (cit. on p. 3).
15. Merkle, D., Kahya, N. & Schwille, P. Reconstitution and Anchoring of Cytoskeleton inside Giant Unilamellar Vesicles. *ChemBioChem* **9**, 2673–2681. doi: 10.1002/cbic.200800340 (2008) (cit. on p. 3).
16. Funk, P. *Variationsrechnung Und Ihre Anwendung in Physik Und Technik* doi: 10.1007/978-3-642-88597-6 (Springer Berlin Heidelberg, 1970) (cit. on pp. 5, 14).
17. Nolting, W. *Grundkurs Theoretische Physik 6* doi: 10.1007/978-3-642-25393-5 (Springer Berlin Heidelberg, 2014) (cit. on p. 8).
18. Lipowsky, R. *et al.* Droplets, Bubbles, and Vesicles at Chemically Structured Surfaces. *Journal of Physics: Condensed Matter* **17**, S537–S558. doi: 10.1088/0953-8984/17/9/015 (2005) (cit. on p. 11).
19. Keller, C. A., Glasmästar, K., Zhdanov, V. P. & Kasemo, B. Formation of Supported Membranes from Vesicles. *Physical Review Letters* **84**, 5443–5446. doi: 10.1103/PhysRevLett.84.5443 (2000) (cit. on p. 11).
20. Jeon, N. L. *et al.* Generation of Solution and Surface Gradients Using Microfluidic Systems. *Langmuir*. doi: 10.1021/la000600b (2000) (cit. on p. 11).
21. Hiratsuka, Y., Tada, T., Oiwa, K., Kanayama, T. & Uyeda, T. Q. Controlling the Direction of Kinesin-Driven Microtubule Movements along Microlithographic Tracks. *Biophys. J.* doi: 10.1016/S0006-3495(01)75809-2 (2001) (cit. on p. 11).
22. Hochmuth, R. M. *Micropipette Aspiration of Living Cells* doi: 10.1016/S0021-9290(99)00175-X. pmid: 10609514 (2000) (cit. on p. 11).

23. Tian, A., Johnson, C., Wang, W. & Baumgart, T. Line Tension at Fluid Membrane Domain Boundaries Measured by Micropipette Aspiration. *Phys. Rev. Lett.* doi: 10.1103/PhysRevLett.98.208102 (2007) (cit. on p. 11).
24. Karimi, M. *et al.* Asymmetric Ionic Conditions Generate Large Membrane Curvatures. *Nano Lett.* doi: 10.1021/acs.nanolett.8b03584 (2018) (cit. on p. 11).
25. Bhatia, T., Agudo-Canalejo, J., Dimova, R. & Lipowsky, R. Membrane Nanotubes Increase the Robustness of Giant Vesicles. *ACS Nano* **12**, 4478–4485. doi: 10.1021/acs.nano.8b00640 (2018) (cit. on p. 11).
26. Menger, F. M. & Keiper, J. S. Chemistry and Physics of Giant Vesicles as Biomembrane Models. *Curr. Opin. Chem. Biol.* doi: 10.1016/S1367-5931(98)80110-5 (1998) (cit. on p. 12).
27. ROBERTSON, J. D. The Ultrastructure of Cell Membranes and Their Derivatives. *Biochem. Soc. Symp.* (1959) (cit. on p. 12).
28. Helfrich, W. Elastic Properties of Lipid Bilayers Elastic Properties of Lipid Bilayers: Theory and Possible Experiments. *Z. Naturforsch* (1973) (cit. on p. 12).
29. Seifert, U., Berndl, K. & Lipowsky, R. Shape Transformations of Vesicles: Phase Diagram for Spontaneous- Curvature and Bilayer-Coupling Models. *Phys. Rev. A* **44**, 1182–1202. doi: 10.1103/PhysRevA.44.1182. pmid: 9906067 (1991) (cit. on pp. 12, 27, 28, 32, 33, 76, 77).
30. Lipowsky, R. Understanding Giant Vesicles – a Theoretical Perspective. *Giant Vesicle B.* doi: 10.1201/9781315152516 (2019) (cit. on pp. 12, 29, 33, 79).
31. Abel, N. H. in *Oeuvres Complètes Niels Henrik Abel* (eds. Sylow, L. & Lie, S.) 66–94 (Cambridge University Press, 2013). doi: 10.1017/CB09781139245807.008 (cit. on p. 18).
32. Inc., W. R. Mathematica, Version 12.0 (cit. on p. 19).
33. Bærentzen, J. A., Gravesen, J., Anton, F. & Aanaes, H. in *Guide to Computational Geometry Processing: Foundations, Algorithms, and Methods* (eds. Bærentzen, J. A., Gravesen, J., Anton, F. & Aanaes, H.) 143–158 (Springer, 2012). doi: 10.1007/978-1-4471-4075-7\_8 (cit. on p. 21).
34. Irons, M. L. The Curvature and Geodesics of the Torus, 19 (2005) (cit. on p. 22).
35. Deuling, H. & Helfrich, W. The Curvature Elasticity of Fluid Membranes : A Catalogue of Vesicle Shapes. *J. Phys.* **37**, 1335–1345. doi: 10.1051/jphys:0197600370110133500 (1976) (cit. on p. 27).
36. Bhatia, T., Christ, S., Steinkühler, J., Dimova, R. & Lipowsky, R. Simple Sugars Shape Giant Vesicles into Multispheres with Many Membrane Necks. *Soft Matter* **16**, 1246–1258. doi: 10.1039/C9SM01890E (2020) (cit. on p. 32).

37. Fourcade, B., Miao, L., Rao, M., Wortis, M. & Zia, R. K. P. Scaling Analysis of Narrow Necks in Curvature Models of Fluid Lipid-Bilayer Vesicles. *Physical Review E* **49**, 5276–5286. doi: 10.1103/PhysRevE.49.5276 (1994) (cit. on pp. 34, 35).
38. Mogensen, P. K. & Lyon, S. JuliaNLSolvers/NLsolve.Jl: Zenodo Release. doi: 10.5281/ZENODO.2682215 (2019) (cit. on pp. 36, 79).
39. Abkarian, M., Loiseau, E. & Massiera, G. Continuous Droplet Interface Crossing Encapsulation (cDICE) for High Throughput Monodisperse Vesicle Design. *Soft Matter* **7**, 4610–4614. doi: 10.1039/C1SM05239J (2011) (cit. on p. 39).
40. Hu, Z., Gogol, E. P. & Lutkenhaus, J. Dynamic Assembly of MinD on Phospholipid Vesicles Regulated by ATP and MinE. *Proceedings of the National Academy of Sciences* **99**, 6761–6766. doi: 10.1073/pnas.102059099. pmid: 11983867 (2002) (cit. on pp. 39, 53).
41. Christ, S., Litschel, T., Schwille, P. & Lipowsky, R. Active Shape Oscillations of Giant Vesicles with Cyclic Closure and Opening of Membrane Necks. Manuscript Submitted for Publication. (2020) (cit. on pp. 40, 42, 43, 45–48, 53, 54).
42. Schindelin, J. *et al.* Fiji: An Open-Source Platform for Biological-Image Analysis. *Nature Methods* **9**, 676–682. doi: 10.1038/nmeth.2019 (2012) (cit. on p. 43).
43. Ku, H. H. *Notes on the Use of Propagation of Error Formulas* (National Bureau of Standards, 1966) (cit. on p. 43).
44. Giordano, M. Uncertainty Propagation with Functionally Correlated Quantities. *ArXiv e-prints*. arXiv: 1610.08716 [physics.data-an] (2016) (cit. on p. 43).
45. Dajkovic, A. & Lutkenhaus, J. Z Ring as Executor of Bacterial Cell Division. doi: 10.1159/000094050 (2006) (cit. on p. 52).
46. Zieske, K. & Schwille, P. Reconstitution of Self-Organizing Protein Gradients as Spatial Cues in Cell-Free Systems. *eLife* **3**, e03949 (2014) (cit. on p. 52).
47. Loose, M., Fischer-Friedrich, E., Herold, C., Kruse, K. & P. Schwille. Min Protein Patterns Emerge from Rapid Rebinding and Membrane Interaction of MinE. *Nature Struct. Mol. Biol.* **18**, 577–583 (2011) (cit. on p. 53).
48. Mogensen, P. K. & Riseth, A. N. Optim: A Mathematical Optimization Package for Julia. *Journal of Open Source Software* **3**, 615. doi: 10.21105/joss.00615 (2018) (cit. on p. 54).
49. Appert-Rolland, C., Ebbinghaus, M. & Santen, L. Intracellular Transport Driven by Cytoskeletal Motors: General Mechanisms and Defects. *Phys. Rep.* **593**, 1–59. doi: 10.1016/j.physrep.2015.07.001 (2015) (cit. on p. 57).
50. Reck-Peterson, S. L. *et al.* Single-Molecule Analysis of Dynein Processivity and Stepping Behavior. *Cell*. doi: 10.1016/j.cell.2006.05.046. pmid: 16873064 (2006) (cit. on p. 58).



51. Vale, R. D. The Way Things Move: Looking Under the Hood of Molecular Motor Proteins. *Science* **288**, 88–95. doi: 10.1126/science.288.5463.88 (2000) (cit. on p. 58).
52. Tabb, J. S., Molyneaux, B. J., Cohen, D. L., Kuznetsov, S. A. & Langford, G. M. Transport of ER Vesicles on Actin Filaments in Neurons by Myosin V. *Journal of Cell Science* **111**, 3221–3234. pmid: 9763516 (1998) (cit. on p. 58).
53. Vuppalachchi, D., Willis, D. E. & Twiss, J. L. in *Cell Biology of the Axon* (ed. Koenig, E.) 293–304 (Springer, 2009). doi: 10.1007/400\_2009\_16 (cit. on p. 58).
54. Welte, M. A. Fat on the Move: Intracellular Motion of Lipid Droplets. *Biochemical Society Transactions* **37**, 991–996. doi: 10.1042/BST0370991 (2009) (cit. on p. 58).
55. Lyman, M. G. & Enquist, L. W. Herpesvirus Interactions with the Host Cytoskeleton. *Journal of Virology* **83**, 2058–2066. doi: 10.1128/JVI.01718-08. pmid: 18842724 (2009) (cit. on p. 58).
56. Hollenbeck, P. J. & Saxton, W. M. The Axonal Transport of Mitochondria. *Journal of Cell Science* **118**, 5411–5419. doi: 10.1242/jcs.02745. pmid: 16306220 (2005) (cit. on p. 58).
57. Müller, M. J. I., Klumpp, S. & Lipowsky, R. Molecular Motor Traffic in a Half-Open Tube. *J. Phys. Condens. Matter* **17**, S3839–S3850. doi: 10.1088/0953-8984/17/47/014. pmid: 21690728 (2005) (cit. on pp. 59–62).
58. Hernández, M. Chebyshev’s Approximation Algorithms and Applications. *Comput. Math. with Appl.* **41**, 433–445. doi: 10.1016/S0898-1221(00)00286-8 (2001) (cit. on p. 71).
59. Tucker, W. *Validated Numerics: A Short Introduction to Rigorous Computations* (2011) (cit. on p. 71).
60. Agudo-Canalejo, J. & Lipowsky, R. Stabilization of Membrane Necks by Adhesive Particles, Substrate Surfaces, and Constriction Forces. *Soft Matter* **12**, 8155–8166. doi: 10.1039/C6SM01481J (2016) (cit. on pp. 76, 77).
61. Rackauckas, C. & Nie, Q. DifferentialEquations.jl – A Performant and Feature-Rich Ecosystem for Solving Differential Equations in Julia. *J. Open Res. Softw.* **5**. doi: 10.5334/jors.151 (2017) (cit. on p. 79).



## *Glossary*

---

<b>Notation</b>	<b>Description</b>	<b>Page List</b>
$A$	Surface area	12, 13, 17, 18, 21–23, 43, 44, 75, 77, 79, 81, 83
$a$	Lattice constant of the discretization of space	69
$A_u$	Area of unduloid	35
$A$	First kink of the contour of a truncated cone	16, 17, 21
$\bar{A}$	Scaled area	13, 77–79
$B_{\text{op}}$	Bifurcation point of prolates and prolate-sphere shapes	44, 45, 47
$B$	Second kink of the contour of a truncated cone	16, 17, 21
$D$	Discontinuous transition between prolates and oblates	28

---

Notation	Description	Page List
$D^{\text{pear}}$	Discontinuous transition between symmetric and asymmetric prolates	32, 33
$D^{\text{sto}}$	Discontinuous transition between oblates and stomatocytes	28
$D_{\text{ub}}$	Diffusion constant of unbound molecular motors	59, 60, 62–64
$\mathcal{E}_{\text{be}}$	Bending energy (functional)	12, 21, 24, 28, 44, 47, 75
$\mathcal{E}_{\text{be,k}}$	Bending energy contribution of the kinks	21–24
$\mathcal{E}_{\text{be,s}}$	Bending energy contribution of the shell surface	21, 24
$\bar{\mathcal{E}}$	Scaled energy functional	13, 14
$\bar{\mathcal{E}}_{\text{be}}$	Scaled bending energy (functional)	13, 14, 44–47, 56, 78, 79
$\bar{\mathcal{E}}_{\text{be}}^{\text{asym}}$	Scaled bending energy (functional) of the asymmetric branch	44
$\bar{\mathcal{E}}_{\text{be}}^{\text{sym}}$	Scaled bending energy (functional) of the symmetric branch	44
$\bar{\mathcal{E}}_{\text{tot}}$	Scaled total energy	56
$F$	Free energy	8, 55, 59, 75
$\bar{F}$	Scaled free energy	55, 56

Notation	Description	Page List
$\mathcal{H}$	Hamilton function	8, 9
$K$	Desorption constant/ ratio of unbinding to binding events	60, 61, 63, 64, 68
$L$	Length/height of a (truncated) cone	9, 10, 16–19, 21, 24, 25, 56, 62–69
$L_*$	Jam-length	60, 61, 64, 66, 67
$L_{1+1}$	Limit shapes with two spheres of different size	32, 33
$L_{2^*}$	Limit shapes with two equally sized spheres	33, 36
$L_{\text{ps}}$	Limit shapes with one sphere and one prolate	44, 48
$L^{\text{sto}}$	Limit shape of two spheres where one is folded into the other	28
$L_\star$	Decay length	64, 68
$M$	Mass of an ideal gas particle	8–10, 56, 75, 76
$\mathcal{M}$	Mean curvature	12, 13, 21–23

Notation	Description	Page List
$m$	Spontaneous curvature	12, 13, 18, 21, 24, 25, 46, 56, 75, 76
$M^{\text{sto}}$	Point of stomatocytes with maximal volume	28
$\bar{\mathcal{M}}$	Scaled mean curvature	13
$\bar{m}$	Scaled spontaneous curvature	13–15, 27, 29–34, 36, 37, 43–48, 51, 53, 54, 77–79
$N$	Number of particles	8, 56, 63, 75, 76
$n$	Total number of spheres of multisphere vesicles	29–31
$n_l$	Number of large spheres of multisphere vesicles	30, 32
$n_s$	Number of small spheres of multisphere vesicles	30–32
$\mathbf{p}$	Impulse vector	8, 9
$p_+$	Forward moving probability of molecular motors	62–64, 68, 69

Notation	Description	Page List
$p_-$	Backwards moving probability of molecular motors	62–64, 68, 69
$p_b$	Binding probability of molecular motors	62, 68, 69
$p_{ub}$	Detaching probability of molecular motors	62, 68, 69
$R$	Radius of a (truncated) cone	9, 10, 16–19, 21, 23–25, 56, 64–69
$r$	Radial coordinate in a cylindrical coordinate system	9, 10, 14, 16, 17, 21, 35, 63–67, 75, 76, 99, 100
$\mathbf{r}$	Position vector	8, 9
$R_{ne}$	Neck radius of a vesicle	42, 43, 46, 48, 50, 51
$R_{ve}$	Vesicle radius	12, 13, 43, 44, 46, 48, 51

---

Notation	Description	Page List
$\bar{r}$	Scaled radial coordinate	14, 15, 35, 71, 77–79
$\bar{R}_l$	Scaled larger radius of multisphere vesicles	29, 30, 32, 33, 35–37
$\bar{R}_{ne}$	Scaled neck radius of a vesicle	34–37, 43, 46–49, 51, 54
$\bar{R}_s$	Scaled smaller radius of multisphere vesicles	29, 30, 32–37
$S$	Total arc-length	13, 14, 76
$s$	Point along the arc length of the contour of a shape	14–16, 34, 35, 75
$SI^{ob}$	Point where oblate solutions start to self-intersect	28
$\bar{S}$	Scaled arc-length	13–15, 35, 77–79
$T$	Temperature	8, 46
$u$	Curvature in a natural parameterisation	76
$\bar{u}$	Scaled curvature	14, 15, 77–79

---



Notation	Description	Page List
$V$	Volume	8–10, 12, 13, 17, 18, 24, 25, 43, 56, 75, 79
$v$	Volume-to-area ratio / reduced volume	13–15, 18, 24, 25, 27, 28, 30–34, 36, 43–51, 56, 77–79
$v_b$	Signed velocity of bound molecular motors	59, 60, 62
$V_u$	Volume of undoloid	35
$Z$	Partition sum	8
$z$	Height or z-coordinate in a cylindrical coordinate system	8–10, 14, 16, 17, 21, 22, 36, 63, 65–67, 75, 76, 99

---

Notation	Description	Page List
$Z_1$	One-particle partition sum	8, 9, 56, 75
$\Delta P$	Osmotic pressure difference of inner and outer solution	12, 13, 75, 76, 79
$\Delta \bar{P}$	Scaled osmotic pressure difference of inner and outer solution	13–15, 78, 79
$\Delta u$	Residual for optimization	79
$\Sigma$	Surface tension	12, 13, 75, 76, 79
$\bar{\Sigma}$	Scaled surface tension	13–15, 78, 79
$\Phi$	Aspect ratio	18, 19
$\alpha$	Opening angle of a (truncated) cone	10, 16–19, 21–24, 55–57, 64–67, 69
$\beta$	Inverse of thermal energy	8–10, 56, 75, 76
$\gamma_+$	Forward moving rate of molecular motors	62

---

Notation	Description	Page List
$\gamma_-$	Backwards moving rate of molecular motors	62
$\gamma_b$	Binding rate of molecular motors	60, 62
$\gamma_r$	Lagrange multiplier function for $r$ in a natural parameterisation	75, 76
$\gamma_{ub}$	Detaching rate of molecular motors	60, 62
$\gamma_z$	Lagrange multiplier function for $z$ in a natural parameterisation	75, 76
$\bar{\gamma}_r$	Scaled $\gamma_r$	14, 15, 78, 79
$\zeta$	Partition volume of an ideal gas	75, 76
$\kappa$	Bending rigidity of vesicles	12, 13, 21, 22, 24, 28, 44, 46, 47, 55, 56, 75, 76
$\mu$	Relative motility of bound and unbound motors	63, 64
$\rho_0$	Particle density of molecular motors at the jam-length defining point	66, 67
$\rho_b$	Particle density of bound molecular motors	59, 62, 63
$\rho_{b, \text{in}}$	Particle density of bound molecular motors at the open boundary	60, 61

---

<b>Notation</b>	<b>Description</b>	<b>Page List</b>
$\rho_{\text{ub}}$	Particle density of unbound molecular motors	62, 63
$\sigma$	General cross section	62, 63
$\sigma_{\text{cyl}}$	Cross-section of a cylinder	59, 60
$\tau$	Mean diffusion time of unbound motors	62, 69
$\tau_b$	Mean diffusion time of bound motors	62–64, 69
$\psi$	Bending angle. Angle between the tangent of the contour of a shape and the $r$ -axis	14, 15, 29, 34, 35, 71, 75–79

---

## *Numerical Constants*

<b>Notation</b>	<b>Description</b>	<b>Page List</b>
$e$	Euler's constant	9, 10, 75, 76
$g$	Standard gravitational acceleration of the earth	8–10, 75, 76
$h$	Planck's constant	9, 10, 75
$k_{\text{B}}$	Boltzmann's constant	8, 46

$\pi$	Archimedes' constant	9, 10, 12–15, 17, 18, 21, 22, 24, 28, 34, 35, 43, 44, 46, 47, 54–56, 63–66, 75–78
-------	----------------------	---

---


## *Abbreviations*

---

<b>Notation</b>	<b>Description</b>	<b>Page List</b>
ATP	adenosine triphosphate	39, 40, 58, 59
cDICE	continuous droplet interface crossing encapsulation	39
DIC	differential interference contrast microscopy	39
DOPC	1,2-Dioleoyl-sn-glycero-3-phosphocholine	39
DOPG	1,2-Dioleoyl-sn-glycero-3-phosphoglycerol	39
eGFP	enhanced green fluorescent protein	39, 40
GUV	giant unilamellar vesicle	2, 3, 12, 39, 40, 43, 47, 53, 54, 73
LUV	large unilamellar vesicle	12
SUV	small unilamellar vesicle	12

---

# List of source links

viii.1 :

[https://github.com/sisl/tufte\\_algorithms\\_book](https://github.com/sisl/tufte_algorithms_book)

10.1  (2.11):

[https://gitlab.mpikg.mpg.de/christ/phdthesis\\_code/-/blob/v0.1/PartitionSum\\_IdeaGas\\_Cone.wls](https://gitlab.mpikg.mpg.de/christ/phdthesis_code/-/blob/v0.1/PartitionSum_IdeaGas_Cone.wls)

14.1  (3.16):

[https://gitlab.mpikg.mpg.de/paper/min\\_GUV\\_oscillations\\_Code/-/blob/master/Deriving\\_Shape\\_Equations.wl](https://gitlab.mpikg.mpg.de/paper/min_GUV_oscillations_Code/-/blob/master/Deriving_Shape_Equations.wl)

19.1  (3.25):


[https://gitlab.mpikg.mpg.de/christ/phdthesis\\_code/-/blob/v0.1/BendConeGas.wls](https://gitlab.mpikg.mpg.de/christ/phdthesis_code/-/blob/v0.1/BendConeGas.wls)

20.2  (3.25):


[https://gitlab.mpikg.mpg.de/christ/phdthesis\\_code/-/blob/v0.1/cone\\_parameter\\_region.wls](https://gitlab.mpikg.mpg.de/christ/phdthesis_code/-/blob/v0.1/cone_parameter_region.wls)

24.1  (3.33):

[https://gitlab.mpikg.mpg.de/christ/phdthesis\\_code/-/blob/v0.1/KinkRadius.wls](https://gitlab.mpikg.mpg.de/christ/phdthesis_code/-/blob/v0.1/KinkRadius.wls)

40.1 :

[https://onlinelibrary.wiley.com/action/downloadSupplement?doi=10.1002%2Fanie.201808750&file=anie201808750-sup-0001-Video\\_S6.mp4](https://onlinelibrary.wiley.com/action/downloadSupplement?doi=10.1002%2Fanie.201808750&file=anie201808750-sup-0001-Video_S6.mp4)

40.2 :

[https://onlinelibrary.wiley.com/action/downloadSupplement?doi=10.1002%2Fanie.201808750&file=anie201808750-sup-0001-Video\\_S6.mp4](https://onlinelibrary.wiley.com/action/downloadSupplement?doi=10.1002%2Fanie.201808750&file=anie201808750-sup-0001-Video_S6.mp4)

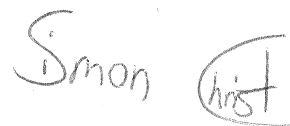


- 43.1 :  
[https://gitlab.mpikg.mpg.de/paper/min\\_GUV\\_oscillations\\_Code/-/tree/v0.1/analyse\\_frames](https://gitlab.mpikg.mpg.de/paper/min_GUV_oscillations_Code/-/tree/v0.1/analyse_frames)
- 52.1 :  
[https://onlinelibrary.wiley.com/action/downloadSupplement?doi=10.1002%2Fanie.201808750&file=anie201808750-sup-0001-Video\\_S6.mp4](https://onlinelibrary.wiley.com/action/downloadSupplement?doi=10.1002%2Fanie.201808750&file=anie201808750-sup-0001-Video_S6.mp4)
- 52.2 :  
[https://onlinelibrary.wiley.com/action/downloadSupplement?doi=10.1002%2Fanie.201808750&file=anie201808750-sup-0001-Video\\_S6.mp4](https://onlinelibrary.wiley.com/action/downloadSupplement?doi=10.1002%2Fanie.201808750&file=anie201808750-sup-0001-Video_S6.mp4)
- 54.1 :  
[https://gitlab.mpikg.mpg.de/paper/min\\_GUV\\_oscillations\\_Code/-/blob/v0.1/plots/r\(t\)\\_v0\\_670.jl#L46](https://gitlab.mpikg.mpg.de/paper/min_GUV_oscillations_Code/-/blob/v0.1/plots/r(t)_v0_670.jl#L46)
- 67.1  (6.33):  
[https://gitlab.mpikg.mpg.de/christ/phdthesis\\_code/-/blob/v0.1/JamLengthVSOpeningAngle.wls](https://gitlab.mpikg.mpg.de/christ/phdthesis_code/-/blob/v0.1/JamLengthVSOpeningAngle.wls)
- 68.1  (6.34):  
[https://gitlab.mpikg.mpg.de/christ/phdthesis\\_code/-/blob/v0.1/JamLengthGenK.wls](https://gitlab.mpikg.mpg.de/christ/phdthesis_code/-/blob/v0.1/JamLengthGenK.wls)
- 68.2  (6.35):  
[https://gitlab.mpikg.mpg.de/christ/phdthesis\\_code/-/blob/v0.1/JamLengthGenK.wls](https://gitlab.mpikg.mpg.de/christ/phdthesis_code/-/blob/v0.1/JamLengthGenK.wls)
- 77.1 :  
<https://gitlab.gwdg.de/PhD/VesicleForms.jl>
- 78.2  (B.2):  
[https://gitlab.mpikg.mpg.de/paper/min\\_GUV\\_oscillations\\_Code/-/blob/v0.1/Boundary\\_Conditions+expansion.wl](https://gitlab.mpikg.mpg.de/paper/min_GUV_oscillations_Code/-/blob/v0.1/Boundary_Conditions+expansion.wl)
- 81.1 :  
<https://gitlab.gwdg.de/PhD/molemoto>



## *Selbständigkeitserklärung*

Hiermit versichere ich, dass ich die vorliegende Arbeit selbständig verfasst und keine anderen als die angegebenen Quellen und Hilfsmittel verwendet habe.

A handwritten signature in black ink that reads "Simon Christ". The word "Simon" is written in a cursive style, and "Christ" is written in a more blocky, slightly cursive style.

Potsdam, den 2020-06-16

Simon Christ